CHIRAL SEPARATION USING HYBRID OF PREFERENTIAL CRYSTALLIZATION MODERATED BY A MEMBRANE BARRIER

A Dissertation
Presented to
The Academic Faculty

By

Apichit Svang-Ariyaskul

In Partial Fulfillment
Of the Requirements of the Degree
Doctor of Philosophy in the
School of Chemical & Biomolecular Engineering

Georgia Institute of Technology
May, 2010

CHIRAL SEPARATION USING HYBRID OF PREFERNTIAL

CRYSTALLIZATION MODERATED BY A MEMBRANE BARRIER

Approval by

Dr. Ronald W. Rousseau
School of Chemical & Biomolecular Engineering
Georgia Institute of Technology

Dr. Mark Prausnitz
School of Chemical & Biomolecular Engineering
Georgia Institute of Technology

Dr. William J. Koros
School of Chemical & Biomolecular Engineering
Georgia Institute of Technology

Dr. Angus P. Wilkinson
School of Chemistry & Biochemistry
Georgia Institute of Technology

Dr. Amyn Teja
School of Chemical & Biomolecular Engineering
Georgia Institute of Technology

Date approved: February 26, 2010

To my loving parents, the love of my life.

ACKNOWLEDGEMENTS

I would like to express my sincere gratitude to my advisers, Dr. Ronald Rousseau and Dr. William Koros, for their support and encouragement throughout my PhD studies. I really appreciate that they are very patient and have a faith in me. It was quite a long journey but it did worth it. I truly appreciate their constructive criticism to bring the best out of me and to prepare me well for both professional and personal development for the future. I would not be as capable and confident without their guidance. I also would like to extend sincere appreciation to my committee, Dr. Amyn Teja, Dr. Mark Prausnitz, and Dr. Angus Wilkinson.

I would like to thank my research group members, Dr. Quinta Nwanosike-Warren, Dr. Krystle Chavez, Dr. Stephanie Barthe, PJ Dumont, and Dr. Karsten Bartling, for their thoughtful advice, meaningful discussions, help in the lab, and more importantly, encouragement during tough time.

I would like to thanks my friends from Georgia Tech and from back home, Thailand, for their encouragement and keep me sane during difficult time. I would like to thank my best friends, Dr. Quinta Nwanosike-Warren, Pei Yoong Koh, and Brandon Woodward, for making me feel home even though I am thousands of miles away. Thanks very much for always being there for me, keeping me smile and happy, and more importantly listening to me whining on a daily basis. I would like to thank my very dear friend, Dr. Nakadech Youngwilai, who always makes my day full of sunshine, raises me up when I am down, and makes me believe that there is hope out there. I would like to thank my very best friend from back home, Dr. Rapeepong Suwanwarangkul, who was

always there for me and supported me during the most difficult time in my life while I was in Canada. Even he passed away, he will always be my prayer.

I would like to give a big thank to my family especially my parents, Sanga and Ar Svang-Ariyaskul, that raised me up with endless love, unbounded support, and constant encouragement. There were several hurdles before I came to this point and I could not make it at all without their support. My parents worked extra hard during economic crisis in Thailand and sacrificed their needs to ensure they had enough money to support my special courses to prepare me for further education abroad. It paid off at the end.

One thing I keep in mind since I was a little kid is that my mom always told me to ask a teacher questions and never leave a classroom without getting answers. This is how I learn and I follow her throughout my entire education. If I did not listen to her, I definitely could not come this far and be as successful as I am today.

Another thing is that my mom always wants her children to obtain a PhD as she lacked of an opportunity to pursue her higher education even high school as my grand parents were very poor and she had to quit school to work. She loves to learn and to be a student. No other children did it for her. But here I am, Ma. I am doing it for you. Maybe the inspiration behind me doing a PhD is my mom.

I would like to thank all of my older sisters and older brothers for their love, care, and support since I was a little kid. I will always be their little brother. It is very nice to always have them caring for me.

It is all to these people who I owe upmost gratitude for their support. I would not be able to make it without them.

TABLE OF CONTENT

LIST OF TABLES

LIST OF FIGURES

NOMENCLATURE

A = area (cm^2), A_c = a single crystal surface area, A_M = membrane surface area

a = activity, a^* = activity of saturated solution

a = wetted surface per volume of the bed (cm^{-1}), a_v = specific surface (cm^{-1})

C = solute concentration in bulk fluid (g/cm^3), C_i= solute concentration at crystal interface, C^*= solute solubility concentration

C_d = drag coefficient

ΔC_p = the change of heat capacity (J/mol.K)

D = crystal seed diameter (cm) or diffusivity (cm^2/min), D_p = crystal seed diameter or particle diameter, D_v = bulk diffusivity, D_e = effective diffusivity (cm^2/min)

E_a = activation energy (J/mol)

F = volumetric flow rate (cm^3/min)

f = friction factor

g = gravitational acceleration (cm/min^2) or overall growth rate order

ΔH = The change of enthalpy (J/mol), ΔH_f = enthalpy of fusion, ΔH_d = enthalpy of dissolution

J = mass flux ($g/cm^2 \cdot min$), J_c = mass flux due to bulk diffusion, J_r = mass flux due to surface integration, J_v = mass flux across the membrane

k_c = mass transfer coefficient at crystal surface (cm/min)

k_r = rate constant for surface integration (cm/min)

K_G = overall growth rate coefficient (cm/min)

l = membrane thickness (cm)

M = mass (g), M_c = increased mass in a crystal at a certain time, M_t = total mass of

crystals

m = mass of solution (g)

MSE = mean square error

MW = molecular weight (kg/kgmol)

N = number of crystal seeds

n = number of hollow fibers or number of data point

P = pressure (g/cm·min^2)

R = gas constant (J/mol·K) = 8.314472 J/mol.K

R_h = hydraulic radius (cm)

Re = Reynolds number

r = surface integration rate order

ΔS = entropy (J/mol.K), ΔS_f = entropy of fusion, ΔS_d = entropy of dissolution

S_M = cross-sectional area of the membrane module (cm^2)

s = supersaturation

T = temperature (^{o}C or K), T_f = fusion temperature, T_t = triple point temperature

t = time (min)

V = volume of each vessel (cm^3)

V_A = molecular volume of D or L-Glu (m^3/kgmol)

v = velocity (cm/min), v_0 = superficial velocity, $\langle v \rangle$ = average velocity

w = solute concentration (g/g solution), w^* = solubility, w^{met} = metastable limit, w_{ex} = concentration from the regression of the experimental values, w_{md} = concentration from the mathematical model

w' = concentration in the mixed solution for HPLC analysis (g/g solution)

X = x-axis value in HPLC calibration curve

x = mole fraction

Y = y-axis value in HPLC calibration curve

α = separation factor

δ = the thickness of the boundary layer (cm)

σ = relative supersaturation

ρ = density of solution (g/cm^3), ρ_s= density of solution, ρ_c= density of crystals

μ = chemical potential (J/mol)

η = viscosity (cP or g/cm·min)

ε = porosity of the membrane surface or the volume porosity of the membrane module in the shell side

τ = tortuosity

ξ_B = association factor of solvent (water)

LIST OF ABBREVIATIONS

D-Glu = D-glutamic acid

L-Glu = L-glutamic acid

DL-Glu = DL-glutamic acid

L-Asp = L-aspartic acid

L-Leu = L-leucine

DL-Leu = DL-leucine

s = shell side of the membrane module

t = tube side of the membrane module

SUMMARY

Chiral separation was proposed using a novel hybrid of preferential crystallization and a membrane barrier. The main objective of this work is to establish a new alternative chiral separation process that increases the product yield and purity from the existing processes. This work is primarily based on experiments. The process simulations were carried out for experimental planning and for helping explain the system behavior. The process simulations were also carried out to study the effects of process variables at the conditions beyond the feasible of the available experimental set ups.

A crystallizer was divided into two separated vessels attached with a membrane. The selected membrane should be able to block the crystals from moving between vessels but allow high mass diffusion of the solutes. The operating conditions must be well-controlled so that the product yield increased from current processes while high purity product was maintained. The fundamentals of the new process are that the operating conditions must be controlled so that the pure enantiomers are produced on opposite sides of a membrane, which acts simply as a physical barrier to block crystals from moving between isolated chambers. The crystallization process starts with racemate mother liquor in different chambers on either side of the membrane. Seed crystals of each enantiomer are introduced into different vessels so that such crystal will grow and remain enotiomerically pure. Therefore, the increase of product yield and purity are expected. In this work, the separation of DL-glutamic acid was studied as a test model. DL-glutamic acid was a racemic conglomerate which was appropriate for the separation by

our hybrid process. L-glutamic acid is an important feed stock for the production of mono sodium glutamate which is used globally as a food flavor enhancement.

The solubility and metastable limits were measured as process boundaries. The solubility is a thermodynamic variable while the metastable limit is a kinetic variable changing upon the system dynamic, in this case, the cooling rate. The faster the cooling rate is, the further away the metastable limit is from the solubility. The concentrations of the undesired species must not reach the metastable limit; otherwise, the undesired species will crystallize as impurity.

Preliminary experiments of DL-glutamic acid resolution were carried out through the set up with a flat plate membrane. The investigation was carried out with two amounts of seed mass (3.50 and 25.22 g/dm^3 crystallizer) at a cooling rate of $1.0^oC/h$. The results showed that the more the seed mass was introduced, the more the final products were recovered because the crystallizing surface increased. The preliminary experimental results showed that this process is feasible. The product yield increased up to 65% from preferential crystallization and the product purity was up to 94%. The adjusted overall crystal growth rate was also estimated here.

The experimental and simulation results showed that the effects from mass transfer resistance due to bulk diffusion were not important while the effects from mass transfer resistance from transmembrane diffusion and surface integration were important. Therefore, the set up with hollow fiber membranes was used in the future to reduce a transmembrane resistance by increasing the membrane area. The surface integration resistance depends on the crystallizing surface area and could be reduced by the increase of seed mass.

For the advanced set up with hollow fiber membranes, the experiments were carried out at various amounts of seed crystals (3.98, 10.09, 25.22, and 74.87 g/dm^3 crystallizer) and cooling rates (0.2, 0.5, 1.0, 5.0, and 10.0^{o}C/h) to investigate on these effects on the system behaviors and the product yield and purity. The experimental results showed that the larger the amount of the seed mass was, the larger the amount of product was recovered because of larger crystallizing surface area. The change of the cooling rate affected the metastable limit gap and the run time. If the cooling rate was too slow at 0.2^{o}C/h, the metastable limit gap was too narrow and the metastable limit was reached. If the cooling rate was too fast at 5.0 and 10.0^{o}C/h, the run time was insufficient for both crystallization of desired species and export of undesired species; therefore, the metastable limit was reached. The cooling rates of 0.5 and 1.0^{o}C/h were feasible and the metastable limit was not reached. The amount of product from cooling rate of 0.5^{o}C/h was higher than the one from cooling rate of 1.0^{o}C/h because longer time was provided for crystallization of desired species. The product purity from the successful experiments was over 99.7% which was considered pure (Mullin, 2001).

The experiments and simulations were carried out further to find the desirable amount of seed mass that gave product yield close to the amount of seed mass and the amount of maximum possible yield. The experiments were run using the 10.09 g seed mass/ dm^3 crystallizer at the cooling rate of 0.5^{o}C/h. The product purity was over 99.7%. The product yield was 65% of the seed mass and 70% of maximum possible yield. This yield was satisfactory. The yield enhancement was up to 283% from preferential crystallization and this enhancement showed that this process was revolutionary.

The major innovation of this work is an establishment of a novel chiral separation process using preferential crystallization coupled with a membrane barrier. This hybrid process was proved to be promising from a significant increase in product yield and purity compared to existing chiral separation processes. This work sets up a process design platform to extend the use of this hybrid process to a separation of other mixtures. This novel process especially is a promising alternative for chiral separation of pharmaceutical compounds which include more than fifty percent of approved drugs world-wide. A better performance chiral separation technique contributes to cut the operating cost and to reduce the price of chiral drugs.

CHAPTER 1

INTRODUCTION

More than fifty percent of approved drugs worldwide are chiral (Li et al., 1999; Wang et al., 2002; Wang et al., 2005). Chirality is a geometric property of the nonidentity of an object with its mirror image. A chiral object may exist in two enantiomers which are superimposable mirror images of each other, for instance, a hand and a snail shell (Jacques et al, 1994). If the object has one or more superimposable mirror images, it is achiral, for example, left and right hands. Enantiomers possess identical physical and chemical properties in an achiral environment but exhibit those properties differently in a chiral environment, such as biological systems (Wang et al., 2003). Each enantiomer fits and acts differently on target receptor sites and metabolic pathways that are chiral in nature. The binding sites and chiral drugs can be visualized as a lock-and-key that only one enantiomer fits.

Generally, only one enantiomer is active for desired activities while the other enantiomer does not perform the activities but instead often inhibits the desired activities, generates side effects, or exhibits toxicity (Wang et al., 2002; Yokota et al., 2006). Therefore, one enantiomer is generally preferable over the other. Ordinary chiral drugs synthesis in the absence of an asymmetric catalyst produces a racemate, an equimolar mixture of both enantiomers (Yokota, 2006; Profir, 2004). Thus enantioseparation processes have been drawing significant attention to the pharmaceutical industries. There are four main chiral separation techniques: crystallization, chromatography, chiral solvent extraction, and kinetic resolution. Although catalytic asymmetric synthesis and

enzymatic kinetic resolution have been advancing consistently, chiral separation by crystallization is still the most important in large scale productions due to its simplicity (Wang et al., 2002; Wang et al., 2003).

There are two main chiral crystallization methods: diastereomeric crystallization and direct crystallization. Classical resolution through diastereomeric crystallization is broadly used in industry, especially in the pharmaceutical industry, to produce the majority of chiral drugs that are not derived from natural products (Collins et al., 1992). Diastereomeric crystallization is a process in which an enantiomer is converted to a diastereomer, a stereomer that is not a mirror image of the other, and salted out. Direct crystallization includes simultaneous crystallization and preferential crystallization. Even though direct crystallization is an alternative technique, it is a promising process and shows real economic importance in industry (Wang et al., 2004).

Another chiral resolution method involving membrane separation has recently shown promise. Membrane separation has the potential for enantioseparation due to its energy efficiency, simple set-up and possible continuous operation even though the initial investment is high (Gumi *et al.*, 2005a). Membrane separation in chiral resolution is not well established, but in principle, a chiral selector membrane binds one of the enantiomers while allowing the other enantiomer to pass though the membrane (Hadik *et al.*, 2005). The membrane matrix itself can be enantioselective; otherwise the enantioselective carrier is bounded chemically or physically into the nonselective membrane. In principle, the membrane separates one enantiomer from the chiral solution to a pure solvent. It is desired that only one enantiomer can transport across the membrane to the solvent due to the chemical potential difference. The process is

isothermal and the solution is undersaturated. No solid form of enantiomers is present. Dense membranes and ultrafiltration membranes have been studied by several researchers (Higuchi *et al.*, 2002; Overdevest *et al.*, 2002; Higuchi *et al.*, 2003; Gumi *et al.*, 2005a; Gumi *et al.*, 2005b; Hadik *et al.*, 2005). From recent studies of solid membranes, the isothermal process started with an undersaturated racemate liquor solution on one side and a pure solvent on the other side (Gumi *et al.*, 2005a, 2005b; Hadik *et al.*, 2005). Hypothetically, each enantiomer will be in a separated vessel in a solution form and the solid products need to be crystallized afterward. The selectivity was at most 2.3, with the process taking over 140 hours and never reaching equilibrium. This means that the final product was at most 85% of the desired enantiomer. Still another approach involving a liquid membrane has been pursued by four research groups (Bryjack *et al.,* 1993; Keruentjes *et al.*,1996; Dzygiel *et al.*,1999; Hadik *et al.*, 2002). The main drawback of liquid membranes is their instability, owing to loss of active solvents in the membranes. All of these requirements raise the question of whether membrane separation is a promising process for chiral resolution.

The present research explores an approach to chiral separation that integrates crystallization and membrane separation. The key feature of this hybrid process is to control system conditions so that the growth of pure enantiomers occurs on opposite sides of a permeate membrane. Instead of using enantioselective membranes, a nonselective porous membrane is used as a physical barrier. Preferential crystallization starts with a racemate liquor solution on both sides of the membrane. Then, one kind of enantiomer crystal will be seeded into opposite sides of the membrane. It is expected that each kind of enantiomer will grow on its own seed nuclei and the other will transfer across the

membrane to grow on its species in the other side of the membrane. The objective of this proposed idea is to produce crystals with not only higher purity but also higher quantity than other existing processes.

In our research, we propose a new concept for chiral separation. The methodology involves two vessels containing solutions of a racemic solution with each vessel seeded by crystals of different enantiomers. It is expected that each enantiomer will grow only on crystals of its own kind: i.e. on the added seed crystals and daughter nuclei formed by secondary nucleation. The challenging feature of this process is to transport the non-crystallizing enantiomer from each vessel to the other where it is being crystallized; doing so keeps the super saturation of the non-crystallizing enantiomers below its metastable limit. It is also essential to block transport of nuclei between the vessels so that only one enantiomer grows in each vessel.

Elsner *et al.* (2007) proposed the idea of exchanging crystal-free mother liquor between two vessels. They did a theoretical analysis and optimization using mathematical simulations involving isothermal crystallization of threonine. Their simulations predicted that the purity and yield of crystal product increased with mother-liquor exchange between the two vessels. While providing valuable insight, there was no suggestion as to how such a process could be implemented practically.

The key feature of the newly proposed process is a hybrid crystallization-membrane system that controls conditions so that the growth of pure enantiomers occurs on opposite sides of a permeate membrane. In essence, a simple nonselective porous membrane is used as a physical barrier to the crystal exchange between two crystallizers, and crystallization starts in each with a racemic solution on both sides of the membrane.

In order to provide a clear description of the process, first consider preferential crystallization from a racemic mixture in a crystallizer. Begin by lowering the temperature so that the solution is slightly supersaturated with respect to both enantiomers (L and D) and add seed crystals of one of the enantiomers, say L. The added seed crystals grow and participate in secondary nucleation of new L crystals that also grow, thereby depleting the available supersaturation of L. Without further cooling, the overall yield of L crystals at this point is low, and yet the solution remains supersaturated with D. Continuing to cool the system produces additional growth of L crystals, but this also increases the supersaturation of D and at some point the metastable limit of D will be exceeded and primary nuclei created. Once there is primary nucleation in the system, it is no longer possible to obtain the desired chiral purity being sought, and such conditions define the maximum yield that can be achieved in a simple batch system.

In the proposed process, there is a flux of D from the crystallizer in which L is being crystallized into a second crystallizer that has been seeded with D crystals. Simultaneously, there is a flux of L from the second crystallizer into the first. These fluxes result from the driving forces created when crystallization in each vessel reduces the concentration of the solute being crystallized in that vessel. The membrane separating the two crystallizers is permeable to both enantiomers but blocks the transfer of crystals between the two units. Such a system now makes it feasible to obtain both high yield and high purity of each enantiomer.

Table 1.1: Comparison of three hypothetic crystallization systems

System	Volume of each Crystallizer (mL)	Mass of Each Recovered Crystalline Species	Condition of Crystalline Product
Simple Batch	1000	m	Mixture of D and L crystals
Elsner et al. (2007)	500 × 2	m	Pure D from V1 crystallizer, Pure L from the other
Present Work	500 × 2	m	Pure D from V1 crystallizer, Pure L from the other

In illustration of the proposed process, consider three hypothetical preferential crystallization systems: a simple batch crystallizer, a system with liquid exchange as suggested by Elsner et al. (2007), and the new membrane-crystallization hybrid system described above. Suppose that each of the crystallizers in the systems utilizing two crystallizers has a volume of 500 mL, while the simple batch system has a single crystallizer with a volume of 1000 mL. It is assumed that nucleation, crystal growth and transport of isomers between the two vessels are sufficiently rapid to prevent the generation of significant supersaturation. Clearly, the three systems all produce the same amount of product crystals of each of the isomers. However, in the batch crystallizer, the

product crystals are a mixture of D and L crystals, while the hypothetical system of Elsner et al. (2007) and the present system produce equivalent, chirally pure products.

Glutamic acid ($C_5H_9NO_4$) was chosen as a model solute for this novel integrated system due to its simple molecular structure and reasonable price compared to other amino acids and drugs. L-Glu is a based-stock for the production of mono sodium glutamate. L-Glu was produced 13,000 tons annually through preferential crystallization in the period of 1963 to 1973 (Jacques et al, 1981, page 223). Even though the production of L-Glu through preferential crystallization has been discontinued, this process is still considered economically competitive with the fermentation process which is now used world-wide. Currently, the global demand of L-Glu is 1.7 million tons annually (Wikipedia). The structure of glutamic acid is presented in Figure 1.1. Moreover, glutamic acid forms a racemic conglomerate, which makes it a good choice for this study.

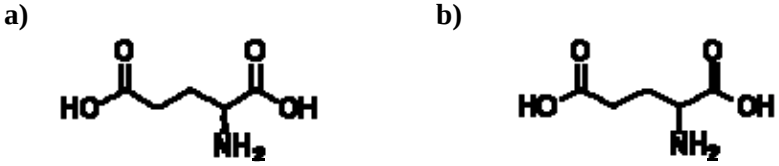

Figure 1.1: Molecular structure of a) D-Glu and b) L-Glu

Racemic species are divided into three categories: racemic compound, racemic conglomerate, and pseudoracemate (Li et al., 1999; Wang et al., 2003). The details of racemic mixture categories will be explained in the literature review section.

The objectives of this study are:

1. To establish a novel chiral separation process through a hybrid of preferential crystallization and membrane separation to increase the product purity and yield as an efficient alternative process.
2. To determine the importance of operating conditions to achieve the highest purity product at an acceptable yield. The most associated operating conditions include amount of crystal seeds, cooling rate, and membrane properties.

There are seven chapters in this thesis. Chapter 1 introduces the motivations and concepts of this thesis and key background supporting the thesis concept. Chapter 2 provides the literature review including important theories, backgrounds, and information related to this thesis. Chapter 3 describes the experimental apparatus and how this apparatus was designed. Chapter 3 provides the general procedures used throughout the thesis. Chapter 4 shows the experimental work of solubility and metastable limit measurements as these two limits govern the separation process. Chapter 5 shows the work of basic novel chiral separation through a hybrid of preferential crystallization and a flat plate membrane barrier. In this chapter, the basic experiments were conducted to study the feasibility of the process focusing on the effect of seed mass on product yield and purity with a short cooling range of temperature. The results proved that this process is promising before the experimental work was carried out further. Chapter 6 extends the work from Chapter 5 by replacing a flat plate membrane with a hollow fiber membrane module to facilitate the mass transfer across the membrane which is the process limitation for the set up with a flat plate membrane as suggested by mathematical calculations. By increasing the mass transfer across the membrane, the cooling range of temperature can

be increased dramatically and it results in the increase of product yield and purity. The experiments were done extensively with the help of mathematical modeling for experimental planning. The experimental results were compared with simulated results here. Several levels of seed mass and cooling rates are used to determine the operating conditions that produce the highest product purity and yield. Chapter 7 concludes the whole thesis, confirms that the objectives were reached, and gives the recommendations. All of the variables in this process are listed and show how some of them were studied and how some of them could not be studied. The experimental and simulated results show that this process is revolutionary and improves the product yield and purity drastically up to 420% of a preferential crystallization. The recommendations of future work are presented in this chapter as well.

CHAPTER 2

LITERATURE REVIEW

2.1 Crystallization Kinetics

Crystal yield and purity depend upon system thermodynamics, nucleation, and growth kinetics. In this section, the fundamentals of the kinetic phenomena are outlined and related to the present study.

2.1.1 Nucleation

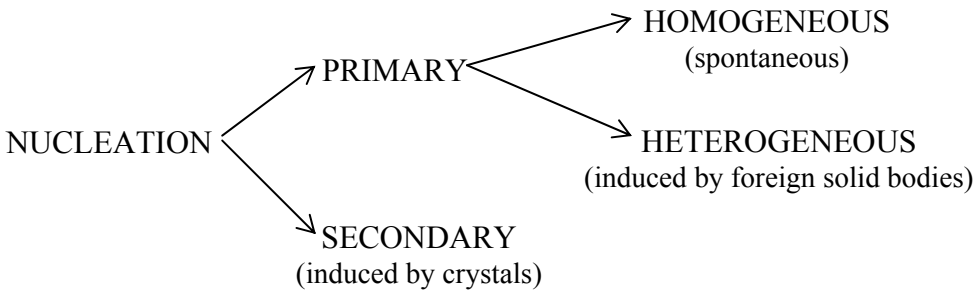

Figure 2.1: Nucleation terminology (Mullin, 2002)

The formation of new crystals is accomplished by nucleation which includes primary or secondary nucleations as illustrated in Figure 2.1. Primary nucleation is not influenced by the presence of crystals of the crystallizing species; intended new crystals are produced directly from the liquid either homogeneously or heterogeneously. Crystallization may not occur under solely supersaturation or supercooling conditions.

Secondary nucleation is influenced by non-foreign seeded crystals or primary nucleated crystals.

Primary nucleation can occur through homogeneous or heterogeneous nucleation. Homogenous nucleation is the process that crystal nuclei are formed from a homogenous fluid. To form crystal nuclei, the constituent molecules must coagulate, resist the tendency to dissolve, and orient into a fixed lattice. The number of molecules in a stable nucleus can vary from ten to several thousands (Mullins, 2002, page 182). Heterogeneous crystallization is the process that nuclei are formed with the presence of the impurity. Generally, it is well accepted that the true homogenous nucleation is uncommon. The mere trace of impurity can affect the nucleation rate significantly. The appropriate foreign surface can induce nucleation at a lower super saturation degree than that from primary nucleation. The interfacial tension is a significant factor controlling the nucleation process and is reduced as the presence of the suitable foreign body surface. Therefore, the nucleation rate is increased.

Secondary nucleation occurs under the presence of non-foreign crystals. The presence of non-foreign crystals could be intentional or unintentional. Preferential crystallization deliberately introduces seed crystals into mother liquor. However, after the crystallization process, the crystallizer wall and mixing blades might not be clean well enough and crystals were stuck on them; this causes secondary nucleation unintentionally. There are several possible mechanisms of secondary nucleation described by Strickland-Constable (1968). Initial breeding is a process that crystalline dusts on top of the seed crystal are swept off from the newly introduced seed crystal and new nuclei are produced. Needle breeding occurs when the weak out-growths are detached from the crystal and

form new nuclei. Polycrystalline breeding is the fragmentation of a weak polycrystalline mass. Collision breeding occurs from the collision of the crystal with crystals or with parts of the crystallizer.

2.1.2 Crystal growth

Crystal growth results from deposition of solute or melts in a manner that results in enlargement of the crystalline solid. There are several crystal growth theories including surface energy theory, adsorption layer theory, and diffusion-reaction theory.

Surface energy theory explains the growth of the crystal through surface free energy. In supersaturated medium, the crystal will eventually develop into an equilibrium shape so that each face will grow to allow the whole crystal to have minimum total surface free energy for a given volume. The relative growth rates of crystal faces depend on their respective surface energies. The lower the surface energy, the faster that crystal face grows. This theory explains the growth rate merely through thermodynamics. However, this theory leaves out kinetics variables such as supersaturation and solution movement which are the well-known effects on the crystal growth rate. Moreover, there is a very limited quantitative support of surface energy theory. Therefore, there is no general acceptance of this theory due to these drawbacks.

Adsorption layer theory or the Gibbs-Volmer theory also explains the crystal growth on basis of thermodynamic reasoning. When the units of crystallizing substance reach crystal surface, they cannot integrate into a crystal lattice instantaneously but merely lose one degree of freedom. These units are adsorbed at the lowest energy kink and form a loosely adsorbed layer at the interface. This interface is in equilibrium with

the bulk solution and the crystal surface. This layer or the third phase is called "adsorption layer." The adsorption continues two-dimensionally until the face is complete and the next layer is then built. One of the drawbacks of the theory is the surface diffusion in the adsorption layer is not well-known yet (Mullins, 2002, page 223). Moreover, this theory as well as surface energy theory does not include well-known effects on crystal growth such as kinetic properties into consideration.

Diffusion-reaction theory is different from surface energy theory and adsorption layer theory in that it includes thermodynamic and kinetic properties. In this theory, crystal growth can be modeled as two stages in series, one involving mass transfer from the solution to the crystal surface and the other being the migration of the solute into the crystal lattice. As shown in Figure 2.2, solute molecules are transferred from the bulk fluid to the crystal-solution interface followed by arrangement of the crystal lattice. The driving forces of these two processes are differences in chemical potential, which can be approximately related to the concentrations:

Diffusion: $J_c = k_c(C - C_i)$ Equation 2.1

Integration: $J_r = k_r(C_i - C^*)^r$ Equation 2.2

Where J_c = mass flux due to bulk mass transfer, J_r = mass flux due to integration in the crystal surface, k_c = mass transfer coefficient by bulk mass transfer, k_r = a rate constant for the surface integration, r = growth rate order due to the integration. The mass transfer coefficient, k_c, is a function of crystal size, crystal density, solution density, solution diffusivity, viscosity, and surface velocity. Each face of a crystal has a different k_r because of its different surface energy.

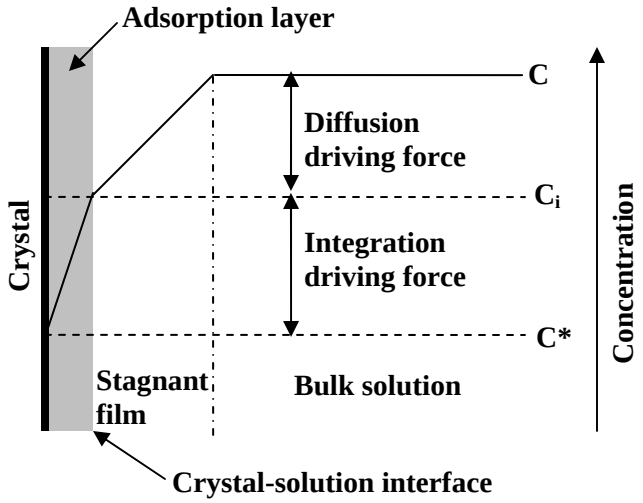

Figure 2.2: Concentration driving force in crystallization in diffusion-integration model where C = solute concentration in bulk fluid, C_i = solute concentration at crystal-solution interface, C^* = solute solubility concentration (Mullis, 2001)

Generally, the diffusion process is considered to be linearly dependent on the concentration difference; however, the integration step (Equation 2.2) is not necessarily first-order. Since it is difficult to measure C_i, Equation 2.3 with r=1 is more convenient to apply because of elimination of the C_i term.

$$J = J_c = J_r = K_G(C - C^*)^g = k_c(C - C_i) = k_r(C_i - C^*)^r \qquad \text{Equation 2.3}$$

If $r = 1$, $J = K_G(C - C^*)$

$$K_G = \frac{k_c k_r}{k_c + k_r} \qquad \text{Equation 2.4}$$

K_G = overall growth rate coefficient. g = overall growth rate order. Crystallization of several inorganic salts from aqueous solution has g in the range of 1 to 2.

The estimation of growth kinetic parameters, k_c, k_r, and r, was studied and published by several research groups, for example, Barbier et al (2009), Garside (1971),

Kumar (2009a, 2009b, 2009c), Mullin and Gaska (1969), Sahin et al (2000), Sahin et al (2003). The growth kinetic parameters, k_c, k_r, and r, were estimated for several substances such as gypsum (Barbier et al, 2009), ammonium pentaborate (Sahin, 2003), boric acid (Sahin, 2000), potassium sulfate (Mulin and Gaska, 1696, 1973), and sucrose (Bennema, 1973; Howell et al, 1969; Kumar et al, 2008; Kumar, 2009; Sgudaldino et al, 2006; Shiau, 2003).

Equation 2.3 can be linearized as:

$$\ln J = \ln K_G + g \ln \Delta C \qquad \text{Equation 2.5}$$

Where $\Delta C = C - C^*$.

The solubility (C^*) is a known value and the concentration (C) can be measured. The mass flux (J) can also be measured by the mass of crystal increase divided by the time and the crystal surface area. Therefore, g and K_G can be estimated as a slope and an intercept of the plot of ln J versus ln ($C - C^*$). K_G depends on temperature and the crystal size. Therefore, the experiments must be isothermal and the crystal size and shape must be well-defined. In our case, it is not possible to control the crystal size and shape as the needles break during the process. The last two terms in Equation 2.3 can be rearranged as:

$$C_i = \left(\frac{J}{k_r}\right)^{1/r} + C^* \qquad \text{Equation 2.6}$$

Then, substitute C_i back into Equation 2.3 and obtain:

$$J = k_c \Delta C - \left(\frac{k_c}{k_r^{1/r}}\right) J^{1/r} \qquad \text{Equation 2.7}$$

Equation 2.7 is complex as it contains three unknown parameters. Equation 2.7 can be rearranged for linear plotting as:

$$\frac{J}{\Delta C} = k_c - \left(\frac{k_c}{k_r^{1/r}}\right)\frac{J}{\Delta C}^{1/r} \qquad \text{Equation 2.8}$$

Equation 2.8 (Kumar, 2009c) can be plotted as $J/\Delta C$ versus $J^{1/r}/\Delta C$. k_c = slope and k_r = (-intercept/slope)^r. In this case, r has to be known or calculated from g in Equation 2.3. Kumar (2009c) used the equations that were rearranged by his/her work and other people works including Sobczak (1990) and Karpinski (1985) to estimate k_c, k_r, and r from the experimental data for the growth of ammonium pentaborate crystals (Sahin et al, 2003), borax dehydrate crystals (Ceyhan et al, 2007), and boric acid crystals (Sahin, 2000). Kumar showed that the equation from Karpinski (1985) fitted all experimental data the best with R^2 more than 0.98. Equation 2.7 can be rearranged according to Karpinski (1985) as:

$$\frac{\Delta C}{J^{1/r}} = \frac{J^{\frac{r-1}{r}}}{k_c} + \frac{1}{k_r^{1/r}} \qquad \text{Equation 2.9}$$

$\Delta C/ J^{1/r}$ is plotted versus $J^{(r-1)/r}$. k_c = 1/slope and k_r = (1/intercept)^r.

The assumptions for the estimation of k_c, k_r, and r, are as follows (Karpinski, 1985; Kumar, 2009a, 2009b, 2009c; Sahin et al, 2000; Sahin, 2002; Sahin et al, 2003):

1. The process is steady state.
2. The process is isothermal.
3. There is no accumulation of solute at any point in the concentrated field.
4. Crystal particles only grow at surface-like heterogeneous reaction.
5. No nucleation occurs.
6. No crystal breakage.
7. The particle shape, size, and number are well-defined.
8. The crystal size range is narrow.

k_c and k_r increase as the temperature increases from the calculations from various groups (Kumar,2009c; Karpinski, 1985; Sobczak; 1990) and this finding is confirmed by multiple works (Elsner et al, 2007; Kumar 2009a; Kumar, 2009b; Sahin et al 2003). At a higher temperature, the solute molecules can diffuse and integrate into the crystal surface at the faster rate. Kumar (2009c) has proposed the relationship of both k_r to the temperature as an Arrhenius relationship as:

$$k_r = k_0 \exp\left(-\frac{E_a}{RT}\right) \qquad \text{Equation 2.10}$$

k_0 = pre-exponential constant, E_a = activation energy (J/mol), and R = gas constant (J/mol·K). k may not change significantly if the activation energy is very low. According to Equation 2.3, k_c can also be viewed as:

$$k_c = \frac{\rho_s D_v}{\delta} \qquad \text{Equation 2.11}$$

$$\delta = \frac{3}{2}\left(\frac{\rho_s D_v}{\eta}\right)^{1/3}\left(\frac{\eta D_p}{\rho_s v}\right)^{1/2} \qquad \text{Equation 2.12}$$

Where ρ_s = solution density (g/cm^3), D_v = bulk diffusivity (cm^2/min), D_p = particle diameter (cm), δ = the thickness of the boundary layer (cm), η = solution viscosity (g/cm·min), v = fluid velocity at the particle surface (cm/min). δ can be calculated from Equation 2.12 (Gilmer et al, 1971). As can be seen from Equation 2.11, D_v increases with temperature while δ decreases with temperature. Therefore, k_c increases as the temperature increases.

The dependent of k_c and k_r on the particle diameter is unclear and no solid explanation could be found. In Figure 21.6 of McCabe et al (1993), the plot of k_c versus the particle size was shown for falling particles in water at 25^{o}C. It shows that k_c

decreased with particle size exponentially from 2-10 μm, remained constant until the size was 10,000 μm and decreased with no pattern after 10,000 μm. Equation 2.11 and 2.12 show that as D_p increases, k_c decreased with $(D_p)^{1/2}$. However, Kumar (2009c) and Sahin (2000) showed that k_c increased as the particle size increased as they explained that the larger the particles, the larger mass flux. Kumar (2009c) also showed that there was no obvious relationship between k_r and the particle size for ammonium petaborate, borax dehydrate, and boric acid.

The mass transfer coefficient k_c needs to be estimated to be used in the model. For k_c values, Harriott (1962) studied and collected data of mass transfer coefficient of suspended particles in water in a stirred tank with $D_v = 10^{-5}$ cm^2/s and $\mu = 1$ cP with a particle diameter range from 2-10,000 μm. k_c* is the minimum mass transfer coefficient. The actual value is higher than k_c*, 1.5 to 5 time greater than k_c* for a wide range of particle sizes and agitation conditions. The reason behind this is that the average slip velocity increases due to frequent acceleration and deceleration of particles and small eddies in turbulent liquid penetration close to the particle surface which increases local mass transfer rate (McCabe et al., 1993). Viscosity alone has a much smaller effect on k_c than diffusivity (Harriott, 1962). k_c* is nearly constant for particle diameters in the range of 100 to 10,000 μm. After accounting for differences in diffusivity and differences in particle and solution density, k_c as k_c* of 0.2975 cm/min is estimated from Harriott (1962) and used for mathematical modeling.

2.1.3 Solubility and metastable limits

Solubility in a solvent is defined as the solute concentration in a solution that is at its equilibrium with the solid at given conditions. It generally increases with temperature. The solubility can be approximated with Equation 2.13 and can be modified to the van't Hoff equation after a series of assumptions in Equation 2.14.

$$\ln\frac{1}{x\gamma} == -\frac{\Delta H_f}{RT}\left(\frac{T_t}{T}-1\right)-\frac{\Delta C_p}{R}\left(\frac{T_t}{T}-1\right)+\frac{\Delta C_p}{R}\ln\frac{T_t}{T} \qquad \text{Equation 2.13}$$

$$\ln x = \frac{\Delta H_f}{R}\left[\frac{1}{T_f}-\frac{1}{T}\right] = -\frac{\Delta H_f}{RT}+\frac{\Delta S_f}{R} \qquad \text{Equation 2.14}$$

x= the solute mole fraction in the solution, γ = activity coefficient, and $\Delta H_f = T_f \Delta S_f$. a = activity, ΔC_p = heat capacity, ΔH_f = molal enthalpy of fusion, ΔS_f = the molal entropy of fusion, T = the solution temperature, T_t = the triple point temperature, T_f = the fusion temperature, and R = gas constant. The assumptions in van't Hoff equation are as follows. First, the difference between triple point and melting point temperatures is very small. As a result, the difference between enthalpy of fusion between them is also very small. Therefore, the triple point temperature is substituted by the melting point temperature and enthalpy of fusion at melting temperature is used. Second, the difference in heat capacity of the solute in the solid and liquid states is negligible. Furthermore, if $\frac{T_t}{T} \to 1, \ln\frac{T_t}{T} \to \frac{T_t}{T}-1$. Then, the last two terms in Equation 2.13 are cancelled out. Third, the solution is ideal and therefore γ = 1. Equation 2.14 can be plotted as a straight line as $\ln x$ versus T^{-1}. Even though the plot of $\ln x$ versus T^{-1}may be a straight line, the slope might be different from $-\Delta H_f / R$ because of non-ideal behavior

(Beiny and Mullin, 1987). Therefore the enthalpy and the entropy of dissolution must be used to account for non-ideality as shown here.

$$\ln x = -\frac{\Delta H_d}{RT} + \frac{\Delta S_d}{R} \qquad \text{Equation 2.15}$$

In a cooling preferential crystallization process, the solution is cooled with a constant concentration and crystals nucleate at a temperature that often may not necessarily correspond to its solubility. This is because the solute molecules do not have enough time to attract other solute molecules to crystallize and reach equilibrium—especially under an imposed cooling ramp. Thus, crystallization occurs at a lower temperature this sets metastable limit (supersaturation limit or supersolubility limit or metastable saturation) temperature which is lower than the solubility temperature. Because solute molecules need a certain period of time to transport to reach one another to nucleate, the faster cooling rate will shift the metastable limit further below the thermodynamic solubility limit. The metastable limit is a kinetic property that depends on several factors such as the cooling rate, the mixing, the presence of impurity, and the thermal history of the solution. Therefore, the metastable limit varies from one particular system to the other and could not be estimated.

Please note that the kinetic metastable limit stated here is not necessarily the same as the locus of points where the second derivative of the Gibbs energy with respect to composition is zero (or the thermodynamic metastable limit).

2.1.4 Crystallization process

Figure 2.3 illustrates undersaturated, metastable, and labile regions. In the undersaturation region, the solution is homogeneous and no crystals are present. In the metastable region, the solution is supersaturated. No primary nucleation occurs in this region, but existing crystals grow and secondary nucleation can occur in this region.

In the labile region, crystals nucleate spontaneously (primary nucleation) from solution due to the high degree of supersaturation. When the solution temperature is reduced to the metastable limit, the solution concentration drops until it reaches the solubility at the selected constant temperature. Clearly, due to mass transfer and "surface integration" phenomena at the face of the growing nuclei, the concentration does not necessarily decrease to its solubility immediately.

Crystallization kinetics depend upon a driving force that may be in various ways: e.g. supersaturation ratio, *S*, and absolute or relative supersaturation, σ. These quantities are defined below.

$$\Delta C = C - C^* \qquad \text{Equation 2.16}$$

$$s = \frac{C}{C^*} \qquad \text{Equation 2.17}$$

$$\sigma = \frac{\Delta C}{C^*} = s - 1 \qquad \text{Equation 2.18}$$

Where C = the solution concentration and C^*= the solubility concentration.

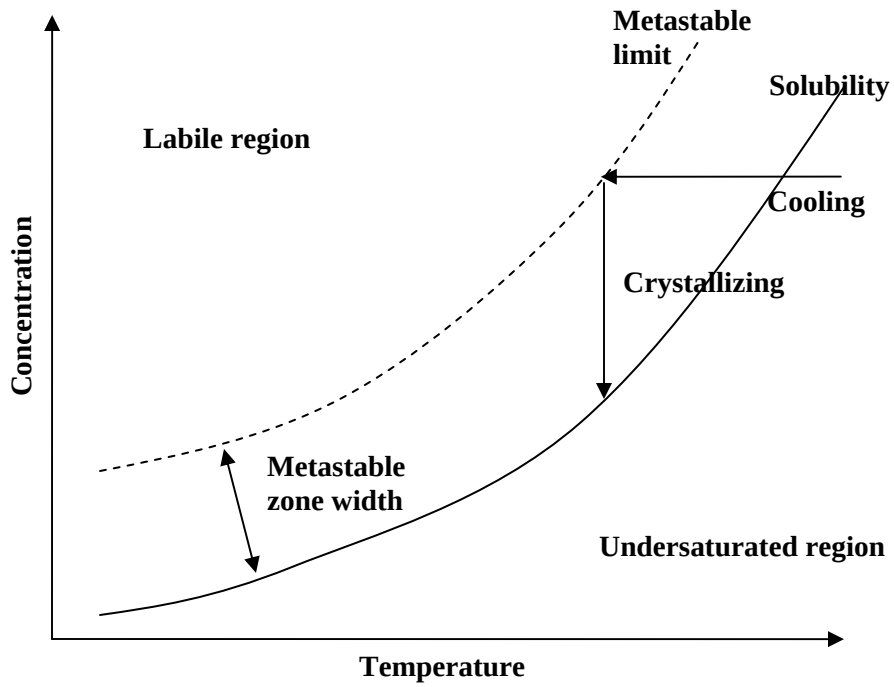

Figure 2.3: Solubility and metastable limit diagram

The fundamental driving force for crystallization comes from the difference between chemical potential, μ, of the solute in different states, i.e. in solution (state 1) and in the crystal (state 2) as shown in Equation 2.18. The relationship between the supersaturation, s, and the solution temperature can be derived as below.

$$\Delta\mu = \mu_1 - \mu_2 \qquad \text{Equation 2.19}$$

$$\mu = \mu_0 + RT \ln a \qquad \text{Equation 2.20}$$

$$\ln s = \ln\left(\frac{a}{a*}\right) = \frac{\Delta\mu}{RT} \qquad \text{Equation 2.21}$$

$$s = \exp\left(\frac{\Delta\mu}{RT}\right)$$ Equation 2.22

Where a^* = the activity of a saturated solution. In this case, $\Delta\mu$ is not necessary a constant.

2.2 Racemic mixtures

Categories of racemic mixtures are distinguished by the nature of the properties of crystals with which they are in equilibrium. There are racemic compounds, racemic conglomerates, and pseudoracemates (solid solutions). Racemic compounds form crystals in which the two enantiomers of opposite chirality are paired in a well-defined arrangement in the crystal lattice. In such compounds, the enantiomer has greater affinity to the mirror image type than to its own species. On the other hand, if each enantiomer has greater attraction to its own kind than the opposite, two enantiomers crystallize as an equimolar mixture of two homochiral crystals, in other words, a physical mixture of pure crystals of each enantiomer. This mixture, which is called a racemic conglomerate corresponds to that, addressed in this work: glutamic acid. If differences in affinity between enantiomers of like or opposite kinds are small, two enantiomers exist more or less randomly in the same crystal lattice as a solid solution. This is called pseudoracemate.

Figure 2.4 illustrates the binary phase diagrams of three types of racemate crystals. Figure 2.4 a) shows the binary phase diagram of racemic conglomerate. As the temperature decreases below T_A^f-E line or so called "liquid curve", the melts crystallize

as one enantiomerically pure solid. As the temperature decreases to T_R^f, the system contains two enantiomerically pure solids (D and L) and liquid E (equimolar of D and L). At the temperature below T_R^f, the system contains two enantiomerically pure solids.

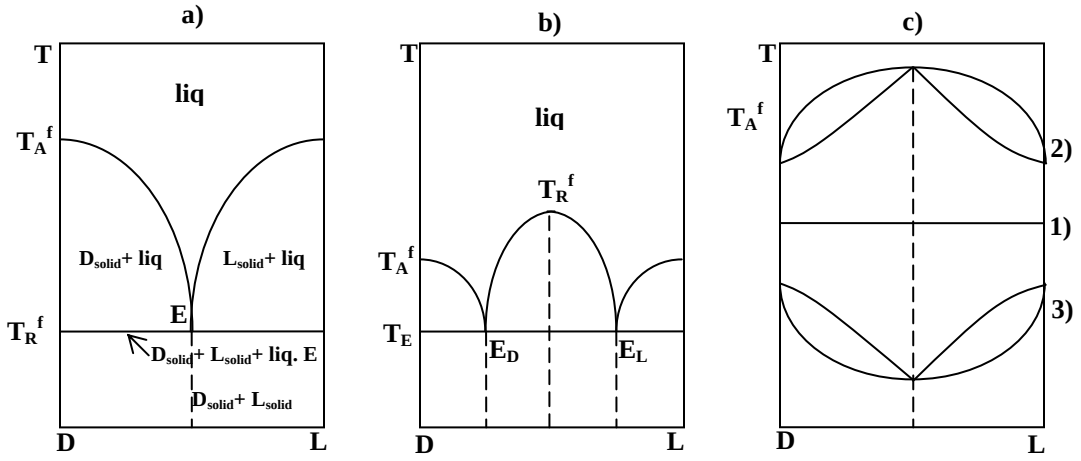

Figure 2.4: Binary phase diagram of concentration versus temperature of a) racemic conglomerate and some racemic compound, b) racemic compound, c) pseudoracemate with three cases: 1) ideal, 2) with a maximum, and 3) with a minimum. D = D-enantiomer, L = L-enantiomer, A = pure enantiomer, R = racemate, E = eutectic point, T^f = fusion temperature.

Figure 2.4 b) shows binary phase diagram of racemic compounds. At temperature lower than T_E, the solids contain racemic compounds and excess enantiomer solids. As the temperature increases above T_E, the solid starts to melt. At the composition between E_D and E_L and the temperature lower than T_R^f, there are two phases which are the racemic compound solid and the liquid. At the region D-E_D and L-E_L, pure enantiomer solid and the liquid exist. Figure 2.4 b) shapes could vary depending on the

system. T_R^f could be higher or lower than T_A^f and the distance between E_D and E_L could be very close to zero or could expands to almost D and L.

Figure 2.4 c) shows the binary phase diagram of pseudoracemate. There are three types of pseudoracemate. In case 1), the mixtures in all proportions melt at the same temperature as the pure enantiomers. The phase diagram shows the maximum melting point for racemate for case 2) and the minimum for case 3). The number of pseudoracemates that have been studied is very limited compared to racemic conglomerate and racemic compounds (Jacques *et al*, 1994, page 105).

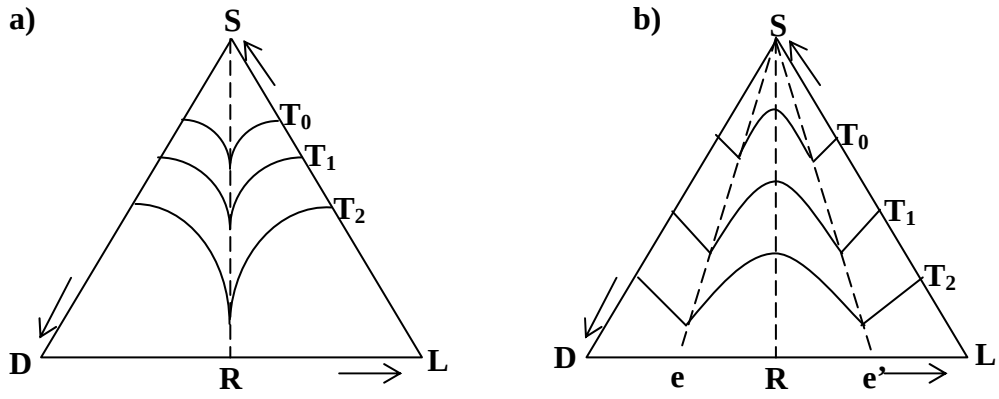

Figure 2.5: Tertiary phase diagram showing the solubilities of a) racemic conglomerate and b) racemic compound at different temperatures. D = D-enantiomer, L = L-enantiomer, S = solvent, R = equimolar concentration of D and L-enantiomer, T_0, T_1, T_2 = temperature, $T_0 < T_1 < T_2$ for endothermic and $T_0 > T_1 > T_2$ for exothermic.

As the racemic conglomerate and the racemic compound are the majority of the racemic mixtures, the focus of enantioseparation is on these two mixtures. Ternary phase diagrams of racemic compounds and racemic conglomerates are presented in Figure 2.5 a)

and Figure 2.5 b). Figure 2.5 shows the solubility of the mixtures at different temperatures. If the process is endothermic, the higher the temperature is, the higher the solubility. If the process is exothermic, the relationship between solubility and temperature is opposite. Then, in Figure 2.5, the range of the temperature is $T_0>T_1>T_2$. In general, the enantioseparation process starts at the equimolar amount of each enantiomer. As can be seen from Figure 2.5 a), there is only one phase above the solubility line and there are three phases under the solubility line which are liquid and two enantiomer solids for the system with racemic conglomerate. The system with the racemic compound is more complicated. Figure 2.6 explains the phases in each region. In A-E-E'-A'-S region, only liquid exists. In A-E-D and A'-E'-L regions, there are two phases which are liquid and the excess enantiomer solid. In E-R-E' region, there are two phases which are liquid and racemic compound solid. Finally, in D-E-R and L-E'-R regions, there are three phases which are liquid, racemic compound solid, and excess enantiomer solid.

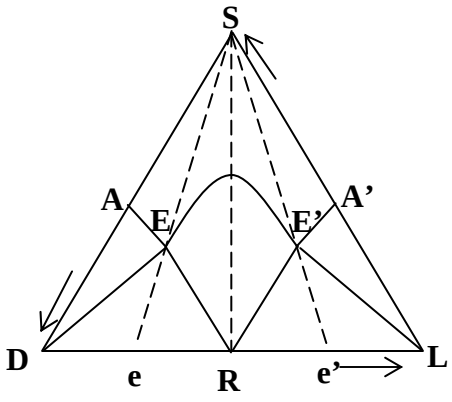

Figure 2.6: Tertiary phase diagram of racemic compound at a constant temperature. D = D-enantiomer, L = L-enantiomer, S = solvent, R = equimolar concentration of D and L-enantiomer, E and E' = eutectic point.

Over 90% of chiral drugs characterized form racemic compounds, and only roughly one percent of them are pseudoracemate (Li et al., 1999; Li et al., 2001). Enantioseparation of a racemic compound requires diastereomeric operations such as diastereomeric compound formation and asymmetric reduction. On the other hand, separation of a racemic conglomerate can be done through a simpler technique, preferential crystallization. In this technique, the desired enantiomer seed crystals are introduced into a saturated solution and the desired enantiomer grows on its own species seeds. Seeding crystallization is not applicable for racemic compound separation due to its solution equilibrium behavior (Jacques *et at*, 1994).

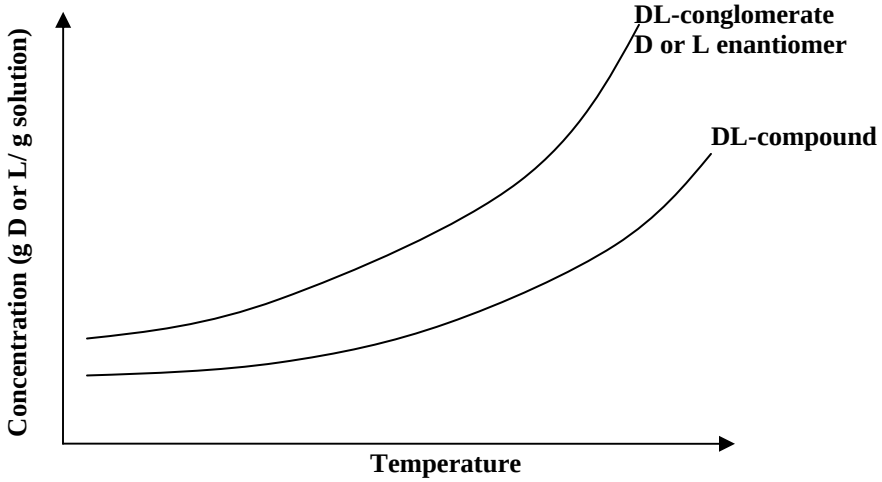

Figure 2.7: Solubility of DL-conglomerate, D or L enantiomer and DL-compound based on one enantiomer concentration versus temperature

Figure 2.7 shows the solubility of D or L enantiomer, DL-conglomerate, and DL-compound based on one enantiomer concentration in a solution. For conglomerates, two enantiomers have slight or no interaction between each other in the solution. Therefore, the solubility of an enantiomer in a conglomerate system is equal to the solubility of pure enantiomer and the solubility of a conglomerate is double the solubility of one enantiomer. However, interactions between enantiomers in the solution result in lower solubility of an enantiomer in a compound than the solubility of pure enantiomer. For pseudoracemates, the solubility of an enantiomer in a pseudoracemate is lower or equal to solubility of pure enantiomer in the solution.

Glutamic acid is categorized as a racemic conglomerate (Jacques *et al*, 1994). Solubility data obtained from a few research groups have confirmed that glutamic acid forms racemic conglomerates (Dalton and Schmidt (1933); Apelblat and Manzurolo (1997); Manzurola and Apelbalt (2002); Yalkowsky (2003)). Figure 2.8 shows the solubility data of D-Glu and L-Glu and DL-Glu in water divided by 2, i.e. $w_{DL}^* = (w_D^* + w_L^*)/2$, at different temperatures from the above mentioned research groups. Solubility of DL-Glu in water based on one species is presented to compare the magnitude of its solubility with pure species (D-Glu and L-Glu). Figure 2.8 shows that solubilities of DL-Glu based on one species are not different from pure enantiomers. From Dalton and Schmidt (1933), the solubility of D-Glu is lower than DL-Glu while L-Glutamic solubility is higher than DL-Glu from Apelblat and Manzurola (1997, 2002). The magnitude difference among different sources is approximately less than 0.005 g/g solution at the same temperature over the entire range.

The example of the solubilities of DL-compound and L-enantiomer are presented in Figure 2.9 and Figure 2.10 for a certain amino acids. These concentrations are based on one enantiomer. Figure 2.9 and Figure 2.10 show that the solubility of the compound could even more than twice lower than the solubility of the enantiomer such as serine and phenylalanine showing strong attraction of opposite enantiomers.

The chiral resolution through preferential crystallization (with seed crystals) is possible if the racemate is a conglomerate (Jacques *et al*, 1981, page 217). The mixture must be a conglomerate because each enantiomer must be able to crystallize separately. This implies that the solubility of the racemate must equal the solubility of conglomerate. Preferential crystallization is described in the next section.

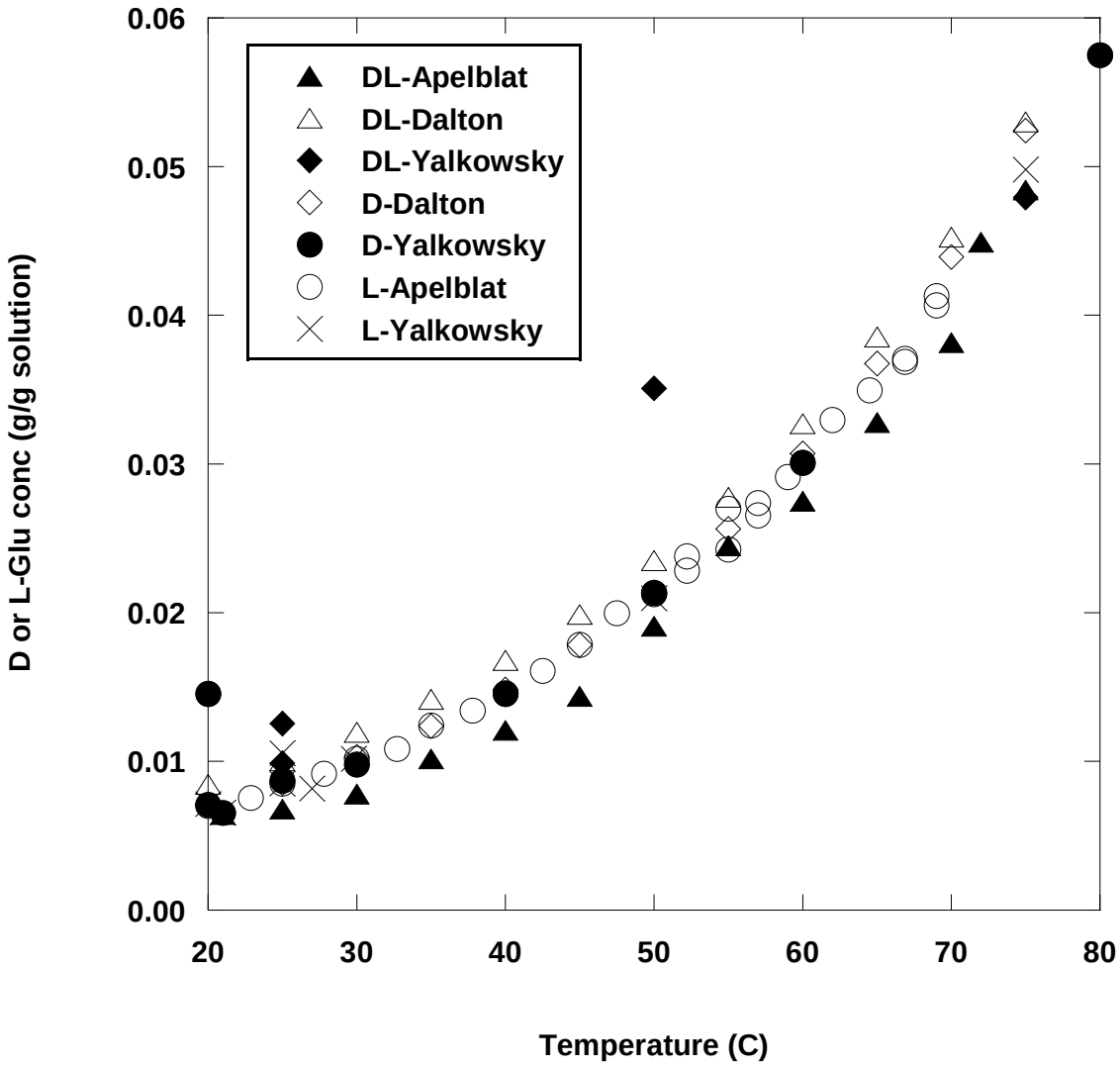

Figure 2.8: Solubility of D-Glu, L-Glu, and DL-Glu based on one enantiomer composition in water. D = D-glutamic acid, L-Glu = L-glutamic acid, DL= DL-glutamic acid, Apelblat = Apelblat and Manzurolo (1997) and Manzurola and Apelbalt (2002), Dalton = Dalton and Schmidt (1933), Yalkowsky = Yalkowsky (2003)

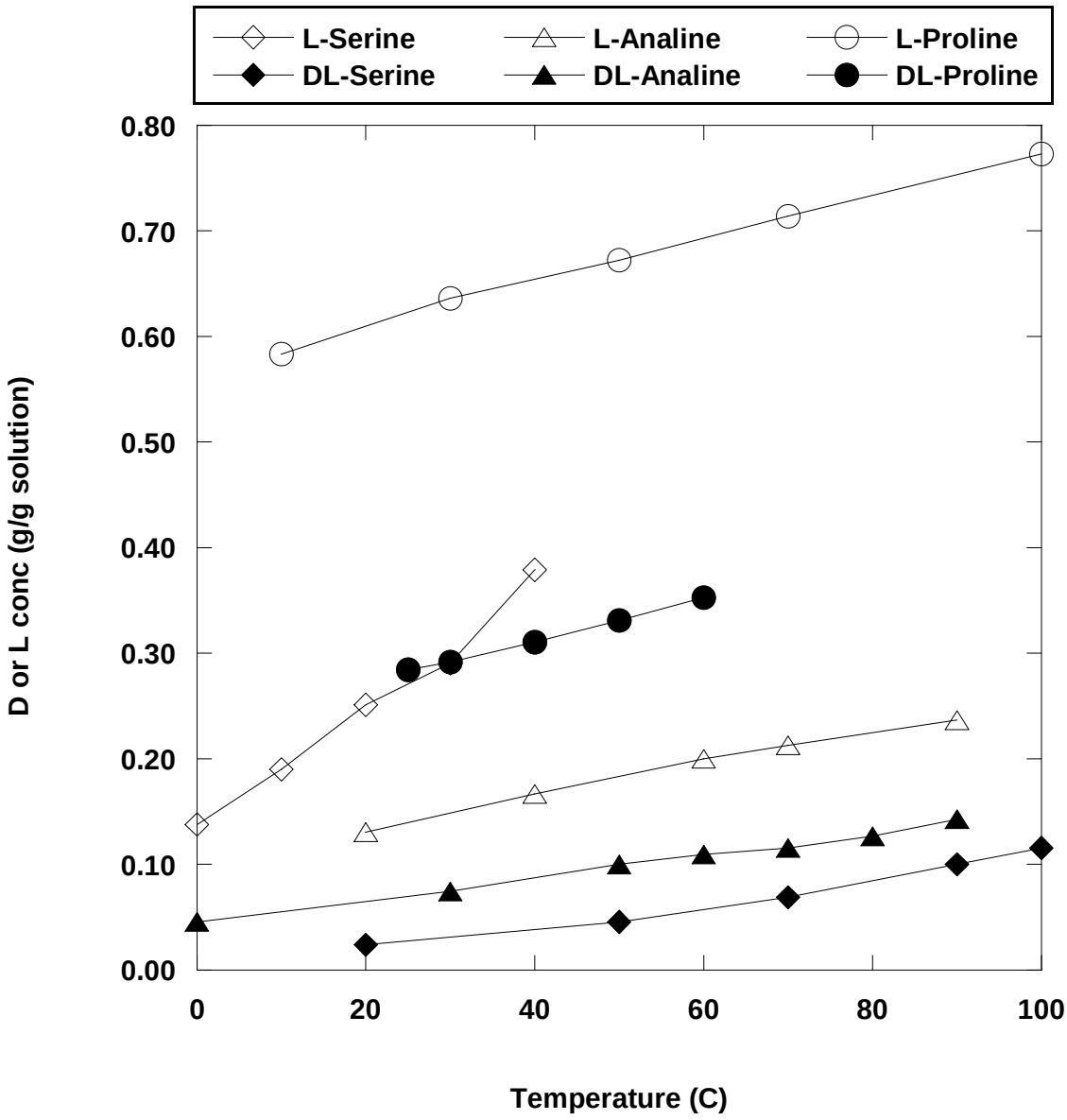

Figure 2.9: Solubility in water of L-serine, DL-serine, L-analine, DL-analine from Pazuki & Nikookar (2006), L-proline from Jit and Feng (2008) and DL-proline from Jin and Chao (1992). These concentrations are based on one enantiomer.

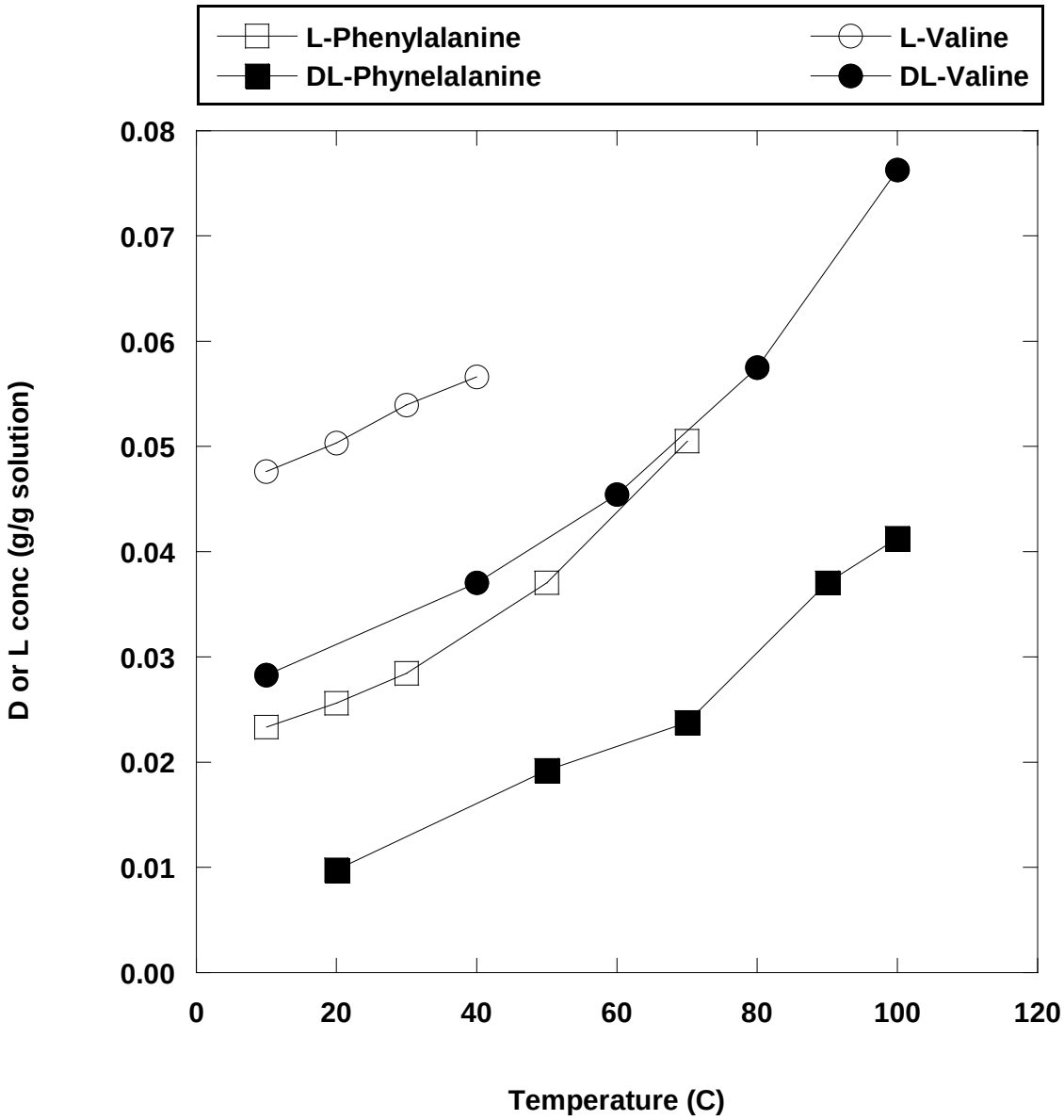

Figure 2.10: Solubility in water of L-phenylalanine (Kustov and Korelev, 2008), DL-phenylalanine (Fasman, 1976), L-valine (Pazuki & Nikookar, 2006), and DL-valine (Jin and Chao, 1992). These concentrations are based on one enantiomer.

2.3 Chiral separation through preferential crystallization

2.3.1 Preferential crystallization of racemic conglomerates

In this section, the chiral separation process through preferential crystallization is explained to give an understanding of how industry employs this process. Figure 2.11 shows tertiary phase diagram of D and L enantiomers and S (solvent) at a constant temperature. The initial supersaturation solution concentration starts at O containing equimolar amounts of D and L. The saturation concentration or solubility curve of this temperature T_0 is AEA'. The process starts with L seed crystals introduced to the system and L solute crystallizes on the L-seed crystal surface. Then the concentration of L drops but concentration of D remains the same; concentration changes from O to N. Then, L product crystals are filtered and the mother liquor concentration is N. The same amount of racemate is then added back to the mother liquor; therefore, the D-concentration (at P) is slightly higher supersaturated than the L concentration. The solution is heated up to dissolve the crystals and cooled down to T_0. D seed crystals are added to the system and the concentration of D drops but L remains constant or from P to Q. Then, D product crystals are filtered. Then, the process repeats with the path of M→N→P→Q→N as a cycle. In this process, the crystallization must stop at a certain time to ensure that primary nucleation does not happen.

As shown in Figure 2.11, it is possible that the process can be done in a cooling manner as well. The path is still M→N→P→Q→N. However, the spot M, N, P, and Q move up toward S on RS axis as the temperature decreases because the solubility concentrations of solute decrease. This could be an alternative operation in case the

solute degrades over time and the mother liquor could not be kept in the tank so long. Then, most of the solute in the mother liquor could be crystallized.

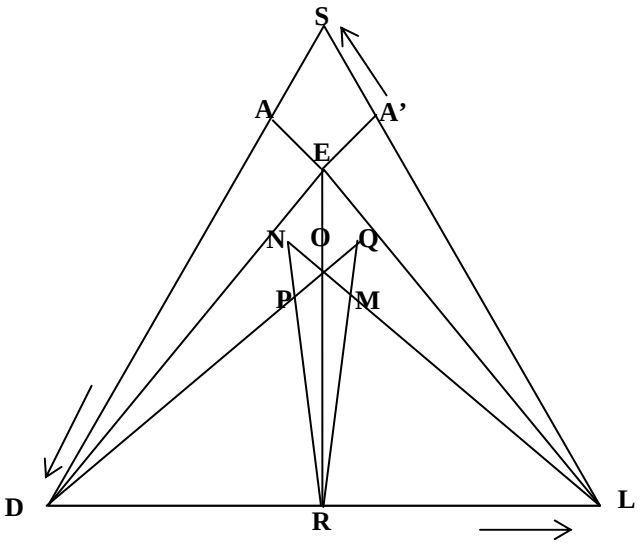

Figure 2.11: Tertiary phase diagram of D and L enantiomers and solvent (S) for preferential crystallization process.

2.3.2 Preferential crystallization of racemic compounds

A number of publications state that it is possible to separate racemic compounds through preferential crystallization but no publication states what criteria the racemic compound system must have to achieve preferential crystallization separation. After reading several articles, there are three criteria that the racemic compound systems must have to be able to be separated by preferential crystallization.

Criterion 1, the solute in the solution must have a higher affinity to its own kind seed crystals than the opposite kind. This criterion makes the system possible to have the solute grow on top of the seed. It seems questionable whether it could happen because

from the racemic compound formation point of view, the enantiomer has a stronger affinity to the opposite enantiomer to nucleate together in the same lattice. To grow solute molecules on its own kind of seed, the attraction of the solute molecules to the crystals of the same enantiomer must be higher than the attraction of the solute molecules to the opposite solute molecules in the solution.

Criterion 2, the metastable pure enantiomer crystals have to be stable enough. As can be seen from Figure 2.12, the solubility of a racemic compound is lower than pure enantiomer. In other words, racemic compound is more stable than pure enantiomer. Therefore, during the course of the process, the metastable pure enantiomer crystals have to be stable enough not to redissolve and transform to racemic compound. There are two factors regarding how fast the pure enantiomer in a metastable form would transform to the racemic compound in a stable form. The first factor is the driving force which is thermodynamic properties. The driving force is the difference in Gibbs free energy of formation (ΔG^{o}) of these two forms. ΔG^{o} of the stable form is more negative than ΔG^{o} of the metastable form. The larger the difference in ΔG^{o}, the larger the driving force. The second factor is the rate of transformation from the metastable to the stable form which is kinetic properties. The transformation depends on both thermodynamics and kinetics. For example, if the driving force is very high but the rate of transformation is very slow, the transformation might not occur during the course of operation. The process time plays an important role here. If the pure enantiomer crystals are in the process long enough, the pure enantiomer crystals will eventually transform to a racemic compound which is more stable.

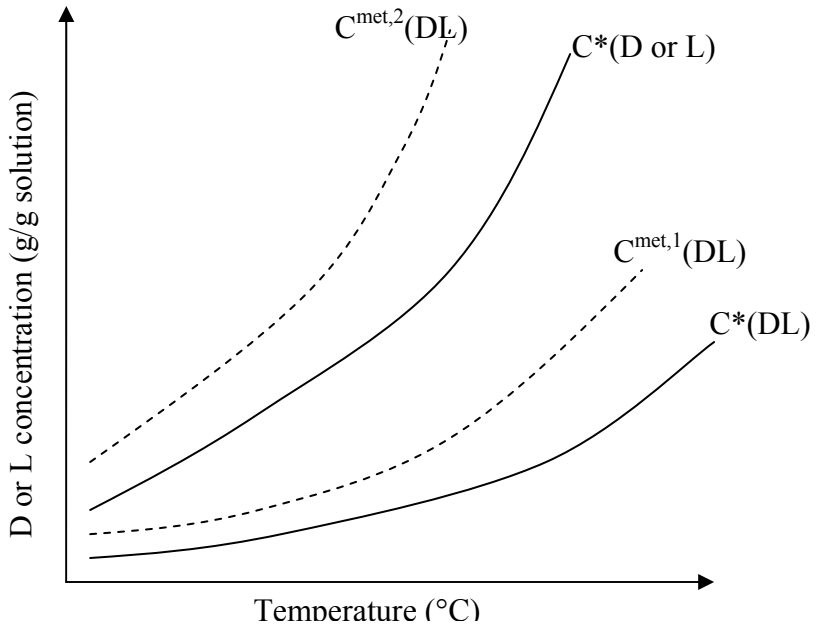

Figure 2.12: Solubility of racemic compounds and pseudoracemates, C*(DL); solubility of pure enantiomer, C*(D or L); metastable limit of racemic compounds and pseudoracemates, $C^{met,1}$(DL) and $C^{met,2}$(DL)

Criterion 3, the solubility concentrations of the racemic compound and the pure enantiomer must be close to each other and the metastable concentrations of the enantiomer must exceed the solubility concentrations of enantiomer. Figure 2.12 shows the solubility and the metastable limits of the mixture and the pure enantiomer versus temperature. In this case, the solubility of the mixture is less than the pure enantiomers; if the solubility of the mixture and the pure enantiomers are equal, it possesses the same properties as racemic conglomerates and the process is automatically feasible. In Figure 2.12, if the metastable limit of the mixture is $C^{met,1}$(DL), the process is not feasible because the mixture crystallizes before the pure enantiomer. If the metastable limit of the mixture is $C^{met,2}$(DL) the process is possible because seed crystals of the pure enantiomer can be introduced to the system in the location between the $C^{met,\ 2}$(DL) and C*(D or L); then the pure enantiomer solutes can grow on its own seed. However, whether the hybrid the process can be applied to such systems depends on how large the gap between $C^{met,2}$(DL) and C*(D or L) is; if the gap is too small, it creates great difficulty in separation. Combining this hybrid process with other methods would be another approach to increase the product yield and purity of the resolution of racemic compounds and pseudoracemates. I have done some research to find amino acids having the gap between C*(D or L) and C*(DL) not too large to make the process possible. However, I could not find one with a smaller gap between $C^{met,2}$(DL) and C*(D or L). Figure 2.9 and Figure 2.10 show the solubilities of L-enantiomer and DL-compound of a certain amino acids. These concentrations are based on one enantiomer. The solubility of the compound could lower even more than twice than the solubility of the enantiomer such as

serine and phenylalanine showing strong attraction of opposite enantiomers. Some references stated that to separate racemic mixtures by preferential crystallization, the system must be a racemic conglomerate. It could be from the fact that the existing racemic compounds that can be separated through preferential crystallization are not found.

2.4 Chiral separation through hybrid of preferential crystallization moderated by a membrane barrier

Figure 2.13 shows a schematic diagram of the novel process explored in the present work. As shown in Figure 2.13, a large vessel is separated by a membrane into two smaller vessels.

The process starts with identical supersaturated DL-Glu aqueous solution in both vessels. D-Glu seed crystals are added into supersaturated or saturated solutions in Vessel 1 and L-Glu in Vessel 2. Because of crystal growth, the concentrations drop for the D-Glu in Vessel 1 and L-Glu in Vessel 2, creating a concentration difference between the vessels. As a result, L-Glu molecules in Vessel 1 move across the membrane to Vessel 2, which has a lower L-Glu concentration, and similarly, D-Glu molecules in Vessel 2 transfer to Vessel 1. If either enantiomer concentration approaches its metastable limit, that enantiomer will crystallize. Both enantiomer concentrations need to stay between the metastable limit and solubility to yield pure component product. Clearly without a membrane, undesirable species concentration does not decrease because no crystallization of the undesirable species in that Vessel, i.e. L-Glu in Vessel 1. As temperature decreases in the preferential crystallization process, L-Glu concentration

in Vessel 1 will approach its metastable limit and cause L-Glu crystallization, which is undesirable. The same phenomenon will happen with D-Glu in Vessel 2. Rather than allow equilibration of the system at the initial temperature, the vessels are cooled to increase production of crystals in the two vessels. In summary, by using this hybrid process, the product purity is maintained and yields are increased.

Corresponding to the process described above, Figure 2.14 shows the expected concentrations of D- and L-Glu in Vessel 1. As can be seen from Figure 2.14, the concentrations of D-Glu are lower than L-Glu because D-Glu is crystallized in Vessel 1. D-Glu concentrations decrease with the temperature due to crystallization but the decrease in L-Glutamic concentrations is due to the transport to the other side of the membrane. The ideal case for our studies is that concentrations of D- and L-Glu are very close to each other. In that case, it shows that the rates of crystallization and transport across the membrane are infinitely fast. Then, the product yield and purity reach the maximum and the equilibrium. The concentrations of D and L-Glu in Vessel 2 are reverse from the ones from Vessel 1.

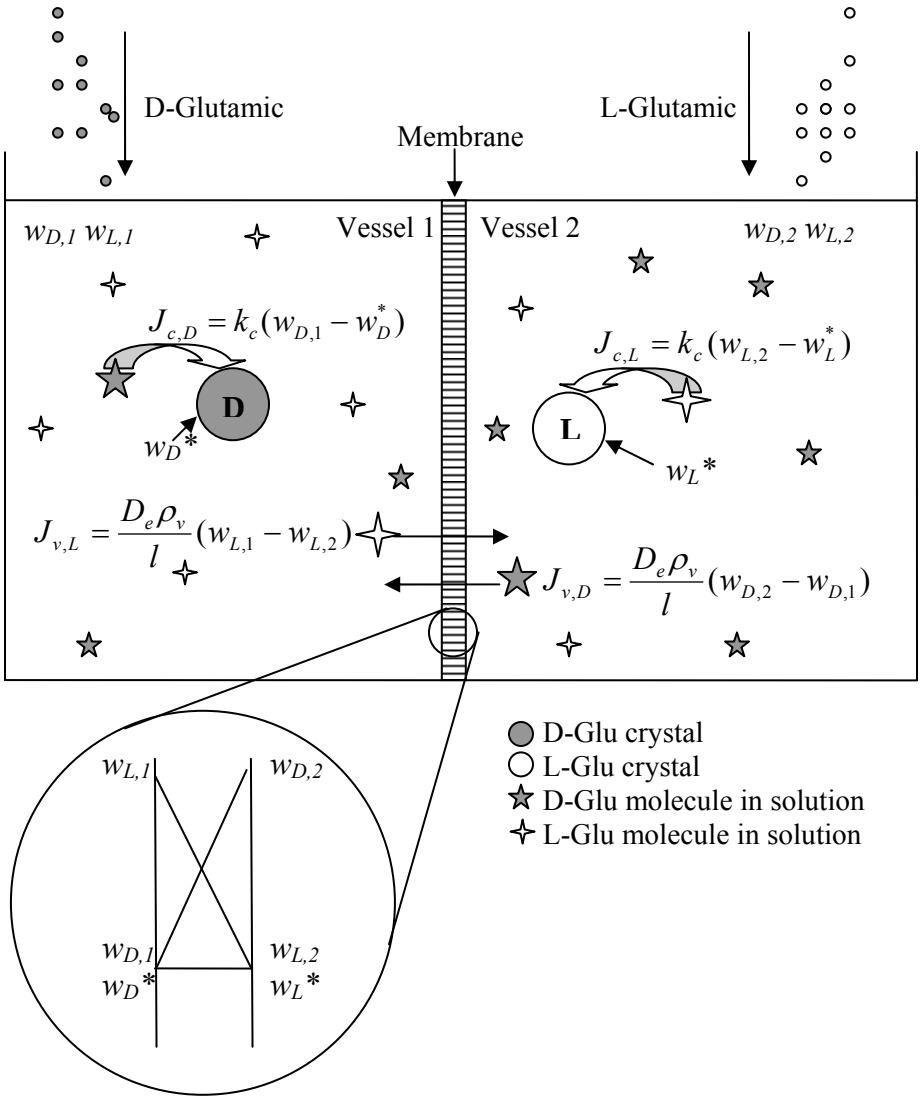

Figure 2.13: Schematic diagram of novel chiral separation process via preferential crystallization and membrane separation

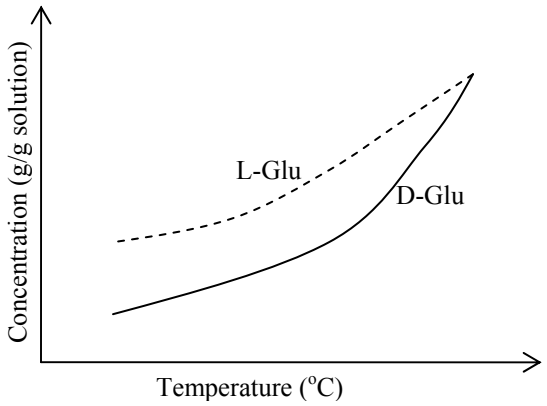

Figure 2.14: The expected concentrations of D- and L-Glu in Vessel 1 versus temperature.

2.5 Mathematical Modeling

A mathematical model was proposed to plan experiments and to explain system behavior. In our system, primary nucleation of undesirable species must be avoided. Primary nucleation occurs when the concentration reaches the metastable limit. Therefore, the primary purpose of this model is to determine when the concentration of undesired species reaches the metastable limit. Therefore, the interest of the model is to understand the process before the metastable is reached. The secondary purpose of this model is to explain transport phenomena of the process. Assumptions of the model are the followings.

1. Pressure in each vessel is equal.
2. The solution in each vessel is well-mixed.
3. Viscosity of the solution is very close to the viscosity of water.

4. The solution is ideal. In other words, the presence of one enantiomer in the solution does not affect the enantiomer solubility. Thus, the solubility of an enantiomer can be calculated by the racemate solubility (DL-Glutamate) divided by two. Also, the metastable limit concentration of an enantiomer is equal to a half of the racemate one.
5. Seed crystals have only one size.
6. There is no agglomeration of crystals.
7. Seed crystals are spheres, as a sphere has the ratio of the lowest surface area per volume at a given diameter. The lowest ratio is undesirable, but it is used to determine limitations.
8. Diffusivity in the solution (D_v) changes upon temperature only in this case and can be calculated from the Wilke-Chang equation.
9. Mass transfer coefficient of particles in a stirred tank (k_c) is constant for the particle diameter range from 100-2000 μm.
10. Mass transfer coefficient for surface integration (k_r) is constant.
11. The surface integration process is first order.
12. Concentration of D-Glu at the surface of the D-Glu seed is equal to its saturation concentration.
13. Solution density and solid glutamic acid density are constant.

The area of interest for the simulation is before the metastable limit is reached. Process simulation ends if the metastable limit is reached or primary nucleation occurs.

Subscript D, L, and DL mean D-Glu, L-Glu, and DL-Glu, respectively. Subscripts 1 and 2 mean in vessel 1 and 2, respectively.

Diffusivity

Bulk diffusivity in liquid is calculated by the Wilke-Chang equation (Wilke and Chang; 1955)

$$D_v = \frac{7.02x10^{-8}(\xi_w MW_w)^{1/2} T}{V_G^{0.6}\mu} \quad \text{Equation 2.23}$$

D_v = bulk diffusivity in liquid (cm^2/min), ξ_w = association factor of water, MW_w = molecular weight of water (kg/kgmol), T = temperature (K), V_G = molecular volume of DL-Glu (m^3/kgmol), μ = viscosity (cP)

Effective diffusivity though the membrane

$$D_e = \frac{\varepsilon}{\tau} D_v \quad \text{Equation 2.24}$$

D_e = effective diffusivity (cm^2/min), ε = porosity, τ = tortuosity

Solubility (w^*) and metastable limit (w^{met})

$$w_D^* = w_L^* = \frac{w_{DL}^*}{2} \quad \text{Equation 2.25}$$

$$w_D^{met} = w_L^{met} = \frac{w_{DL}^{met}}{2} \quad \text{Equation 2.26}$$

w = weight fraction (g/g solution), i.e., w_D^* = D-Glu weight fraction. Solubility (w^*) function used with the model is from this work. Metastable limit (w^{met}) function is calculated from experiment from this work.

Values associated with crystal geometry

$$D_p = \left(\frac{6M_t}{N\rho_c \pi} \right)^{1/3} \quad \text{Equation 2.27}$$

$$A_c = \left(\frac{6\pi^{1/2} M_t}{N\rho_c} \right)^{2/3} \quad \text{Equation 2.28}$$

M_t = total mass of crystals in vessel 1 (g), N = number of seed crystals, ρ_c= density of crystal (g/cm^3), D_p = seed crystal diameter (cm), A_c = surface area per one crystal (cm).

Mass transfer

Mass transfer to the crystal surface

$$J_c = K_G \rho_s (w - w^*) \quad \text{Equation 2.29}$$

$$J_{c,D,1} = K_G \rho_s (w_{D,1} - w_D^*) \quad \text{Equation 2.30}$$

$$J_{c,L,2} = K_G \rho_s (w_{L,2} - w_L^*) \quad \text{Equation 2.31}$$

$$\frac{dM_{c,D,1}}{dt} = J_{c,D,1} A_{c,D} \quad \text{Equation 2.32}$$

$$\frac{dM_{c,L,2}}{dt} = J_{c,L,2} A_{c,L} \quad \text{Equation 2.33}$$

$$M_{t,D,1} = N_D M_{c,D,1} = \rho_s K_G N_D \int (w_{D,1} - w_D^*) A_{c,D} dt$$ Equation 2.34

$$M_{t,L,2} = N_L M_{c,L,2} = \rho_s K_G N_L \int (w_{L,2} - w_L^*) A_{c,L} dt$$ Equation 2.35

J_c = mass flux to crystal surface (g/cm^2.min), k_G = overall mass transfer coefficient at crystal surface (cm/min), ρ_s= density of solution (g/cm^3), M_c = increased mass in a crystal at a certain time (g). K_G = overall growth rate coefficient.

Mass transfer across membrane

$$J_v = -D_e \rho_s \frac{dw}{dl}$$ Equation 2.36

$$J_{v,D,1} = \frac{D_e}{l} \rho_s (w_{D,2} - w_{D,1})$$ Equation 2.37

$$J_{v,L,2} = \frac{D_e}{l} \rho_s (w_{L,1} - w_{L,2})$$ Equation 2.38

J_v = mass flux across the membrane (g/cm^2.min), l = membrane thickness (cm)

Composition evolution

$$\frac{dw_{D,V1}}{dt} = \frac{J_{v,D} A_M}{V_1 \rho_s} - \frac{N_D J_{c,D,1} A_{c,D}}{V_1 \rho_s} = \frac{1}{V_1} \left(\frac{D_e A_M}{l} (w_{D,2} - w_{D,1}) - N_D A_{c,D} K_G (w_{D,1} - w_D^*) \right)$$

Equation 2.39

$$\frac{dw_{L,V1}}{dt} = -J_{v,L,2} \frac{A_M}{V_1 \rho_s} = -\frac{D_e A_M}{V_1 l} (w_{L,1} - w_{L,2})$$ Equation 2.40

$$\frac{dw_{D,V2}}{dt} = -J_{v,D,1} \frac{A_M}{V_2 \rho_s} = -\frac{D_e A_M}{V_1 l} (w_{D,2} - w_{D,1})$$ Equation 2.41

$$\frac{dw_{L,V2}}{dt} = \frac{J_{v,L}A_M}{V_2\rho_s} - \frac{N_L J_{c,L,2}A_{c,L}}{V_2\rho_s} = \frac{1}{V_2}\left(\frac{D_e A_M}{l}(w_{L,1} - w_{L,2}) - N_L A_{c,L} K_G (w_{L,2} - w_L^*)\right)$$

Equation 2.42

Constants

A_M = 17.3495 cm^2, l = 6 x 10^{-3} cm, V_A = 1.525 x 10^{-4} m^3/kgmol, ε = 0.4, ρ_v= 1.012 g/cm^3, ρ_c= 1.460 g/cm^3, ξ_B = 2.6, τ = 1, $K_G = k_c k_r/(k_c+k_r)$, k_c = 0.2975 cm/min (McCabe et al., 1993), k_r = unknown.

Overall mass transfer coefficient, K_G, will be estimated in section 5.4. In our work, the crystal shape is needle. The crystal aspect ratio and size could not be well-defined from the sieving process as discussed earlier. The needles also tend to break in the stir tank from the shear force resulting in a change of crystal number, size, and aspect ratio. As a result, the surface area of the crystals could not be well estimated.

The term NA_cK_G is the only unknown in the process and appears in Equations 2.34, 2.35, 2.39, and 2.42. The term NA_cK_G can be rewrite as:

$$NA_cK_G = A_{c,total}K_G$$ Equation 2.43

$A_{c,total}$ is the total surface area of the crystals. The actual and estimated value of K_G can be related as shown in Equation 2.44.

$$A_{c,total}^{actual} K_G^{actual} = A_{c,total}^{model} K_G^{model}$$ Equation 2.44

In the model, $A_{c,total}^{model}$ was given to be smaller than $A_{c,total}^{actual}$. In this model, the crystal was assumed to be one size of 600 μm as it was the upper bound of the largest sized seed crystals. The amount of crystal larger than 600 μm was negligible. The size distributions of seed crystals are shown in Figures 3.10 and 3.11. The crystal is assumed

to be spherical; therefore, its surface area with same volume is smaller than any other shapes as shown in Equation 2.45 – 2.47. The surface area per volume of sphere is:

$$\frac{A}{V} = \frac{4\pi r_{sphere}^2}{\frac{4}{3}\pi r_{sphere}^3} = \frac{3}{r_{sphere}} \qquad \text{Equation 2.45}$$

The surface area per volume of the cube with the same volume as the sphere is shown below with the condition of $\frac{4}{3}\pi r_{sphere}^3 = L_{cube}^3$.

$$\frac{A}{V} = \frac{6L_{cube}^2}{L_{cube}^3} = \frac{6}{L_{cube}} = \frac{6}{(\frac{4}{3}\pi)^{1/3} r_{sphere}} = \frac{4.30}{r_{sphere}} \qquad \text{Equation 2.46}$$

The surface area per volume of the cylinder with the same volume as the sphere is shown below. The conditions are $\frac{L_{cylinder}}{r_{cylinder}} = \beta > 10$ and $\frac{4}{3}\pi r_{sphere}^3 = \pi\left(\frac{L_{cylinder}}{\beta}\right)^2 L_{cylinder}$.

$$\frac{A}{V} = \frac{2\pi r_{cylinder} L_{cylinder}}{\pi r_{cylinder}^2 L_{cylinder}} = \frac{2}{r_{cylinder}} = \frac{2}{\left(\frac{4}{3\beta}\right)^{1/3} r_{sphere}} \qquad \text{Equation 2.47}$$

$\frac{A}{V} > \frac{3.91}{r_{sphere}}$ if $\beta > 10$.

The surface area of sphere with the same volume is proved to be larger than other shapes. Also, the actual crystal sizes were smaller than 600 μm which was the size in the model. The smaller the crystals, the larger the total surface area per volume. In conclusion, $A_{c,total}^{model}$ was proved to be smaller than $A_{c,total}^{actual}$. As a result, $K_{G,total}^{model}$ had to be smaller than $K_{G,total}^{actual}$ as shown in Equation 2.44. In other words, $K_{G,total}^{model}$ is the maximum value of $K_{G,total}^{actual}$ and can be used as an upper limit.

CHAPTER 3

EXPERIMENTAL APPARATUS AND PROCEDURES

This chapter gives an insight as to how the experimental apparatus was designed and what general procedures were used throughout the experimental work.

3.1 Experimental apparatus

There are two set ups of experimental apparatus in this research. The first set up was to use to study the enantioseparation through the integration of preferential crystallization and a flat plate membrane barrier to study the feasibility of the process. The second set up, more advanced, was designed to enhance the productivity of the process by facilitating mass transport across the membrane. This second set up was done by replacing the flat plate membrane with a hollow fiber membrane which has much higher surface area for mass transport across the membrane. The background and the reasons behind the design are also presented in this section.

3.1.1 Set up with the flat plate membrane

Because of set up simplicity, a flat plate membrane was used for a preliminary study of this novel chiral separation process to determine the feasibility of the process. The Experimental apparatus is shown in Figure 3.1.

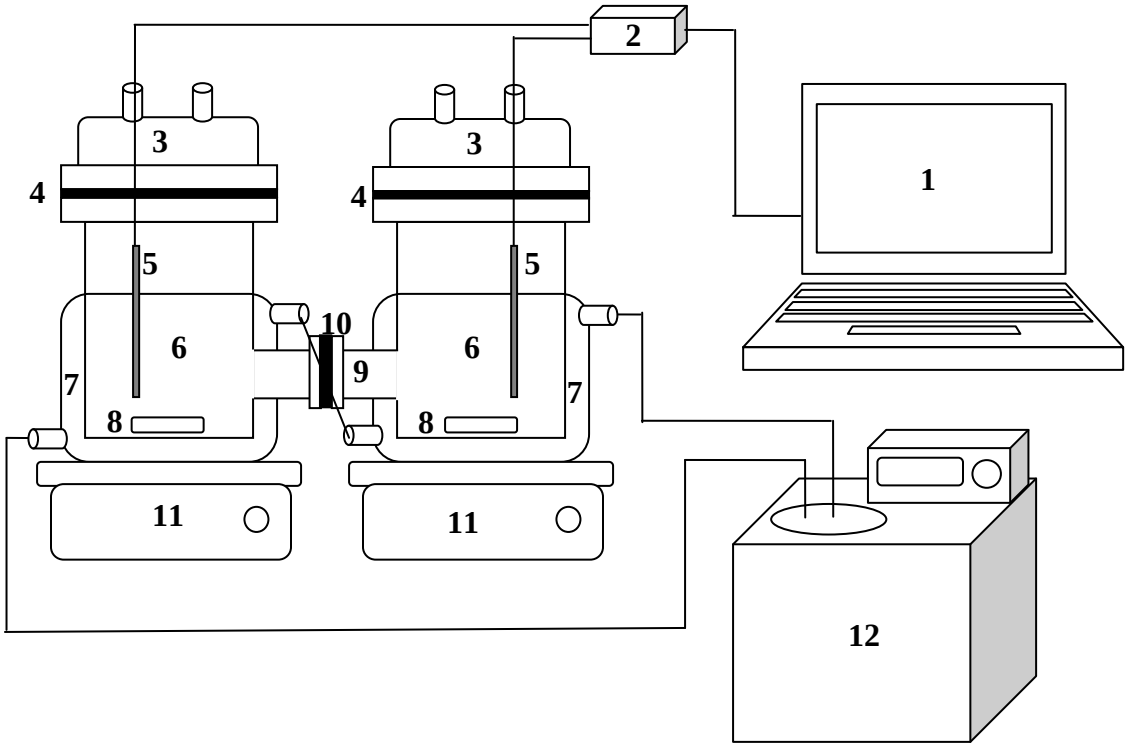

Figure 3.1: Experimental apparatus for a flat plate set up; 1) computer, 2) transducer, 3) vessel lid, 4) flanges with the rubber ring for sealing, 5) thermocouple, 6) glass vessel, 7) cooling/heating jacket, 8) stir bar, 9) connection, 10) membrane, 11) stir plate, 12) programmable heating/cooling bath

Two glass vessels with a cooling jacket are attached to each other though a connection. The end of the connection is a flat flange where a ceramic membrane is placed. Silicon rubber is used for sealing the connection together with a membrane placed in the middle and this seal is removable. Necks on top of the vessel can be opened for sample collection. The solution in the vessel is stirred by using a stir bar. The temperature and cooling pattern of water in the jacket is controlled by a programmable heating/cooling bath. Thermocouples are placed in the vessels to transmit the signal to a transducer to interpret the signal before sending it to a computer. Temperatures of the solution and cooling water are recorded by the LabView program.

Please note that the glass vessels of the preliminary experiment are slightly different from Figure 3.1. The difference is that, for the glass vessels of the preliminary experiment, the vessel was half full. The extra volume above liquid surface does not have a cooling jacket around it. Solution filled in vessel 1 is around 712 ml and 572 ml in vessel 2. The cautions of how to seal the membranes are described in 3.2.4.1

The membranes for this set up are ANOPORE^{TM} inorganic aluminum oxide membranes purchased from SPI supplies, USA to use as a physical barrier. The membrane has straight pores with a size of 0.1 μm and 40% surface porosity. The membrane diameter is 4.7 cm. Top and cross-sectional views of the membrane are shown in Figure 3.2.

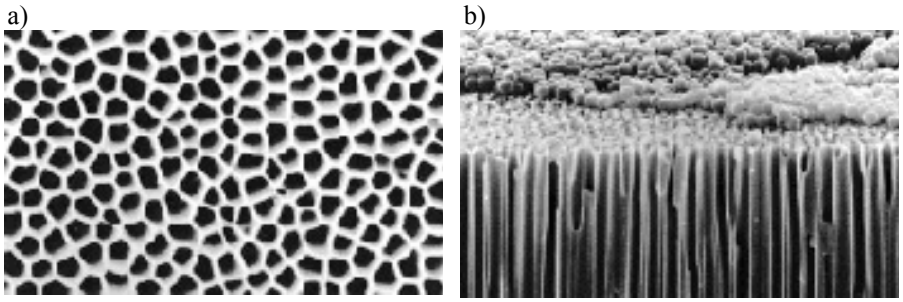

Figure 3.2: Picture of ANOPORE^{TM} inorganic aluminum oxide membrane, a) top view and b) cross-sectional view.

3.1.2 Set up with the hollow fiber membranes

3.1.2.1 General information

The experimental apparatus is shown in Figure 3.3. The membrane module in this work is the only difference from the flat plate membrane set up. In this work, the hollow fiber membrane was replaced with a flat plate membrane in previous work to increase the surface area of the membrane. Two glass vessels with a cooling jacket serve as a crystallizer. The volume of each vessel is 565 cm^3. Solution is transported to the membrane module through a peristaltic pump. The inline 10 μm HPLC filters are placed at the end of the inlet of the tube going to the membrane module to block the crystals. The inlet tubes are attached to the vibrator to shake off the crystal cake on the filter surface. Therefore, the cake thickness is minimized.

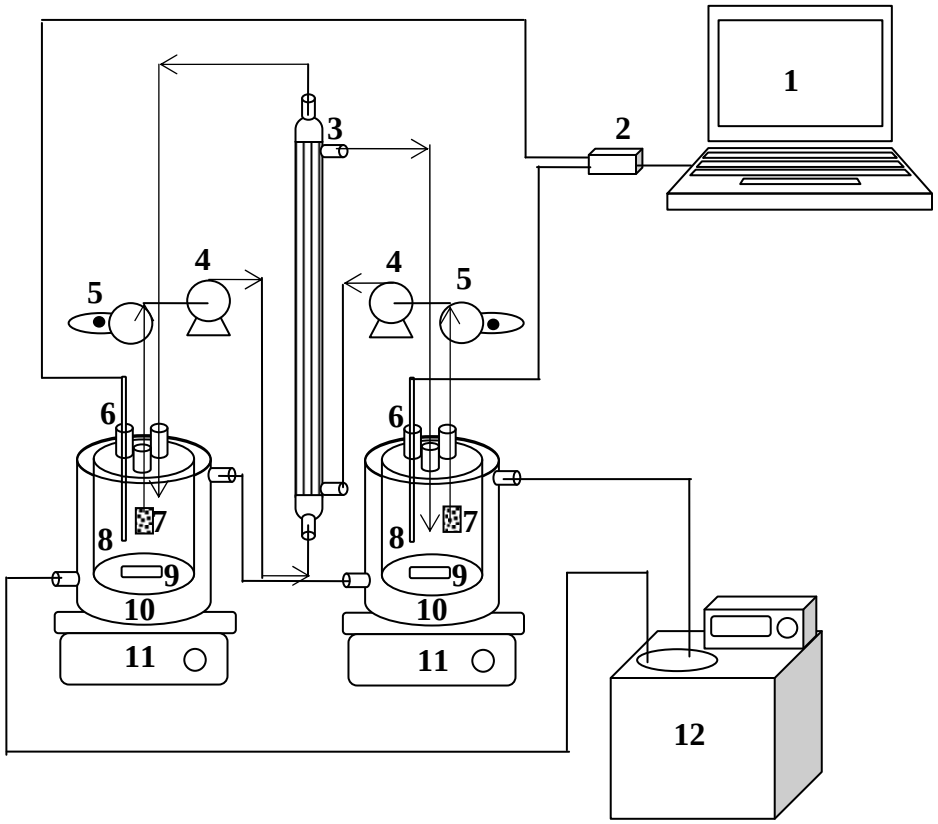

Figure 3.3: Experimental apparatus for a hollow fiber membrane set up; 1: computer, 2: transducer, 3: hollow fiber membrane module, 4: peristaltic pump, 5: vibrator; 6: thermocouple, 7: 10 μm filter, 8: glass vessel, 9; stir bar, 10: cooling jacket, 11: stir plate, 12: programmable heating/cooling bath

Ultrafiltration hollow fiber membrane module, UFP-1-C6, was purchased from GE Healthcare, USA. The inner diameter of the lumen of the fiber is 0.05 cm. The number of the fibers in the module is 520. The membrane has 1000 MWCO (molecular weight cut off) and surface area of 51867.69 cm^2 (by calculation). The outside diameter of the module is 3.2 cm and the length of the shell and the fibers are 63.5 cm. The void volume is 210 cm^3 for the shell side and 75 cm^3 for the tube side. These specifications are received from the manufacturer.

The solution from Vessel 1 was pumped to the membrane module through the shell side with an average flow rate of 98 cm^3/min while the solution from Vessel 2 was pumped to through the tube side with an average flow rate of 17 cm^3/min. The flow rates of these two streams are held at these values so that the pressure drops from top to bottom of the membrane module on both shell and tube sides are equal. Therefore, the convection transport across the membrane can be effectively avoided. The experiments were conducted to determine the flow rates to both the shell and tube sides in the membrane module so that no flow across the membrane occurred. The experimental procedure and results are presented in section 3.1.2.3.

3.1.2.2 Membrane surface area calculation

The main feature of this set up with the hollow fiber membrane unit is that the set up has much higher surface area from the flat plate membrane set up. Based on experimental results in chapter 5, it is questionable whether the membrane surface area is sufficient to transport glutamic acid across the membrane. In this section, the desired membrane surface area was determined per a crystallizer volume of each side of the

membrane. For simplicity, only mass transport behavior in vessel 1 was simulated because the D-Glu composition in one vessel is identical to the L-Glu composition in the other vessel. No experimental values except w^* and w^{met} were used here. If the crystallization is effectively instantaneous, a rate of crystallization of D-Glu in vessel 1 can be explained by Equation 3.1. As the rate of crystallization is instantaneous, the controlling step is the mass transfer across the membrane and the corresponding membrane surface area is calculated here.

$$\frac{dM_{c,D,1}}{dt} = \rho_s V \frac{dw_D^*}{dT}\left(-\frac{dT}{dt}\right) \qquad \text{Equation 3.1}$$

$$w_D^* = \alpha \exp(-\frac{\beta}{T}) \qquad \text{Equation 3.2}$$

Equation 3.2 shows that solubility is an exponential function of temperature that is rearranged from Equation 2.12. To determine the minimum membrane surface area so that the metastable limit is not exceeded, the maximum composition of L-Glu in vessel 1 and D-Glu in vessel 2 is assumed to be at their metastable limit. It means that $w_{D,2}=w_D^{met}$ and $w_{L,1}=w_L^{met}$. Mass transfer across the membrane can be described by Equation 3.3.

$$J_M A_M = \frac{D_e \rho_s A_M}{l}(w_{D,2} - w_D^*) = \frac{D_e \rho_s A_M}{l}(w_D^{met} - w_D^*) \qquad \text{Equation 3.3}$$

The rate of mass transfer across the membrane is equal to the rate of crystallization. Therefore, Equation 3.1 is equal to Equation 3.3.

$$\frac{D_e \rho_s A_M}{l}(w_D^{met} - w_D^*) = -\rho_s V \frac{dw_D^*}{dT}\frac{dT}{dt} \qquad \text{Equation 3.4}$$

$$\frac{A_M}{V} = -\frac{l}{D_e(w_D^{met} - w_D^*)}\frac{dw_D^*}{dT}\frac{dT}{dt}$$ Equation 3.5

Equation 3.5 was used to generate the ratio of desired membrane surface area per crystallizer volume illustrated in Figure 3.4 a). Figure 3.4 b) shows the solution temperature versus operating time with cooling rates of 1.0, 5.0, and 10.0°C/h. As shown in Figure 3.4 a), this ratio increased as temperature decreased and as cooling rate increased. This trend was expected because of the following reasons. As temperature decreases, diffusivity increases while the slope of solubility versus temperature *(dw_D^*/dT)* decreases. The slope (dw_D^*/dT) is steeper at higher temperature. Therefore, it results in the increase of the ratio at lower temperature. For cooling rate effects on this ratio, *dT/dt* and *(w_D^{met}-w_D^*)* increase as cooling rate increases. However, the change in magnitude of *dT/dt* is higher than *(w_D^{met}-w_D^*)*; therefore, the ratio increases with the cooling rate.

Based on the above analysis, a low cooling rate is preferred if the apparatus could be constructed as the calculation suggests. For example, a solution at 10.0°C with 1.0°C/h cooling rate needs 6 cm^2 of the membrane area to separate 1 cm^3 of the solution in a crystallizer or 2 cm^3 of the entire system. In a flat plate membrane set up, the ratio of membrane area and a crystallizer volume is 0.03 which is nowhere near the requirement. The question remains whether the apparatus construction is feasible and other membrane modules can be utilized to meet the requirement.

It would not be a problem if a hollow fiber or plate-and-frame membrane module could be used, since in principle, area per volume ratios of up to 100 can be achieved in such systems. A hollow fiber membrane module is similar to a shell and tube heat exchanger. The problem with this module is that if crystals are nucleated inside the hollow fiber, they could not be removed. This problem could be solved by placing a

filter at the tube inlet to the membrane unit as described in the previous section. Also, equal pressure between the tube and shell sides must be maintained otherwise convective mass transfer occurs which is not desirable. The flow rates of the tube and shell sides of the membrane must be controlled so that pressure difference between tube and shell sides is negligible. The flow rate calculation is explained in the next section.

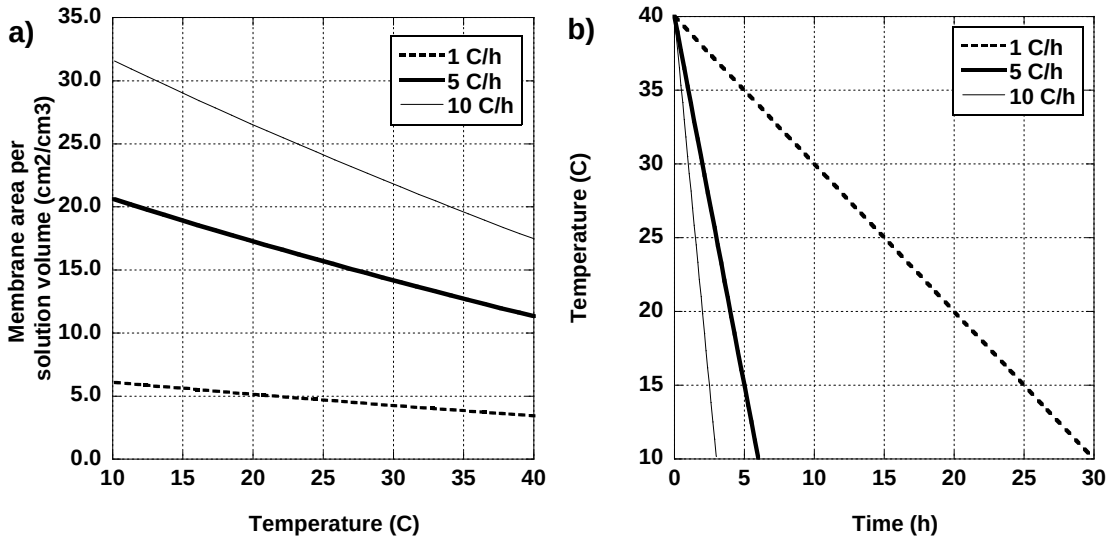

Figure 3.4: a) desired membrane area per crystallizer volume and b) solution temperature versus operating time at cooling rate of 1.0°C /h (dashed line), 5.0°C/h (heavy line), and 10.0°C /h (solid line)

3.1.2.3 Flow rate calculation

Fundamental to this thesis, mass transfer across the membrane must be primarily from diffusion. Therefore, it is crucial that convective mass transfer across the membrane must be avoided. This means that the pressure difference between tube and shell sides must be negligible.

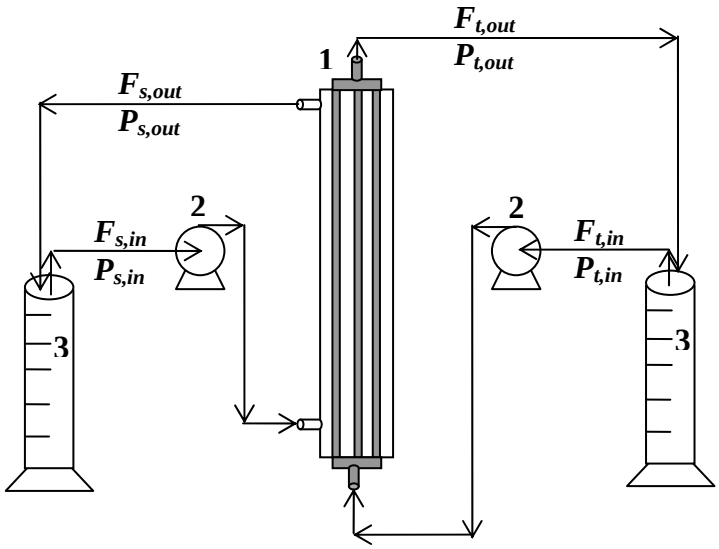

Figure 3.5: Experimental set up to study the flow across hollow fiber membranes; 1: hollow fiber membrane unit, 2: peristaltic pump, 3 gravitational cylinder, *F*: inlet volumetric flow rate (cm^3/min), *P*: pressure (g/cm.min^2). Subscript *t* stands for tube side and *s* stands for shell side. Subscript *in* stands for inlet and *out* stands for outlet.

In this section, the mathematical equations are derived to calculate the flow rates of tube and shell sides so that the pressure difference between two sides is negligible. Also, experiments were conducted to confirm these calculations.

In this set up, there are flows of tube and shell side of the membrane. It is assumed that no convective mass transfer across the membrane occurs and diffusive mass transfer across the membrane is negligible compared to convective flow in tube and shell sides. Figure 3.5 shows the experimental set up to determine the flow across hollow fiber membranes to ensure that the assumption of no convective flow is valid.

The purpose of the calculations is to determine volumetric flow rate that prevents convective mass transfer across the membrane. Therefore, inlet and outlet flow rates for each stream are assumed to be equal.

Bore side fluid flow: The flow inside hollow fiber bores or in the tube side can be modeled as flow through straight cylinder as described by Hagen-Poiseuille equation in Equation 3.6.

$$P_{t,out} - P_{t,in} = \frac{8\mu L(F_{t,in}/n)}{\pi R^4 \rho} \qquad \text{Equation 3.6}$$

where μ = viscosity (g/cm·min), L = length of the membrane module (cm), n = number of hollow fibers, R = hollow fiber bore diameter (cm), ρ = fluid density (g/cm^3).

Shell side fluid flow, the flow goes through a tube bundle and can be modeled as flow through a cylindrical tube packed with "equivalent spheres" (Bird *et al*, 2002, page 189). The pressure drop through a tube bundle can be derived as follow.

$$P_{s,out} - P_{s,in} = \frac{1}{2}\rho\langle v\rangle^2\left(\frac{L}{R_h}\right)f_{tube} \qquad \text{Equation 3.7}$$

where $\langle v\rangle$ =average velocity (cm/min), R_h=hydraulic radius (cm), f_{tube}= a friction factor of a tube. Friction factor f in the packed bed column is expressed as:

$$f = \frac{1}{4}\left(\frac{D_p}{L}\right)\left(\frac{P_{s,out} - P_{s,in}}{\frac{1}{2}\rho v_0^2}\right) \qquad \text{Equation 3.8}$$

where D_p = effective particle diameter (cm), v_0 = superficial velocity (cm/min) which is in the form of flow rate divided by empty cross section or the void fraction ε times the average velocity $\langle v \rangle$.

$$v_0 = \frac{F}{\rho S_M} = \varepsilon \langle v \rangle \qquad \text{Equation 3.9}$$

The hydraulic radius can be described in terms of the void fraction (ε) and the wetted surface a per unit volume of the bed as follows.

R_h = (cross section available for flow)/(wetted perimeter)

= (volume available for flow)/(total wetted surface)

= [(volume of voids)/(volume of bed)]/[(wetted surface)/(volume of bed)]

$$R_h = \frac{\varepsilon}{a} \qquad \text{Equation 3.10}$$

f_{tube} is a function of Reynolds number, $\mathrm{Re}_h = \frac{4R_h \langle v \rangle \rho}{\mu}$, and substitute Equation 3.7 into Equation 3.8, we get:

$$f = \frac{1}{4}\frac{D_p}{R_h}\frac{\langle v \rangle^2}{v_0^2} f_{tube} = \frac{1}{4\varepsilon^2}\frac{D_p}{R_h} f_{tube} \qquad \text{Equation 3.11}$$

Wetted surface per volume of bed (a) can be related to the "specific surface" a_v which is total particle surface per volume of particles as

$$a_v = \frac{a}{1-\varepsilon} \qquad \text{Equation 3.12}$$

The mean particle diameter (D_p) can be calculated from

$$D_p = \frac{6}{a_v} \qquad \text{Equation 3.13}$$

From the last three expressions, hydraulic radius can be expressed as

$$R_h = \frac{D_p \varepsilon}{6(1-\varepsilon)} \qquad \text{Equation 3.14}$$

Substitute Equation 3-14 into Equation 3-11, then we have

$$f = \frac{3}{2}\left(\frac{1-\varepsilon}{\varepsilon^3}\right) f_{tube} \qquad \text{Equation 3.15}$$

In a laminar flow, $f_{tube} = \frac{16}{\mathrm{Re}_h}$ for a tube of equivalent hydraulic radium, R_h. To account for noncylindrical surface and tortuous flow paths, $f_{tube} = \frac{100}{3\,\mathrm{Re}_h}$. Substitute this friction factor into Equation 3.15 and it becomes

$$f = \frac{(1-\varepsilon)^2}{\varepsilon^3} \frac{75}{(D_p \rho v_0 / \mu)} \qquad \text{Equation 3.16}$$

Substituting Equation 3.16 into Equation 3.8 we get

$$P_{s,in} - P_{s,out} = 150 L \left(\frac{\mu v_0}{D_p^2}\right) \frac{(1-\varepsilon)^2}{\varepsilon^3} \qquad \text{Equation 3.17}$$

This equation is good for $\frac{D_p \rho v_0}{\mu(1-\varepsilon)} < 10$ and ε < 0.5 (Bird *et al*, 2002, page 189). Volumetric flow rate, $F = \rho v_0 S$.

To calculate the ratio of the pressure drop in shell to tube side, Equation 3.17 is divided by Equation 3.6 and the pressure drop ratio is

$$\frac{P_{s,in} - P_{s,out}}{P_{t,in} - P_{t,out}} = 18.75 \frac{\pi R^4}{S_M D_p^2} \frac{(1-\varepsilon)^2}{\varepsilon^3} \left(\frac{F_s}{F_t / n} \right) \qquad \text{Equation 3.18}$$

In this case, the pressure drop between both sides of the membrane need to be equal or $\frac{P_{s,in} - P_{s,out}}{P_{t,in} - P_{t,out}} = 1$. Then, the ratio of the flow rate from shell to tube sides can be expressed as

$$\frac{F_s}{F_t} = \frac{1}{18.75} \frac{S_M D_p^2}{\pi n R^4} \frac{\varepsilon^3}{(1-\varepsilon)^2} \qquad \text{Equation 3.19}$$

Values of variables received from the membrane vendor are n = 520, membrane area = 4800 cm^2, fiber inner radius (R) = 0.025 cm, module outside diameter = 3.2 cm, module length (L) = 63.5 cm, void volume in shell side = 210 cm^3. Assume that the thickness of the module is 0.2 cm; then the module inside diameter = 2.8 cm. Then a certain variables are calculated.

Volume inside the module = $\pi R^2 L = \pi \left(\frac{2.8}{2} \right)^2 (63.5) = 391.00$ cm^3

$S_M = \pi R^2 = \pi \left(\frac{2.8}{2} \right)^2 = 6.16$ cm^2

ε = 210/391 = 0.54

ρ = 1 g/cm^3 for water

μ = 1.002 cP = 0.6012 g/cm.min

a = (membrane area + wall area)/(module volume) = (4800 + π(3)(63.5))/391

$a = 15.13\ \text{cm}^{-1}$

$a_v = 32.69\ \text{cm}^{-1}$

$D_p = 0.184$ cm

$\frac{F_s}{F_t} = 12.53$

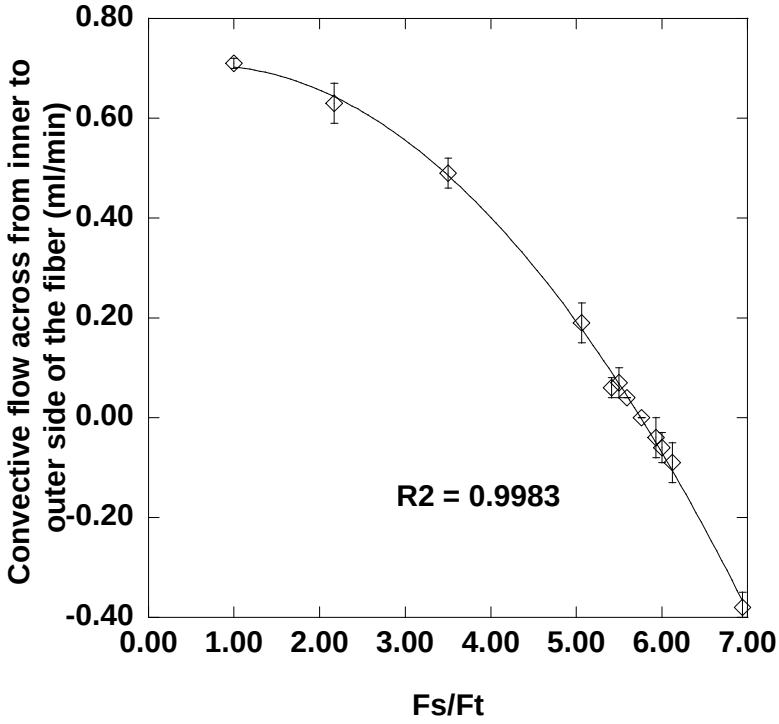

Figure 3.6: Convective flow across the hollow fiber membrane from inner (tube) side to outer (shell) side versus the flow rate ratio of shell and tube sides (F_s/F_t).

Experiments were carried out to determine F_s and F_t with the guide from calculation, F_s/F_t = 12.53, to eliminate convective mass transfer across the membrane. The experimental set up is shown in Figure 3.5. HPLC water was filled in both gravitational cylinders and the water was pumped from a cylinder to the membrane unit with various flow rates from 17 to 120 cm^3/min at 22°C. This flow rate is within laminar flow with Reynold's number = HPLC water was run to the membrane unit for 30

minutes to reach equilibrium before any measurement. After the system reached equilibrium, the levels of water in both cylinders were recorded and the time started. After a certain period of time (2 – 48 hours), the experiments were stopped and the levels of water in both cylinders were recorded. If the levels of water in the cylinder changed upon time, it means that convective mass transfer occurred. This change would not come from diffusive mass transfer because there is no chemical potential in this experiment. The experiments were repeated at least 3 times and the experimental variation is within 10%.

Experimental results show that the gain of water in one cylinder was equal to the loss of water in the other cylinder. The convective mass flow rate from tube to shell side can be calculated as the volume of transferred water divided by the time. Figure 3.6 shows the convective flow across the hollow fiber membrane from tube to shell side versus the flow rate ratio of shell to tube sides (F_s/F_t). As can be seen from Figure 3.6, the desirable value of F_s/F_t from the calculation and the experiments are not close to each other. From the restriction of Equation 3.17, $\frac{D_p \rho v_0}{\mu(1-\varepsilon)} = \frac{D_p F_s}{\mu S_M (1-\varepsilon)} < 10$ and $\varepsilon < 0.5$. It means that $F_s < 93$ cm^3/min. In the experiments, to keep $F_s<93$, F_t must be less than 7 cm^3/min to keep $F_s/F_t = 12.53$. $F_t = 7$ cm^3/min is too slow. The void volume of the tube side is 75 cm^3 and it takes 10.5 minutes to pass through the tube side. It is desirable to have the flow is as quick as possible so that the concentrations in the membrane module and the crystallizer vessels are very close. However, the flow rate could not go higher than 100 cm^3/min because the cake formation at the inlet filter gets to be significant. Again, the porosity ε of this shell side is more than 0.5. Therefore, both restrictions of Equation 3.17 are violated and therefore, it results in an inaccurate prediction. In

addition, the effects of fluid entrance and exit the membrane module were not being accounted in the development. The effects may be different in shell and bore sides of the membrane module. This could also attribute to the inaccurate prediction. Also, this could come from the fact that the membranes specifications given by the membrane vendor are not exact and some estimated membrane properties are not quite accurate. However, the calculation is still useful as a guideline for the experiments. From the experimental results, the value of F_s/F_t is set at 5.76 and F_s= 98 cm^3/min and F_t= 17 cm^3/min for future experiments.

3.2 Procedures

3.2.1 Materials

DL-glutamic acid monohydrate 99% reagent grade, D-glutamic acid 99% reagent grade, L-glutamic acid 99% reagent grade, L-aspartic acid 99% tissue culture grade, DL-leucine 99% biochemical and reagent grade, copper (II) sulfate pentahydrate 98% reagent grade, and acrylic acid 99.5% extra pure, were purchased from Acros Organics, USA. Ethylene glycol dimethacrylate, azobisisobutyronitrile HPLC grade water, and HPLC grade methanol were purchased from Fisher Scientific, USA.

3.2.2 Analysis of solution compositions

Concentrations of glutamic acid in aqueous solution and crystal products were analyzed by high performance liquid chromatography (HPLC). L-aspartic acid aqueous solution was used as an internal standard. The HPLC apparatus was purchased from Shimazu, Japan. The apparatus includes a system controller (SCL-10A), a liquid

chromatograph (LC-10AT), a degasser (DGU-14A), a UV-Vis detector (SPD-10AV), and an auto injector (SIL-10A). The chiral separation column, Chirex 3126 (D-)-penicillamine, was purchased from Phenomenex, USA. The conditions used are as follow: effluent 2.5 mM $CuSO_4$ in water 85 %v, effluent methanol 15 %v, isocratic pump, flow rate 1 ml/min, ambient temperature, detection UV-Vis-Abs- variation wave at 254 nm. Each run takes 60 minutes to analyze.

The internal standard method is used to calculate the concentration of D and L-Glu in the solution. L-aspartic acid is used as an internal standard. Figure 3.7 shows the example of HPLC analysis peaks.

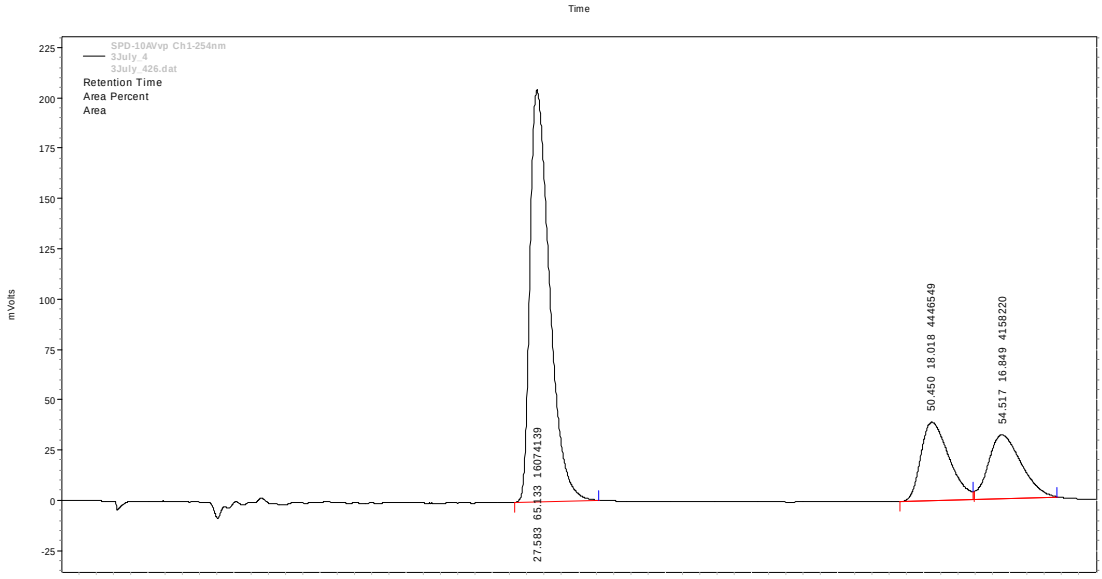

Figure 3.7: An example of HPLC analysis peaks

As shown in Figure 3.7, the first numbers on the peaks are the time that amino acid appears. The second numbers are the area under the curve of each amino acid. The third numbers are the percent of area under the curve of each amino acid. L-aspartic acid, L-Glu, and D-Glu peaks appear at around 27, 50, and 55 minutes respectively.

Glutamic acid compositions are calculated through a calibration curve. A calibration curve had to be constructed every time the column was detached from HPLC unit for accuracy. Figure 3.8 shows an example of a calibration curve. In a calibration curve, x-axis shows the ratio of area under HPLC peaks of D or L-Glu to L-aspartic acid as shown in Equation 3.20. Y-axis shows the ratio of concentration of D or L-Glu to L-aspartic acid as shown in Equation 3.21. A relationship between X and Y is linear as shown in Equation 3.22 with R^2>0.99 for all calibration curves.

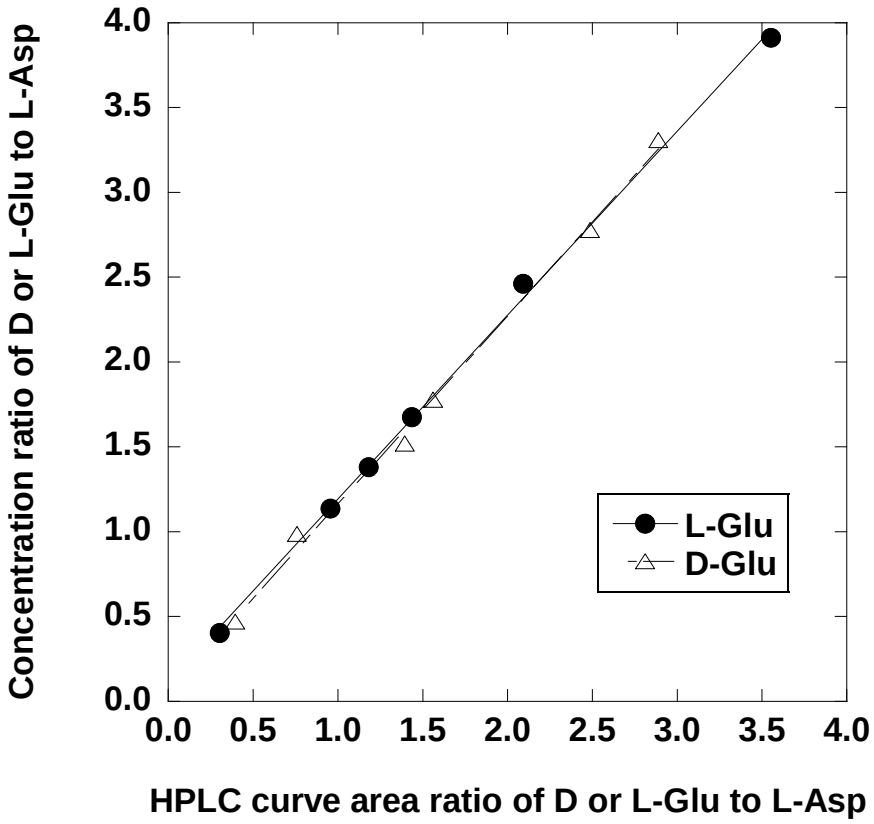

Figure 3.8: HPLC calibration curve showing the ratio of area under the HPLC curve of D or L-Glu to L-Asp versus the concentration ratio of the D or L-Glu to L-Asp in the solution mixed with internal standard, D-Glu = D-Glu, L-Glu = L-Glu, and L-Asp = L-aspartic acid.

$$X_{D-Glu} = \frac{A_{D-Glu}}{A_{L-Asp}} \text{ , } X_{L-Glu} = \frac{A_{L-Glu}}{A_{L-Asp}}$$ Equation 3.20

where X = x-values and A= area under the curve.

$$Y_{D-Glu} = \frac{w'_{D-Glu}}{w'_{L-Asp}} \text{ , } Y_{L-Glu} = \frac{w'_{L-Glu}}{w'_{L-Asp}}$$ Equation 3.21

where Y = y-values and w'= concentration of the mixed solution mixed, mother liquor mixed with internal standard (g/g solution)

$$Y_{D-Glu} = a_{D-Glu}X_{D-Glu} + b_{D-Glu} \text{ , } Y_{L-Glu} = a_{L-Glu}X_{L-Glu} + b_{L-Glu}$$ Equation 3.22

where a = slope and b = intercept.

To analyze the concentration of glutamic acid in the mother liquor solution (glutamic acid and water), the procedure is as follows. The mother liquor solution was collected through the syringe with 0.2 micron filter at the end to mix with internal standard solution (L-aspartic acid and water). The weight of the mother liquor solution sample and internal standard solution were known. The concentration of internal standard in the mixed solution could be calculated through Equation 3.23 and concentration of D or L-Glu could be calculated from Equation 3.24.

$$w'_{L-Asp} = \frac{w_{L-Asp}m_{L-Asp}}{m_{L-Asp} + m_{Solution}}$$ Equation 3.23

Where $m_{L\text{-}Asp}$=mass of internal solution (g), $m_{solution}$=mass of solution from mother liquor (g), and w= concentration of amino acid in mother liquor (g/g solution)

$$w_{D-Glu} = w'_{L-Asp}(a_{D-Glu}X_{D-Glu} + b_{D-Glu})\frac{(m_{L-Asp} + m_{Solution})}{m_{Solution}},$$

$$w_{L-Glu} = w'_{L-Asp}(a_{L-Glu}X_{L-Glu} + b_{L-Glu})\frac{(m_{L-Asp} + m_{Solution})}{m_{Solution}} \qquad \text{Equation 3.24}$$

3.2.3 Seed crystal preparation

D and L-Glu seed crystals were prepared with the same procedure. Pure enantiomer of glutamic acid was dissolved into HPLC grade-water to a weight fraction around 0.2 g/g solution at 65°C and filtered with a 0.2 μm membrane to remove impurities and undissolved particles. Then the solution was cooled down to and held at 5 °C for 24 hours with stirring. Seed crystals were collected and dried in a desiccator for 7 days. Both D and L-Glu seed crystals are needle (or plate)-like forms.

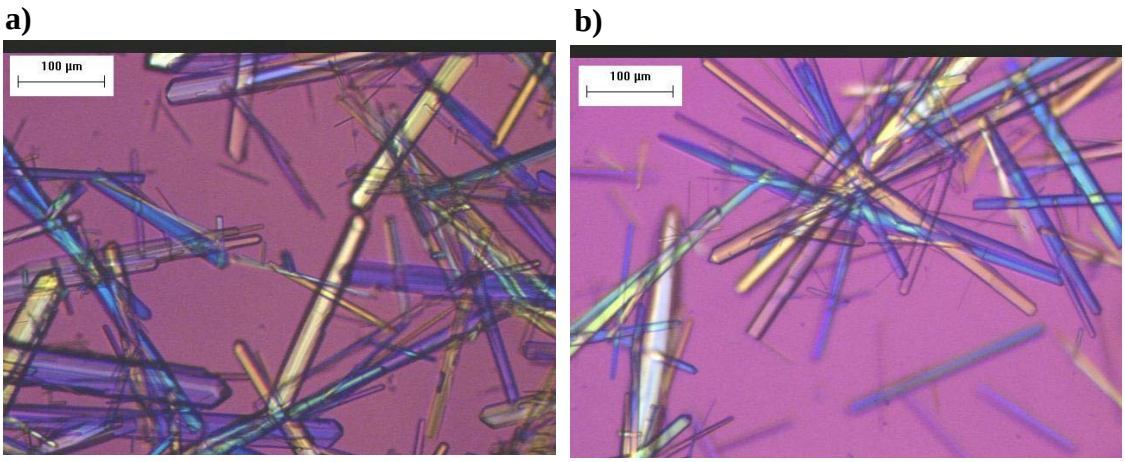

Figure 3.9: Seed crystal pictures of a) D-Glu, b) L-Glu

Figure 3.9 shows seed crystal photomicrographs of D-Glu and L-Glu. Then, crystals were sieved by sieving plates. The stack of sieving plates has the size range from <10 to 1180 μm. Each time, roughly 15 grams of crystals were put on the largest sieve plate on top of the stack. Then, the stack of sieving plates was shake by the machine for

two hours. If the time was less than two hours, the crystal size distribution would not be consistent between each batch. There are two possible explanations why it took two hours for the crystal size distribution to be consistent. First, it took two hours to ensure all the small crystals could make their way to the bottom of the sieving plates as it is hard to go through the well-packed the needle shaped crystals. Second, it took two hours to break all of larger needles into smaller pieces. The characteristic length of the crystals is not well-defined depending on the crystal orientation during sieving.

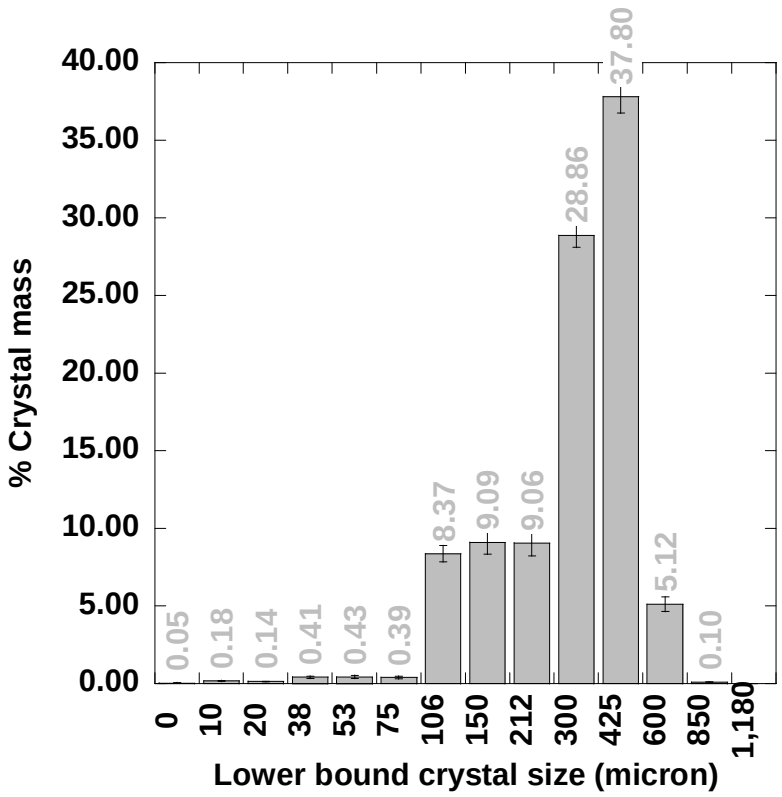

Figure 3.10: Seed crystal size distribution for the set up with a flat plate membrane, x-axis is a lower bound characteristic length of seed crystals (micron) and y-axis is the percentage of seed crystal mass.

Crystal size is in the range of <10 to 1180 μm. Over 66% is in the range of 300-600 μm. All sizes of crystal prepared were used for the set up with the flat plate membranes as it was a basic set up to prove the concept. The crystal size distribution is shown in Figure 3.10. However, the seed crystals for the hollow fiber membrane set up were selected from the range of 106 – 850 μm. size crystals are not practical to prepare because the characteristic length was not well-defined. The size range was an approximation. The reason this range was selected so that the smaller crystals could not get into the filter and the narrower seed crystal size distribution gave better repeatability of the experimental results. Even though the inlet filter has the size of 10 μm, the characteristic length of the crystals is not as well-defined as the crystal shape is needle. Therefore, to be safe, the smallest seed crystal size is 106 μm or roughly 10 times higher than the filter bores. The seed crystal size distribution is shown in Figure 3.11 for the experiments with the set up using hollow fiber membranes.

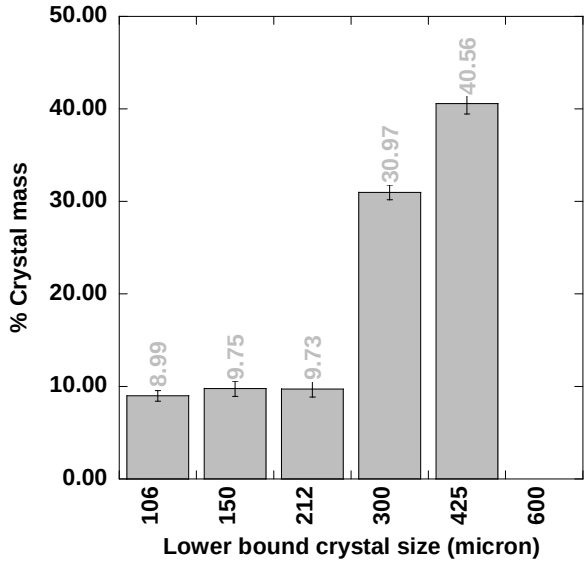

Figure 3.11: Seed crystal size distribution for the set up with a hollow fiber membrane unit, x-axis is a lower bound characteristic length of seed crystals (micron) and y-axis is the percentage of seed crystal mass.

3.2.4 Operations of the hybrid set up with a flat plate membrane

3.2.4.1 Procedures to place a membrane and seal the unit

1. After the vessels were cleaned and dried, the silicone rubber was applied to the surface of the flange of both vessels around 2 mm thick. Then, a piece of membrane was picked up with tweezers and placed on top of one of the flanges very carefully.
2. Then, both vessels were placed on an aluminum tray. Both vessels were put together by attaching the flanges together very carefully. The flanges were held by a clamp. The vessels were placed on a tray so that they did not move. The membrane is very brittle. A very small impact can break the membrane easily.
3. The tray was placed in the oven at 60^{o}C for 2 hours and placed in the ambient temperature for at least 15 hours to ensure that the silicone rubber was dried and sealed.

3.2.4.2 Procedures to transfer the solution into the vessels

After the attached vessels were placed on the stirred plate ready for the experiments, the solutions were poured into both vessels at the same time very slowly. It was important to make sure that the solution levels from both sides of the membrane were the same; otherwise, the membrane would be broken because of the pressure difference. Also, the solution should not be poured quickly because the waves could break the membrane very easily.

3.2.4.3 Procedures to transfer the solution out of the vessels at the end of the run

1. The vessels were picked up very carefully and the solutions were poured into two beakers. Do not shake the vessels to obtain all crystals. Very small waves and impact can break the membrane as it is very fragile when wet.
2. The razor blade was used with caution to unseal the flanges by inserting the blade between the flanges and move it around until the vessels detached from each other. If the silicon rubber layer was too thin, it was nearly impossible to detach the two vessels apart because there was no slit for the razor blade to cut through the silicone rubber layer. If it happened, soak the whole unit into the mixture of water and acetone 50%v for 3 days so that the rubber is swollen and can be cut through. Make sure that the blade cut through the seal over the whole flange so that the vessels can be detached easily. Forcing the glass vessels to detach can cause serious injuries by breaking the glass.
3. Once the vessels were detached, cold HPLC water at 5^{o}C were used to rinse the vessels and the crystals were collected.

3.2.4.4 Procedures to clean up the unit

Once all the crystals recovered, the flanges of the vessels were put into the ice bucket to harden silicone rubber for 30 minutes. Then, the spatula was used to remove hard silicone on a flange surface. Do not scratch the flange surface because it may cause a rough surface and could create problems with sealing in the future. Afterward, the vessels were rinsed with deionized water and dried in the oven.

3.2.5 Operations with the hybrid set up with the hollow fiber membranes

In general, the unit can be easily assembled and maintained. The major maintenance of this unit is to clean the hollow fiber membrane module. As shown in Figure 3.3, the vessels can be easily cleaned by rinsing with deionized water. However, the procedure for cleaning the hollow fiber membrane module is more complicated and is shown as follows.

1. After the experiments were done, 3000 cm^3 of HPLC water at 50^oC were pumped to the module at the bottoms of both the shell and tube sides with a flow rate of 1 cm^3/min. The temperature was kept at 50^oC to ensure the fine particles crystallized inside the membrane were dissolved. However, the temperature cannot exceed 50^oC due to the membrane restriction. The flow rate was kept at 1 cm^3/min to provide sufficient resident time to dissolve the fine particles.
2. Then, 2000 cm^3 of HPLC water at 50^oC was pumped to the top of the module of both the shell and tube sides with a flow rate 250 cm^3/min to flush out the fine particles to the bottom. However, the fine particles were not observed. Some nuclei could be infinitesimal but can cause crystallization of an undesired product. As the HPLC water came out from the inlet filter, this step also pushed out some fine crystals stuck inside the inlet filters as because of reverse flow.
3. The membrane module was left alone for at least 12 hours to allow the HPLC liquid adsorbed in the hollow fiber membranes to desorb and drip to the

bottom of the module. Then this water was sucked out from the module by the peristaltic pump. The adsorbed water was roughly 50 – 60 cm^3 in total.

4. Inlet filters were soaked in 500 cm^3 of HPLC water at 80^oC for 120 minutes to dissolve fine particles that might be left inside the filters.

CHAPTER 4

SOLUBILITY AND METASTABLE LIMIT MEASUREMENTS

It is crucial to know solubility and metastable limits that govern the crystallization process as stated in section 2.1.3. In this chapter, experiments were carried out to measure the solubility concentrations and metastable concentrations at cooling rates of 0.2, 0.5, 1, 5, and 10^{o}C/h.

4.1 Experiments

A DL-Glu aqueous solution was prepared by dissolving DL-Glu monohydrate in HPLC grade water with the weight fraction ranging from 0.0010 to 0.0045 g DL-Glu anhydrous/g solution at a temperature higher than its average solubility temperature from the literatures (Apelblat and Manzurola, 1997; Dalton and Schmidt, 1933). The solution was filtered with 0.2 μm membrane to remove impurities and undissolved particles. The solution temperature was controlled by a programmable heating/cooling bath and recorded by the LabView program. Each data point had at least four repetitions and the variation was less than 6% of the average temperature in ^{o}C.

For metastable limit measurements, the solution was cooled from 5.0^{o}C above its solubility at rates of 0.2, 0.5, 1.0, 5.0, and 10.0^{o}C/h. Light was directed through the vessel to determine if crystals formed. The Tyndall effect is the visual observation of light scattering of particles in a colloidal system such as suspensions. This phenomenon confirms that primary nucleation takes place at this temperature. For this system, an enormous amount of particles must be seen at the temperature to be considered as a

metastable limit temperature. There were some particles smaller than 0.2 μm in the system and they could be seen in the solution.

Utilizing the Tyndall effect differs from other research groups and resulted in determination of the metastable temperatures that were a few ^{o}C higher than previous determination. Reproducibility of the results were also improved using the Tyndall effect.

The solubility concentration is generally measured by adding a little amount of solid each time to the isothermal solution in a stirred tank. When the solid can be no longer dissolved, that concentration is the solubility. In this work, the solubility was measured by heating the solution at a constant concentration at 2°C every hour until the solution became clear. When the solution was clear, the temperature was recorded as the solubility temperature. The solution used here was the solution that formed crystals in the metastable limit measurement. The aim of our measurement was to confirm the data received from the literature. The observation of the solution clarity was also aided by a light directed through the vessel.

4.2 Results and Discussions

Solubility data obtained from this study fall between the data from Dalton and Schmidt (1933) and Apelblat and Manzurolo (1997) as shown in Figure 4.1.

Figure 4.2 shows the solubility and the metastable limit concentrations of DL-Glu based on one enantiomer at cooling rate of 0.2, 0.5, 1.0, 5.0, and 10.0^{o}C/h. As can seen from Figure 4.2, the faster the cooling rate, the higher the metastable concentrations. As stated in section 2.1.3, the solute needs a certain period of time to move around in the

solution to attract the other solute molecules to form a crystal. With the same given period of time, the system reaches the metastable limit temperature at that given solute concentration at lower temperatures if the cooling rate is faster. As shown in Figure 4.2, the metastable zone width of the system with a cooling rate of 0.2°C is very narrow and it creates great difficulties to pursue preferential crystallization. Both solubility and metastable limit concentrations have exponential relationships with temperature. The data in Figure 4.2 are plotted as ln x versus T^{-1} in Figure 4.3. The plots of ln x versus T^{-1} are shown to be linear with R^2>99%. As shown in Equation 2.15, $\ln x = -\frac{\Delta H_d}{RT} + \frac{\Delta S_d}{R}$, the values of ΔH_d and ΔS_d are calculated from the slope and intercept of the solubility curve in Figure 4.2. ΔH_d and ΔS_d equal to 29.83 kJ/mol and 0.05 kJ/mol·K respectively.

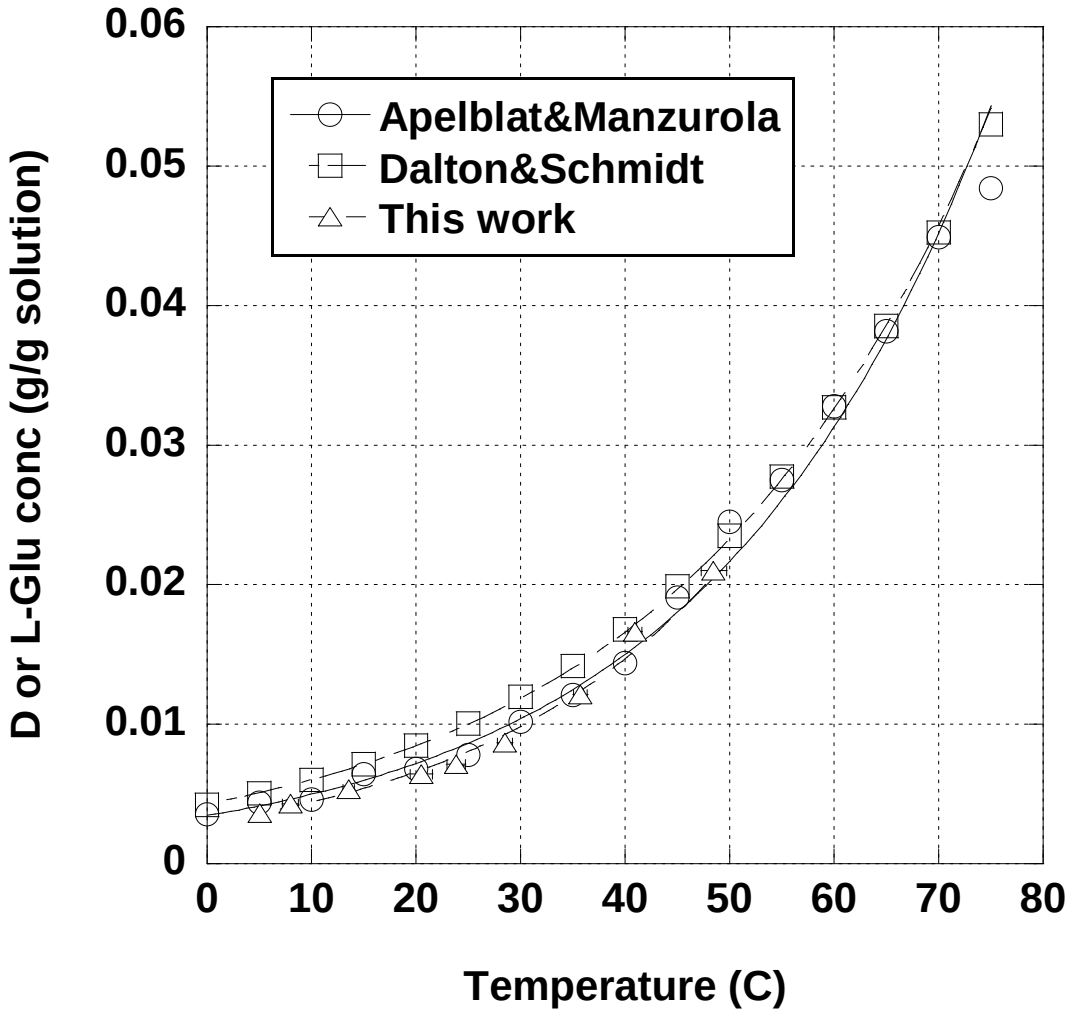

Figure 4.1: The solubility concentrations of DL-Glu based on concentrations of only one enantiomer versus temperature from Apelblat and Manzurola (1997), Dalton and Schmidt (1993), and this work.

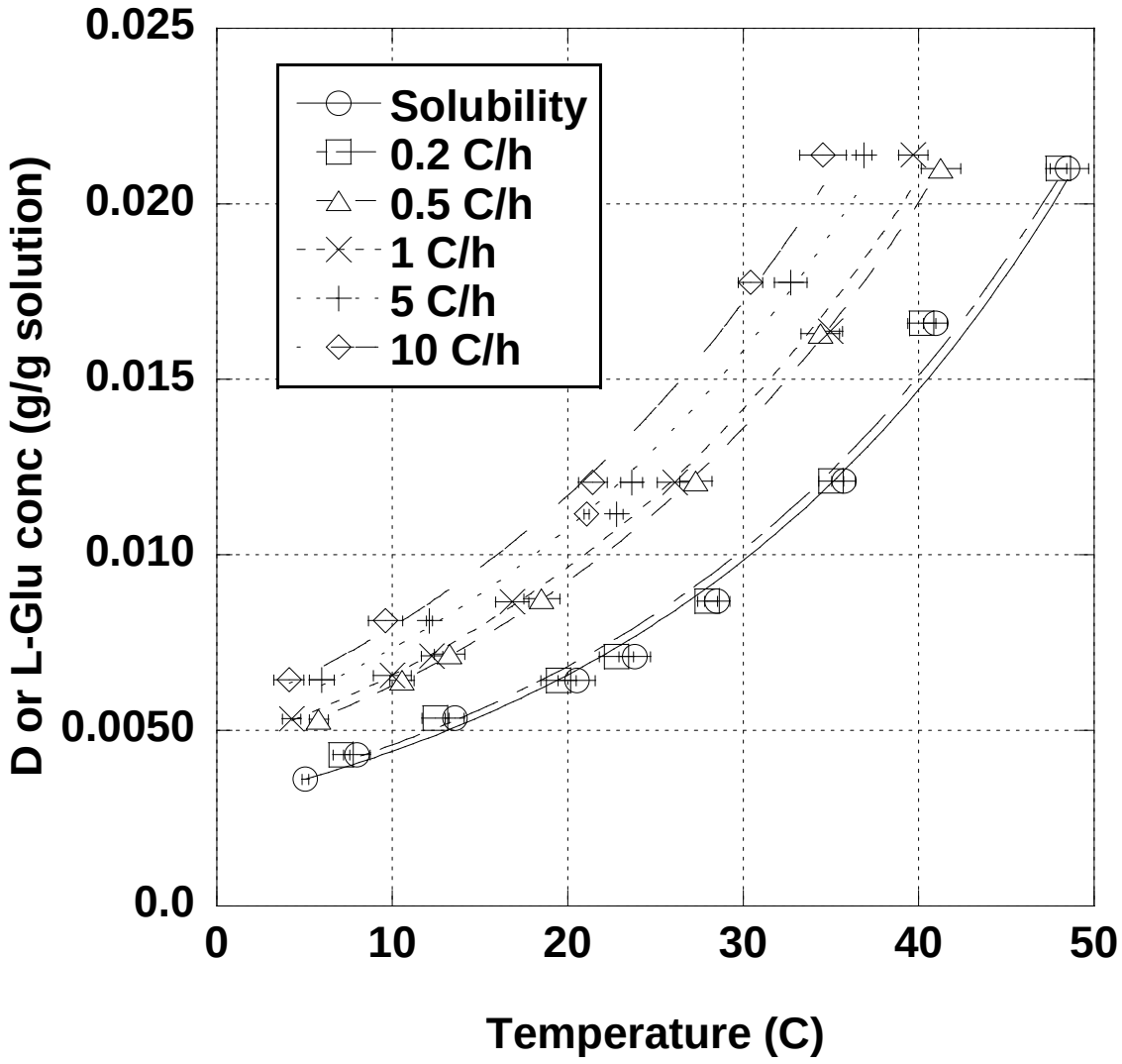

Figure 4.2: DL-Glu concentrations based on one enantiomer versus temperature. The concentrations are at the solubility and metastable limit with cooling rates of 0.2, 0.5, 1.0, 5.0, 10.0°C/h

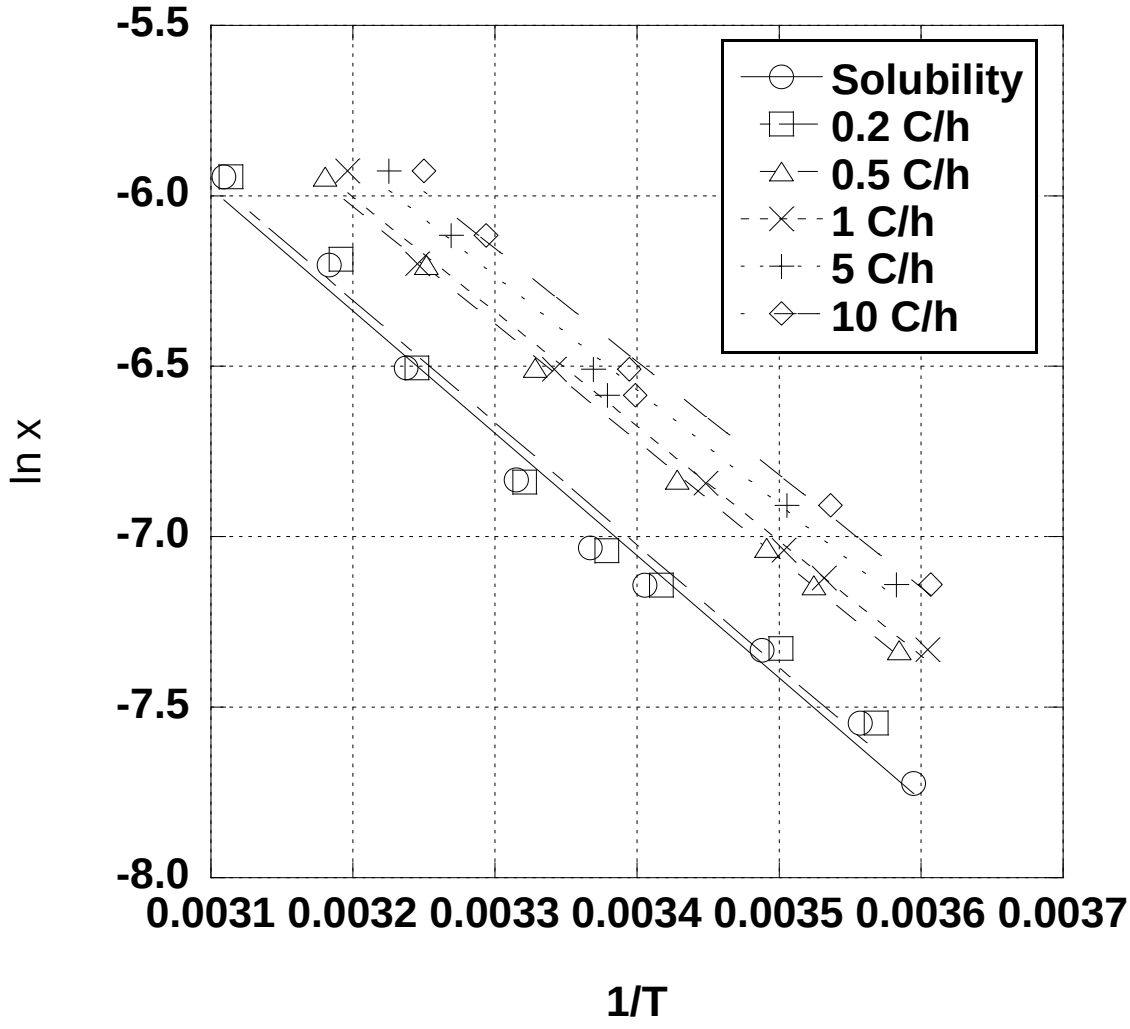

Figure 4.3: The plot of ln x versus T^{-1} (K^{-1}) of the concentrations at the solubility and metastable limit with cooling rates of 0.2, 0.5, 1.0, 5.0, 10.0 $^{\circ}$C/h

4.3 Conclusions

Experiments were carried out to measure the solubility and metastable limit of DL-Glu. The measurement method here was different from typical methods with bare eye observation which could be biased depending on how exhausted the eyes were after a long observation. The aid of flash light was used to observe Tyndall's effects to detect the change of solution visibility. The aid of the flash light helped reduce the experimental variation. The experimental variation was less than ±6% of the average values. The measured solubilities from this work were close and within the same range as the literatures (Apelblat and Manzurola, 1997; Dalton and Schmidt, 1993). It was observed that the metastable gap increased as the cooling rate increased. Both solubility and metastable limit concentrations performed exponential relationships with temperature as expected.

CHAPTER 5

BASIC CHIRAL SEPARATION THROUGH A HYBRID PROCESS

This chapter describes a novel chiral separation technique that combines preferential crystallization with a flat plate membrane barrier for DL-Glu resolution. The flat plate membrane was used as a physical barrier for this simple set up to show the feasibility of the novel process. The process utilizes two crystallization vessels that are separated by a membrane that prevents transport of crystals from one vessel to another. The objective of these experiments is to maximize the product yield and purity. Experiments were conducted to study the effect of the seed crystal mass on the product yield and purity. A different seed mass provides different surface area for the solute to grow on top of the crystals. The seed mass is divided by a crystallizer volume to show how much seed mass is invested in a given volume of a crystallizer. Two seed mass levels, 3.50 and 22.20 g/dm^3 crystallizer, were studied. In these experiments, the temperature of the solution decreased from 40 to 37^{o}C at 1.0^{o}C/h and stayed at 37^{o}C for 7 hours to study how fast the crystal grew. The overall growth rate coefficient, K_G, in Equation 2.4 was estimated in this chapter for the future use in an advanced study.

5.1 Experiments

The experimental set up is shown in Figure 3.1. An aqueous solution of DL-Glu was prepared by dissolving DL-Glutamic monohydrate into HPLC grade water at 80 °C with a concentration of 0.033 to 0.035 gram of DL-Glutamic per gram of solution. The

solution was filtered through a membrane with 0.2 μm pores to remove impurities and undissolved particles. Each crystallizer contained averagely 642 cm^3 of solution.

A clear DL-Glu aqueous solution that had a concentration corresponding to saturation at 40 °C, was cooled from 80 to 41 °C. Then the solution was cooled from 41 to 37 °C with a cooling rate of 1.0°C/h and held at 37°C for 10 hours. D and L seed crystals of glutamic acid were introduced into Vessel 1 and Vessel 2, respectively, at 40°C. The seed crystals were prepared in section 3.2.3 and the size distribution is shown in Figure 3.10. The amount of the enantiomer seed crystals was approximately 22.20 g/dm^3 crystallizer for high-seed-mass runs and 3.50 g/dm^3 crystallizer for low-seed-mass runs. The starting time for a run was defined to be when the solution reached 40°C. Samples were withdrawn throughout the run by using a syringe with a 0.2-μm filter and mixed with internal standard for composition analysis. The final product crystals were filtered, dried, and weighed. They were then rediscover in water, filtered, and analyzed by HPLC. The HPLC analysis procedure is followed in section 3.2.2. Each run was repeated multiple times to determine a standard deviation that is used in the analysis of experimental results.

5.2 Results and Discussions

The analyses of liquid samples taken in the high-seed-mass runs are shown in Figure 5.1, while those taken in the low-seed-mass runs are shown in Figure 5.2. Figures 5.1 and 5.2 show the average solute concentrations ± standard deviation versus time. The figures also show the solubility of D- and L-Glu. There are three sources of solubility data: Apelblat and Manzurola (1997), Dalton et al (1933), and the present work. For the

sake of consistency, the solubility data presented in Figure 5.1 and Figure 5.2 are from the present work.

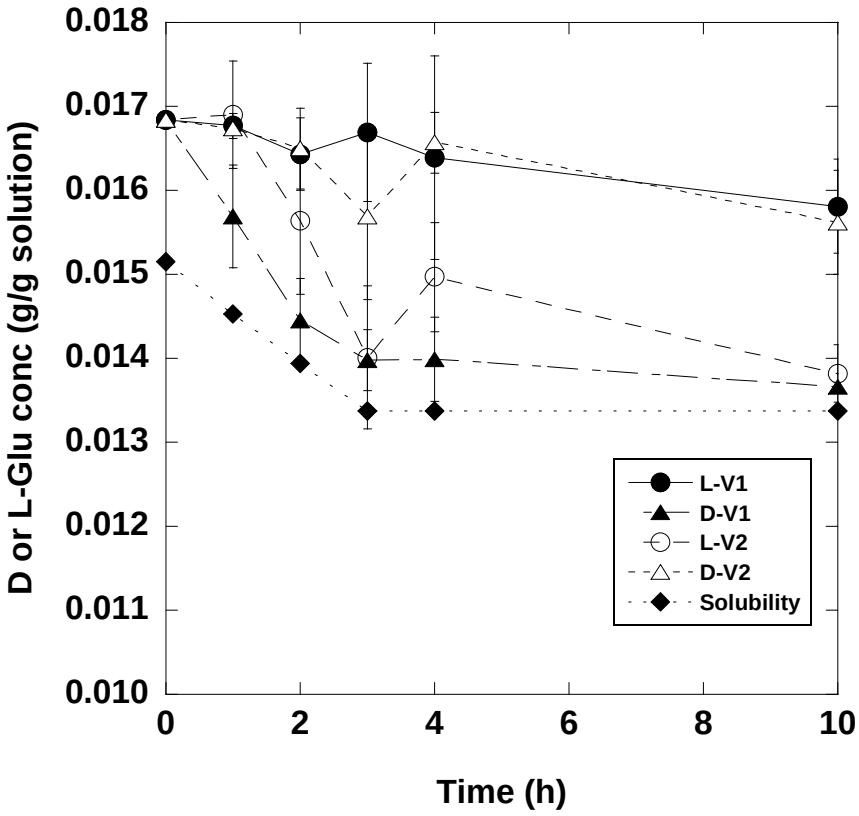

Figure 5.1: Solution concentrations of D-Glu and L-Glu and solubility in high-seed-mass experiments.

Both sets of runs resulted in higher concentrations of L-Glu in the solution of Vessel 1 while higher D-Glu concentration was found in the solution of Vessel 2. As a run progressed, the concentration of the seeded enantiomer decreased in the vessel to which such seed crystals had been added: e.g. D-Glu in Vessel 1 and L-Glu in Vessel 2. The concentrations of the non-seeded enantiomer remained high and showed little decrease during a run. This undoubtedly was due to the difference in the rate of the

crystallization, with the concomitant reduction in concentration of the crystallizing species, and the rate of membrane transport of the non-crystallizing species; e.g. considering Vessel 1, the concentration of D-Glu decreased substantially as it grew on the seed crystals, while the concentration of L-Glu remained high. The consistency of the data is supported by the observation that none of the measured enantiomer compositions was lower than the solubility.

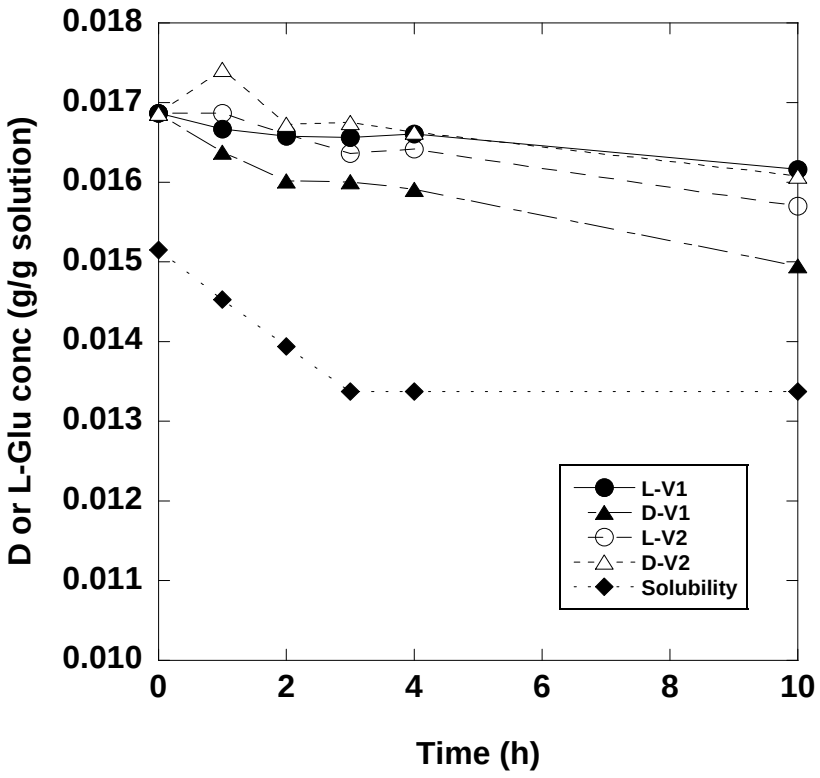

Figure 5.2: Solution concentrations of D-Glu and L-Glu and solubility in low-seed-crystal-mass experiments.

Comparison of the data in Figure 5.1 and Figure 5.2 shows that the mass of added seeded crystals had a significant impact on the rate at which the concentration of the

seeded species decreased: i.e., as expected, the higher mass of seed crystals led to a more rapid decrease in concentration. This undoubtedly is because of the greater surface area for the high-seed-mass experiment.

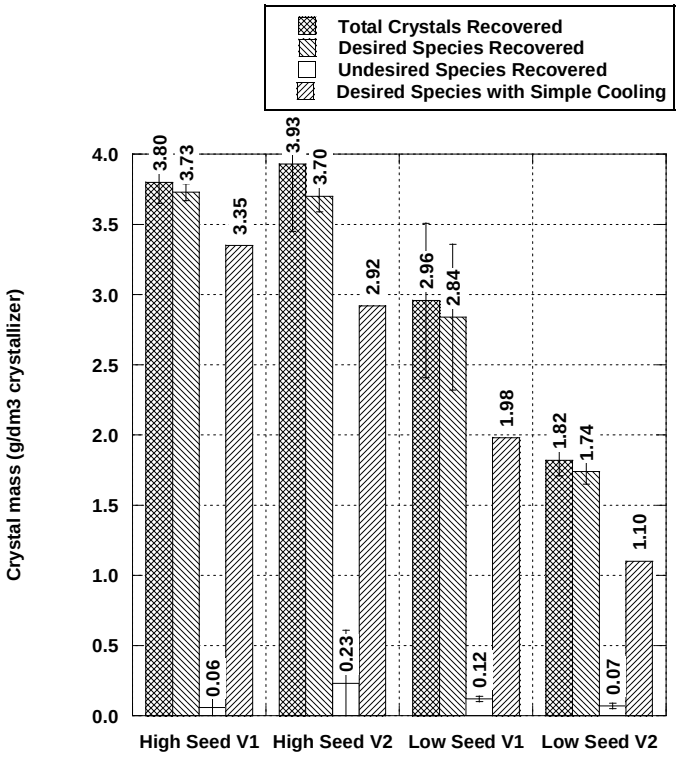

Figure 5.3: Glutamic acid crystal mass recovered from high-seed-mass and low-seed-mass runs. Total is the mass of recovered crystals; desired product is recovered mass of seeded species; undesired product is recovered mass of unseeded species; mass of desired species with simple cooling is determined from solution concentrations and Equation 5.2.

To analyze these experiments further, the crystal product quantity and purity were evaluated. The product purity from all experiments was analyzed by HPLC and ranged from 94 to 98%, which corresponds to a separation factor of 16 to 60. Separation factor, α, can be calculated from Equation 5.1. This separation factor was higher than chiral separations reported in the chiral selective membrane systems (Gumi et al., 2005a, 2005b;

Hadik et al., 2005), which had separation factors of 5.7 at most. It shows that our hybrid process produced higher purity product than the membrane process alone.

$$\alpha = \frac{\left(w_{desired} / w_{undestired} \right)_{product}}{\left(w_{desired} / w_{undestired} \right)_{feed}} \qquad \text{Equation 5.1}$$

α = separation factor and w = weight fraction.

The amounts and purities of product crystals from the two sets of runs are shown in Figure 5.3. The masses of product shown are the average values ± standard deviation. The desired products are D-Glu from Vessel 1 and L-Glu from Vessel 2. The masses of the desired crystal products in the high-seed-mass runs were nearly the same (3.74 g and 3.69 g/dm^3 crystallizer) and higher than low-seed-mass runs (2.83 and 1.74 g/dm^3 crystallizer), again confirming the higher seed-crystal surface area had a significant influence on the crystallization rate. For the low-seed-mass runs, however, the total crystal masses from two vessels were different (2.83 and 1.74 g/dm^3 crystallizer), perhaps reflecting greater variability in system performance when the mass of seed crystals is low. The amounts of undesirable crystals from both sets of runs were small and less than 6% of the total mass collected.

An important feature of this novel process is that it produces a higher yield of desired products than what would be obtained by simple preferential crystallization. In analyzing the results from the runs summarized above, recognize that crystals of the desired product from a seeded vessel could include mass from the original solution in that vessel and mass transferred from the unseeded vessel through the barrier membrane. In other words, seeding Vessel 1 with crystals of D-Glu would result in a mass of desired crystals (D-Glu, m_D) corresponding to the exhibited difference in solution concentrations

between the beginning and end of the run: i.e. expressing the desired species as component *i*

$$M_i = m_{sol}(w_{i,initial} - w_{i,final}) \qquad \text{Equation 5.2}$$

However, as demonstrated in the following analysis, the new process results in additional solute being transported across the membrane from Vessel 2 to produce a mass of desired product greater than that given by Equation 5.2.

The bar chart in Figure 5.3 shows the average total crystal mass recovered from the vessels at the end of the two sets of runs and the average amounts of desired and undesired species as determined by analysis of product samples. The average amounts of the desired species that would have resulted from simple cooling (i.e. in a vessel) were calculated from Equation 5.1 and also are shown on the bar chart. The important points in the figure are that in all instances (1) the crystals recovered were overwhelmingly of the desired species and (2) the yield of desired species was significantly greater than that of simple preferential crystallization. These results are summarized in Table 5.1.

Table 5.1 also shows the ratio of the product mass to the maximum product mass. The maximum possible product mass was the mass available for crystallization and could be calculated as:

$$M_{i,\max} = (m_{sol,V1} + m_{sol,V2})(w_{i,initial} - w^*_{i,final}) \qquad \text{Equation 5.3}$$

In these experiments, $M_{i,\max}$ was equal to 6.99 g/dm^3 crystallizer. From Table 5.1, the ratio was relatively in the same range except the lower one from V2 in the low-seed mass experiments as their product mass recovery was the least. A possible explanation was that V2 (572 cm^3) was smaller than V1 (712 cm^3); therefore, the amount of mass crystallized would be less. Another impact could come from that the amounts of final

product from low-seed-mass experiments were very small. Very little mass loss could have a strong impact on the average mass product.

The key feature of this process was the product recovery would be greater than the product from preferential crystallization itself. The yield enhancement from preferential crystallization could be calculated from Equation 5.4.

$$\textbf{\textit{Yield enhancement}} = \frac{(Yield_{hybrid} - Yield_{crystallization})}{Yield_{crystallization}} x100 \qquad \text{Equation 5.4}$$

As shown in Table 5.1, the yield enhancements from the low-seed-mass experiments were higher than the high seed mass experiments. This is because the denominator of low-seed-mass experiments was lower in Equation 5.3. The enhancement was up to 65% which was a great improvement.

Table 5.1: Purity and recovery of desired enantiomers

Seed Mass	High		Low	
Vessel	V1	V2	V1	V2
Purity of Desired Species	98.4%	94.1%	96.1%	95.9%
Ratio of the product mass to the maximum product mass	0.53	0.53	0.41	0.26
Yield enhancement	13%	27%	43%	65%

5.3 Estimation of the overall growth rate coefficient

The overall growth rate coefficient, K_G, was estimated here for further use of mathematical modeling to predict and to plan the experiments in the future. K_G is the

only unknown parameter in mathematical equations in section 2.5. The procedure to estimate K_G is as follows and the R code is presented in Appendix D. The mass transfer coefficients due to diffusion and surface integration, k_c and k_r, and were estimated from K_G from Equation 2.4. It would be determined later on whether the process was controlled by diffusion or surface integration.

1. The experimental values of solute concentrations were plotted against temperature for both low and high seed mass experiments.
2. The regression equations of the solute concentration against temperature were created from experimental data.
3. The value of K_G was guessed. Then, mathematical simulations were carried out according to the guessed K_G. The plots of solute concentration versus temperature were generated from mathematical equations in section 2.5 for both low and high seed mass experiments.
4. The guessed value of K_G was changed to minimize the mean square error (*MSE*) of the difference in the solution concentration values from the regression of the experiments and the model or to minimize the summation of *MSE* as shown in Equation 5.6.

$$MSE = \sqrt{\sum_{j=1}^{n} \frac{(w_{ex,j} - w_{md,j})^2}{n}} \qquad \text{Equation 5.5}$$

$$\min \sum_{i=1}^{4} MSE_j = \sum_{i=1}^{4} \sqrt{\sum_{j=1}^{n} \frac{(w_{ex,j} - w_{md,j})^2}{n}} \qquad \text{Equation 5.6}$$

Where $w_{ex,j}$ = solution concentrations from the regression of the experimental values, $w_{md,j}$ = solution concentrations from the mathematical model, n =

number of data, j = index of the data point, i = index of the species, i.e. L-V1, i = 1; D-V1, i = 2; L-V2, i = 3; D-V2, i = 4.

5. Once the *MSE* of experiments from both high and low seed mass experiments were minimized; then, the value of K_G was obtained. K_G could be a function of the amount of seed mass.

The simulations were carried out by varying K_G from 0.000025 to 0.25 cm/min. The simulated solution concentrations were plotted against temperature and compared with the experimental data. Figure 5.4 and 5.5 show the plot for low-seed-mass experiments while Figure 5.6 and 5.7 show the plot for high-mass-experiments in Vessel 1 and 2. As can be seen from Figure 5.4 through 5.7, the concentrations of crystallizing species (D-Glu for V1 and L-Glu for V2) changed significantly with the change of K_G. The concentrations barely changed for very low K_G of 0.000025 cm/min as the crystals grew at very slow rate while the concentrations dropped to the solubilities very quickly at very high K_G of 0.25 cm/min as the crystals grew at very fast rate. The concentration for non-crystallizing species (L-Glu for V1 and D-Glu for V2) did not change importantly with K_G. Even though the driving force or the concentration differences between two vessels were very high at very high K_G of 0.25 cm/min, the non-crystallizing species could not diffuse across the membrane quick enough to bring the its concentration down. It can be concluded that the membrane surface area was insufficient and need to be increased and the mass transfer resistance due to the membrane was important.

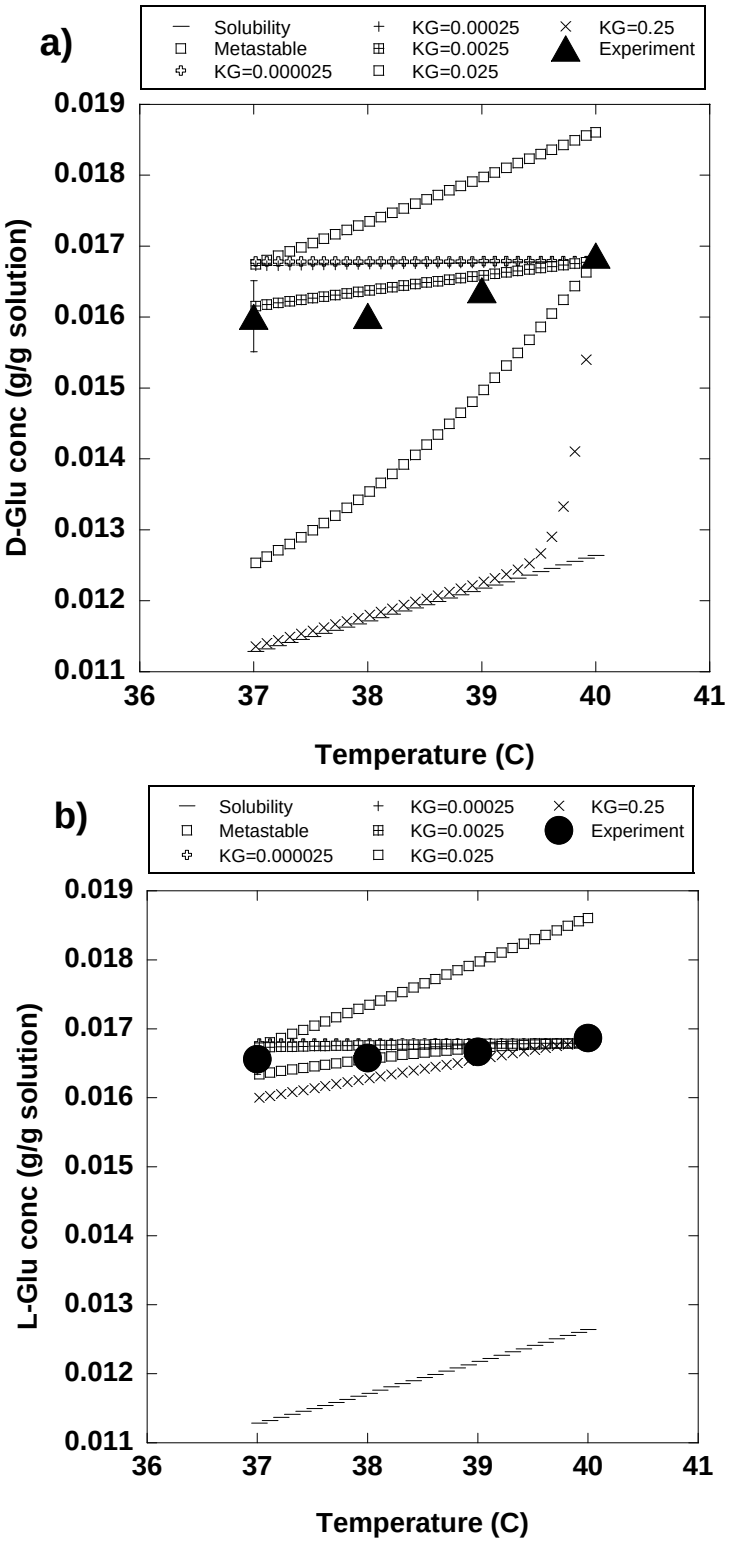

Figure 5.4: Experimental and simulated concentrations in Vessel 1 of D-Glu (a) and L-Glu (b) for low seed mass experiments with K_G = 0.000025, 0.00025, 0.0025, 0.025, and 0.25 cm/min.

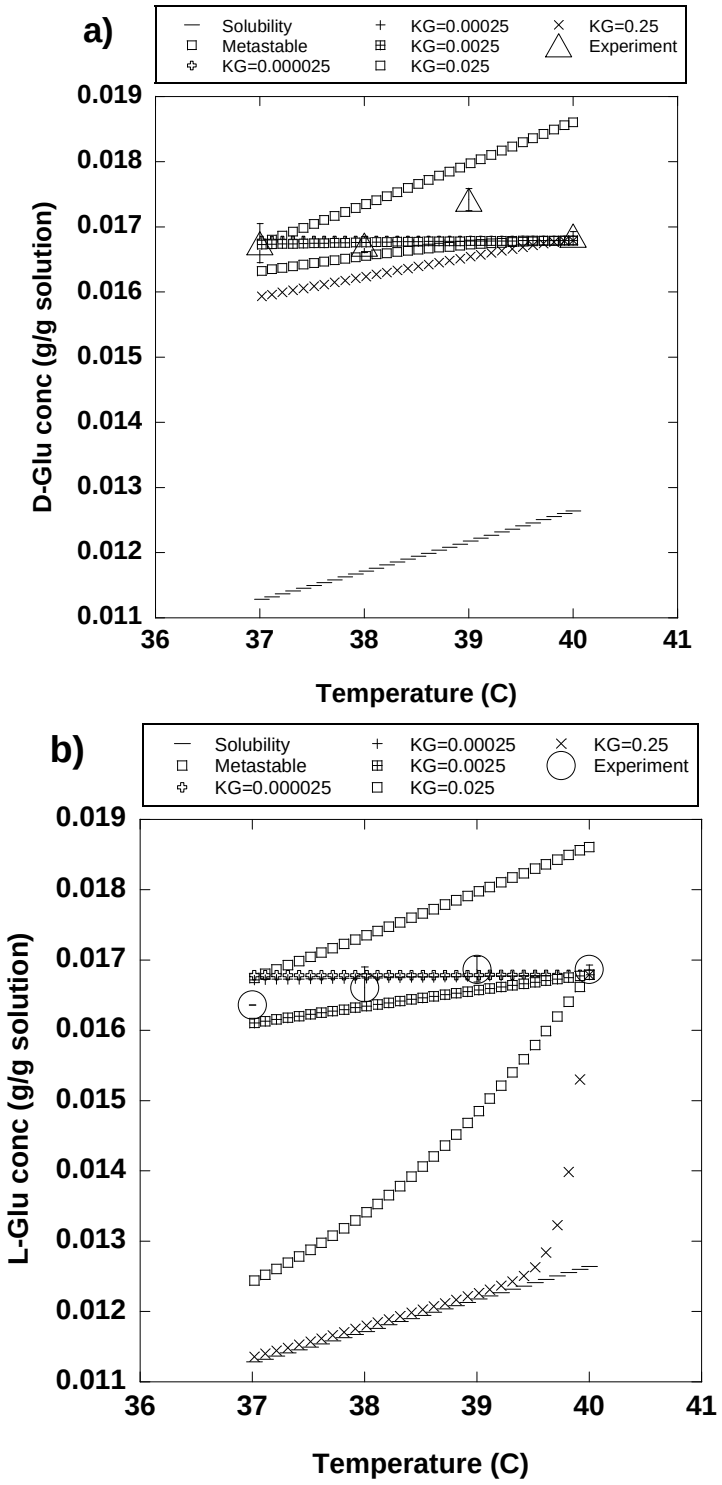

Figure 5.5: Experimental and simulated concentrations in Vessel 2 of D-Glu (a) and L-Glu (b) for low seed mass experiments with K_G = 0.000025, 0.00025, 0.0025, 0.025, and 0.25 cm/min.

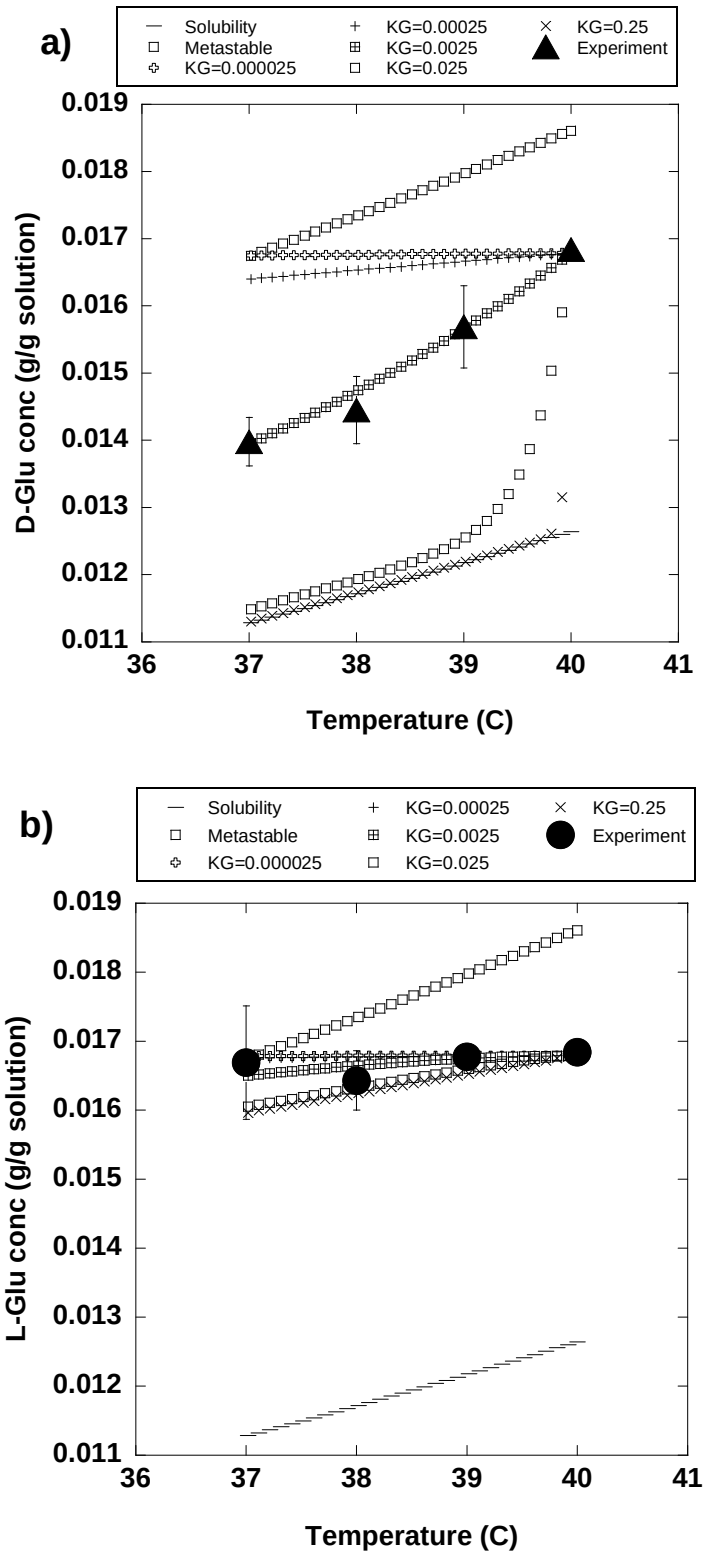

Figure 5.6: Experimental and simulated concentrations in Vessel 1 of D-Glu (a) and L-Glu (b) for high seed mass experiments with K_G = 0.000025, 0.00025, 0.0025, 0.025, and 0.25 cm/min.

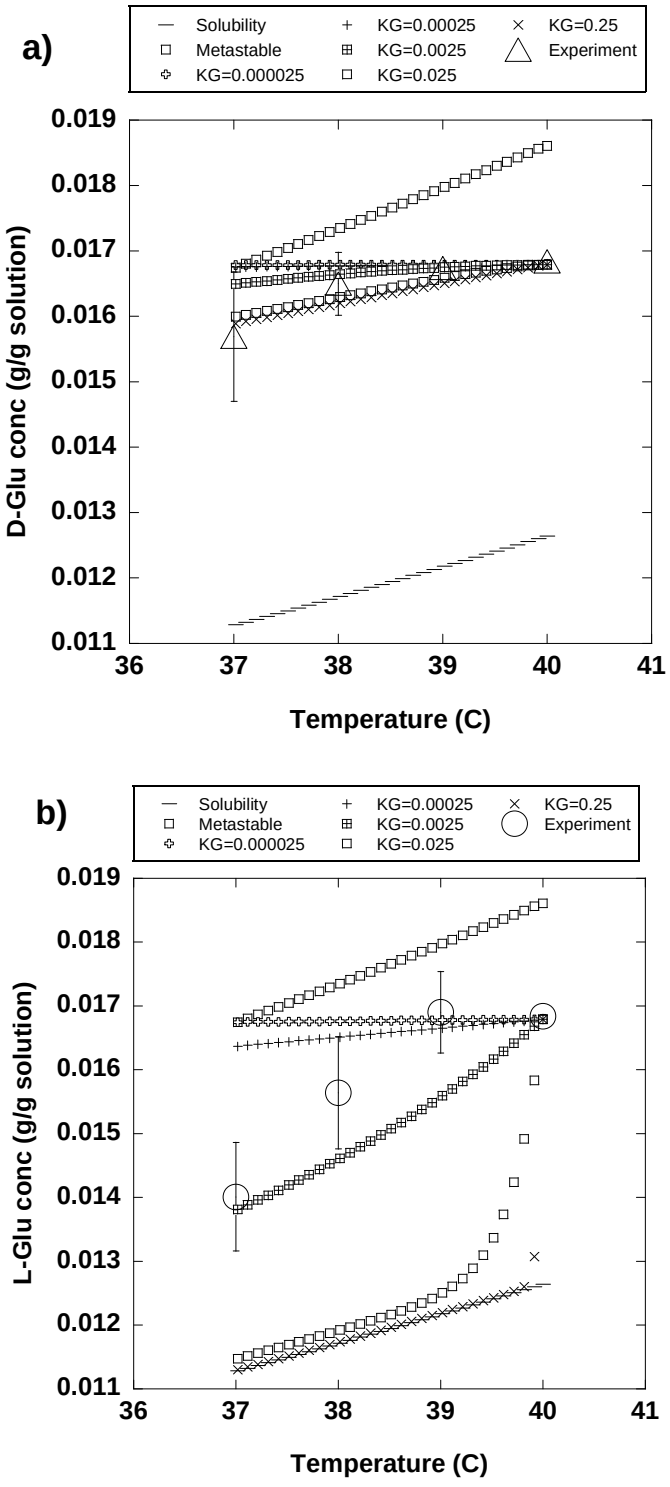

Figure 5.7: Experimental and simulated concentrations in Vessel 2 of D-Glu (a) and L-Glu (b) for high seed mass experiments with K_G = 0.000025, 0.00025, 0.0025, 0.025, and 0.25 cm/min.

K_G = 0.0025 cm/min fitted the data the best for both low and high-seed mass experiments. With the K_G equal 0.0025 cm/min, $\sum MSE$ = 7.07×10^{-5} g/g solution or 0.42% of initial concentrations for low-seed-mass experiments and 9.19×10^{-5} g/g solution or 0.55% of initial concentrations for high-seed-mass.

At K_G = 0.0025 cm/min, the concentrations of crystallizing species did not reach equilibrium value or its solubility. Therefore, the mass transfer resistance due to crystal growth is important and can be reduced by the increase of crystallizing surface area or the seed mass. The mass transfer resistance due to crystal growth consists of the resistances from diffusion and surface integration. These resistances can be decoupled from the value of K_G.

The estimated K_G is the maximum value of the actual K_G as proved in section 2.5. k_c was estimated from Harriott (1962) to be equal to 0.2975 cm/min at 25°C and was expected be higher at 37 – 40°C as shown in Equation 2.10. If the surface integration growth rate order, r, is assumed to be one, k_r can be estimated from Equation 2.4 and is equal to 0.0025 cm/min. This estimated k_r is the maximum value of k_r as the estimated K_G is the maximum value. k_c is 120 larger than the maximum k_r; therefore, the process is controlled by the surface integration not the bulk diffusion. If k_c > 0.2975 cm/min as the temperature higher than 25°C, k_r is still expected to be 0.0025 cm/min as k_c is much larger than k_r. k_c and k_r can assumed to be a constant within a short temperature range, 37 – 40°C.

5.5 Conclusions

A novel chiral separation process combining preferential crystallization and a membrane barrier was proposed and demonstrated using the resolution of DL-Glu as a model system. The product purities were more than 94%, corresponding to the separation factor of 16, and the product yield was increased by as much as 65% compared to simple preferential crystallization. The high-seed-mass runs produced greater product yield than the low-seed-mass runs due to the larger seed crystal surface area. Although not explored in this chapter but next chapter, the results demonstrate the importance of matching the solute transport rate with crystal growth rates in order to maximize crystal yield, minimize run time, and enhance crystal purity. The overall mass transfer coefficient, K_G, was estimated for further use in an advanced studied. It was found that the mass transfer resistances from the membrane and the surface integration were important.

CHAPTER 6

ADVANCED CHIRAL SEPARTION THROUGH A HYBRID PROCESS

Chiral separation through hybrid of preferential crystallization modified by a membrane barrier showed the process is promising in chapter 5. In this chapter, the process variables were explored in more detail at the conditions beyond feasible in Chapter 5, i.e. cooling of a larger temperature range. As previous process limitations were reduced significantly, i.e. transmembrane transport resistance, in this chapter, much higher product yield and purity were expected here.

The hollow fiber membrane, which is more robust, was used in this chapter. The hollow fiber membrane allowed higher transmembrane mass transport as the membrane area increased significantly from a flat plate membrane. The transmembrane mass transport increased for both the import of desired species and the export of undesired species. The increase of transmembrane mass transport allowed cooling of a larger temperature range as the undesired species would not reach metastable limit. Therefore, the increase of product yield and purity was expected.

This new set up consisted of two crystallization vessels and a hollow fiber membrane module as shown in Figure 3.3. The solution in the vessels flowed to the membrane module through the peristaltic pumps. The operating conditions were controlled so that a pure species crystallizes in each vessel. Experiments were carried out with different amounts of seed crystals (13.98, 10.09, 25.22, 78.87 g/dm^3 crystallizer) and different cooling rates (0.5, 1.0, and 5.0^{o}C/h) to determine operating conditions that produce the highest product yield and purity. The seed mass is divided by a crystallizer

volume to show how much seed mass is invested in a given volume of a crystallizer. The product mass and the membrane surface area are also given in the unit compared to a volume of crystallizer, i.e. g seed mass/dm^3 crystallizer and cm^2 membrane area/ dm^3 crystallizer. The seed crystal surface area which depends on the amount of seed mass has significant effects on crystal growth and secondary nucleation. A cooling rate has direct impacts on crystallization kinetic properties such as a metastable limit and time for crystallization. Therefore, both the amount of seed crystals and a cooling rate have key effects on product yield and purity and will be studied intensively in this chapter.

6.1 Experiments and simulations

6.1.1 Experiments

The experimental apparatus is shown in Figure 3.3. The hollow fiber membrane was used to replace a flat plate membrane in the previous chapter to increase the surface area of the membrane. Section 3.1.2.1 describes the membrane description, how the experimental set up is designed, and the procedures to set up and to clean the unit. Section 3.1.2.1 also includes the calculations of the surface area required for the process and of the solution flow rates to the hollow fiber unit. The mathematical simulations were run to plan the possible experiments. The results from mathematical simulations were compared with the experimental results. The temperature range of this experiment was from 5 – 26^{o}C but 37 – 40^{o}C for experiments with a flat plate membrane. In this experiment, the temperature range has increased from 3 to 21^{o}C as shown from the last chapter. However, the experiments in this chapter were run at a lower temperature. The reason behind this is that at higher temperature (40^{o}C), primary nucleation occurs in the

tube transporting the solution to the membrane module and inside the membrane module because the operating temperature is much higher than room temperature (25^{o}C). It is quite difficult to insulate the membrane module and transporting tubes to ensure that the solution temperature is the same in the whole system with imposed cooling ramp. Moreover, the system could not be checked if primary nucleation occurs because the membrane module and the tubes are covered with the insulation. Therefore, the process was set to be operated around the room temperature and below to avoid primary nucleation. The temperature range in this chapter is large enough to show the promise of this process.

Figure 6.1 shows the experimental grid with various operating conditions. The vertical grid shows cooling rates (^{o}C/h) and the horizontal grid shows the seed mass (g/dm^{3} crystallizer). The circles show where the experiments were performed. The number inside the circle expresses which operating condition effects that are investigated. Number 1 is the investigation of effects of seed mass on chiral separation by varying the amount of seed mass at a constant cooling rate. Number 2 is the investigation of effects of cooling rate on chiral separation by varying the cooling rates at a constant seed mass. Number 3 is the search for desirable operating condition. It will be shown in section 6.2.3 that the desirable condition corresponds to the condition in circle 3. The number of run and run time of each circle are shown in Table 6.1.

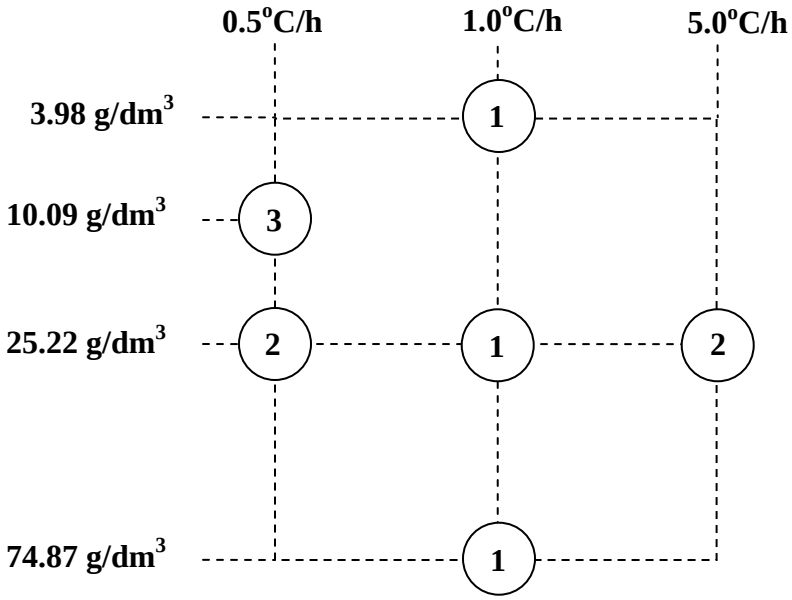

Figure 6.1: The experimental grid: vertical grid = cooling rate (°C/h), horizontal grid = seed mass (g/dm^3 crystallizer). Circles show where the experiments were performed; 1 = investigation of effects of seed mass, 2 = investigation of effects of cooling rates, and 3 = search for desirable operating condition

Table 6.1: Experimental plans

Number of runs/ Run time (h)		Cooling rate (°C/h)				
		0.2	0.5	1.0	5.0	10.0
Crystal seed mass (g/dm^3 crystallizer)	3.98	-	-	8/25	-	-
	10.09	-	4/50	-	-	-
	25.22	-	4/50	17/25*	4/5	-
	74.87	-	-	8/25	-	-

*9 runs for D-Glu seeds added to V1 and L-Glu seeds added to V2 and 8 runs for the D-Glu seeds added to V2 and L-Glu seeds added to V1.

The experimental procedures are described as follows.

1. An aqueous solution of DL-Glu was prepared by dissolving DL-Glutamic monohydrate into HPLC grade water at 35 °C with a concentration around 0.016 gram of DL-Glutamic per gram of solution. The solution was filtered through a membrane with 0.2 μm pores to remove impurities and undissolved particles.
2. A clear DL-Glu aqueous solution that had a concentration corresponding to saturation at 26°C, was cooled from 35 to 30°C. Then the solution was cooled from 30 to 5°C with different cooling rates, 0.5, 1.0, and 5.0°C/h.
3. D and L seed crystals of glutamic acid were introduced into Vessel 1 and Vessel 2, respectively, at 26°C. The amounts of the enantiomer seed crystals were 3.98, 10.09, 25.22, and 74.87 g/dm^3 crystallizer. However, there was one extra set of experiments with 14.25 g seed crystals and 1.0^{o}C/h cool rate that L-Glu seeds were introduced in V1 and D-Glu seeds in V2 to determine whether the different vessels have effects on the separation process. The starting time for a run was defined to be when the solution reached 26 °C. Solution samples were withdrawn throughout the run by using a syringe with a 0.2-μm filter and mixed with internal standard for concentration analysis. The final product crystals were filtered, dried, and weighed. They then were redissolved in water, filtered, and analyzed by HPLC as shown in section 3.2.2. Each run was repeated multiple times to determine a standard deviation that is used in the analysis of experimental results. In each set of experiment, 12 to 15 samples are collected and analyzed through HPLC. The experimental plans are described in Table 6.1. The experiments were performed in the order as shown in Figure 6.1.

4. First, the experiments were fixed with a cooling rate of 1.0°C/h but the seed crystal mass was varied as 3.98, 25.22, and 74.87 g/dm^3 crystallizer . Then, the experiments were fixed with the crystal seed mass of 14.25 g but the cooling rate was varied as 0.5, 1.0, and 5.0°C/h. Finally, the experiments were run expecting to produce the amount of product relatively close to the amount of the seed mass by introducing seed mass equal to 10.09 g/dm^3 crystallizer to the experiments with the cooling rate of 0.5°C/h.

The experiments were not carried out with cooling rates of 0.2 and 10.0°C/h. At a cooling rate of 0.2°C/h, the metastable limit gap is very small as can be seen from Figure 4.2 and therefore, it creates great difficulty for the separation. Due to very low mass transfer coefficient, k_G, the cooling rate of 10.0°C/h is not used because it does not allow sufficient time for desirable solute to crystallize and to have enough impact to transport undesirable enantiomer across the membrane. Therefore, the undesirable enantiomer concentrations remain relatively constant and hit the metastable limit. The simulations also prove that the solute concentration hits the metastable limit which is undesirable for 0.2 and 10.0°C/h. The simulation results will be discussed in the next section.

6.1.2 Simulations

The value of K_G was estimated by fitting the experimental results with seed mass equal to 3.98, 25.22, and 74.87 g/dm^3 crystallizer at 1.0°C/h. The estimation procedure followed section 5.4. The estimated K_G was used for the future predictions and explanations of a system behavior in the remains of experiments. The mathematical

equations can be found in section 2.5. The simulation results were compared with the experimental results to validate the model and to explain system behavior.

6.2 Results and discussions

6.2.1 Effects of seed mass on chiral separation

As was seen in chapter 5, the separation of DL-Glu through a flat plate membrane were successful with seed mass roughly around 3.50 and 22.20 g/dm^3 crystallizer with a cooling rate of 1.0^{o}C/h. The product purity was over 94% and the yield increased up to 37% from preferential crystallization for a short cooling range. In this chapter, the experiments were carried out for the chiral separation with a larger cooling range (26 to 5^{o}C). As shown in Figure 6.1, the experiments were carried out at a fixed cooling rate of 1.0^{o}C/h with seed mass equal to 3.98, 25.22, and 74.87 g/dm^3 crystallizer.

The simulations were carried out at the conditions above to estimate K_G for the use of future prediction. K_G was found to be 0.0025 cm/min which was the same as the K_G from Chapter 5 even though the temperature range was different (37 – 40^{o}C for Chapter 5 and 5 – 26^{o}C for this chapter). As shown in section 5.4, K_G was controlled by k_r or the surface integration step which can be expressed in an Arrhenius relationship with temperature. Because K_G did not change upon the temperature, it implied that the activation energy of the surface integration in Equation 2.10 was very low. Therefore, k_r did not change significantly upon the temperature.

Figure 6.2 shows the concentrations of D and L-Glu versus temperature for experiments with seed mass = 3.98 g/dm^3 crystallizer at a cooling rate of 1.0^{o}C/h. Figure 6.2 a) shows the average concentrations ± standard deviation versus temperature from

experiments. Figure 6.2 b) shows the simulation results. As can be seen from Figure 6.2 a), the solution concentrations decreased as the process went on as crystal growth occurred. The concentrations remained within the metastable limit zone but hit the metastable limit around 16.4^{o}C. It means the spontaneous nucleation of undesired species occured at 16.4^{o}C. After reaching the metastable limit, the solution concentration decreased with temperature along the metastable limit line. Then, the concentrations dropped drastically at around 12^{o}C. The abnormal decreasing trend could come from the following. Primary nucleation occurred and created newly formed crystals. These newly formed crystals did not have sufficient surface area so that the concentrations could drop dramatically but slightly along the metastable limit line. At 13^{o}C, the surface area of the newly formed crystals increased to be significant enough because the solute grew on top of the newly formed crystals adding more surface area. This significant surface area withdrew the solute from the solution significantly and eventually the solute concentrations dropped sharply. Figure 6.2 b) shows the simulated plot of solute concentrations versus temperature as K_G was 0.0025 cm/min. As can be seen here, the simulation results agreed well with the experiments. Therefore, the estimate value of K_G of 0.0025 cm/min was reasonable. However, the simulated solute concentrations were out of interest after the metastable limit was reached. The model was supposed to predict the behavior when the metastable limit would be reached and to explain the transport phenomena before the metastable limit is reached. The assumption can be found in 2.5. Product yield and purity will be discussed later on in this section.

Figure 6.3 shows the concentrations of D and L-Glu versus temperature for experiments with seed mass = 25.22 g/dm^3 crystallizer at a cooling rate of 1^{o}C/h. Figure

6.2 a) shows a plot of average concentrations ± standard deviation versus temperature. Figure 6.2 b) shows the simulation results. As shown in Figure 6.3 a), The concentration decreased as the process went on and remained in the metastable limit zone. It showed that spontaneous nucleation of undesired species did not occur. In this experiment, D-gltuamic acid should crystallize in V1 because D-Glu seeds were introduced in V1. In the same manner, L-Glu should crystallize in V2. As can be seen in Figure 6.3 a), D-Glu concentrations were lower than L-Glu in V1 because D-Glu crystallized in V1. In the same way, L-Glu concentrations were lower than D-Glu in V2 because L-Glu crystallized in V2. Also, the concentrations of D-Glu in V1 were lower than in V2 so that D-Glu in V2 could export to V1. The same explanation could be applied why the concentrations of L-Glu were lower in V2 than V1.

Figure 6.3 b) shows the simulated plot of solute concentrations versus temperature as K_G was 0.0025 cm/min. As can be seen from Figure 6.3 a) and b), the simulation results agreed well with the experiments. Therefore, the estimate value of K_G of 0.0025 cm/min was reasonable.

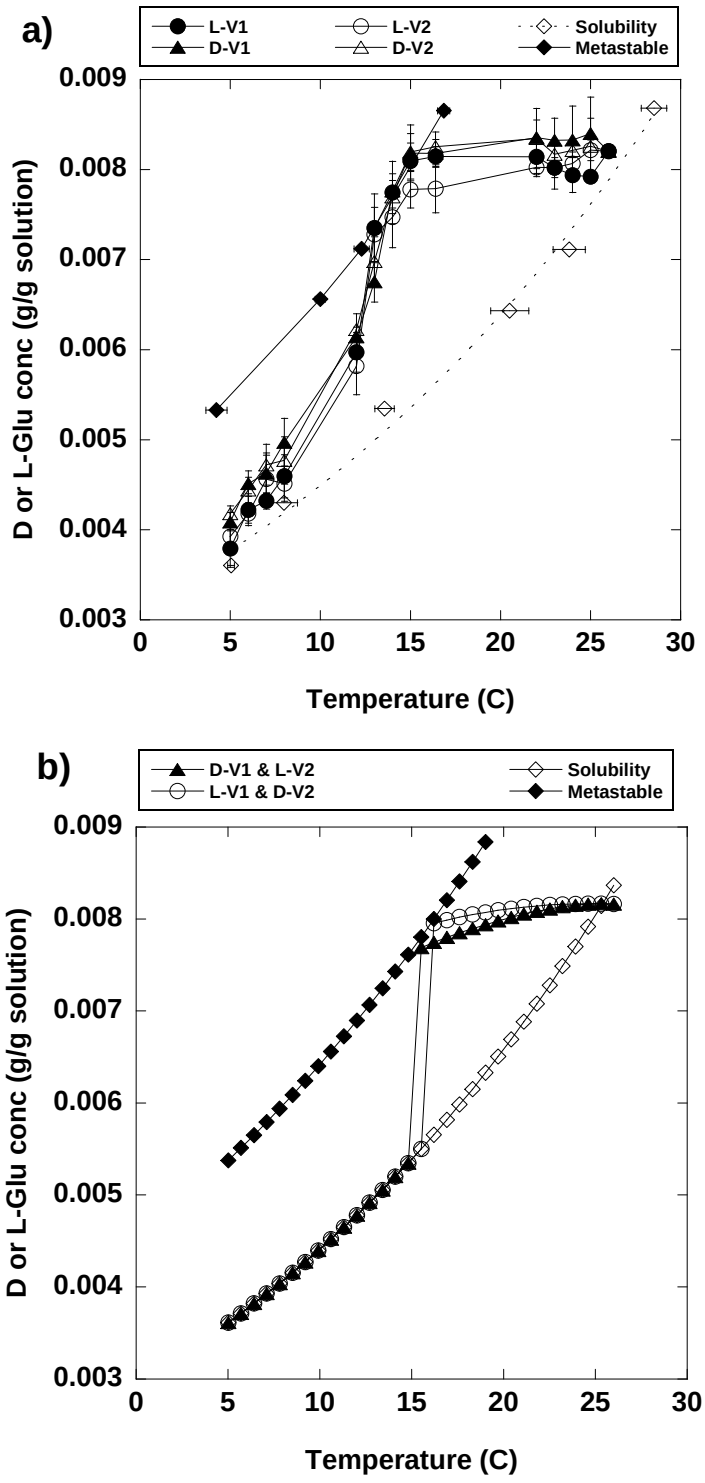

Figure 6.2: Solution concentrations of D and L-Glu versus temperature with seed mass = 3.98 g/dm^3 crystallizer at cooling rate of 1.0^{o}C/h. a) experimental results and b) simulated results. D-Glu seeds were added to V1 and L-Glu seeds were added to V2.

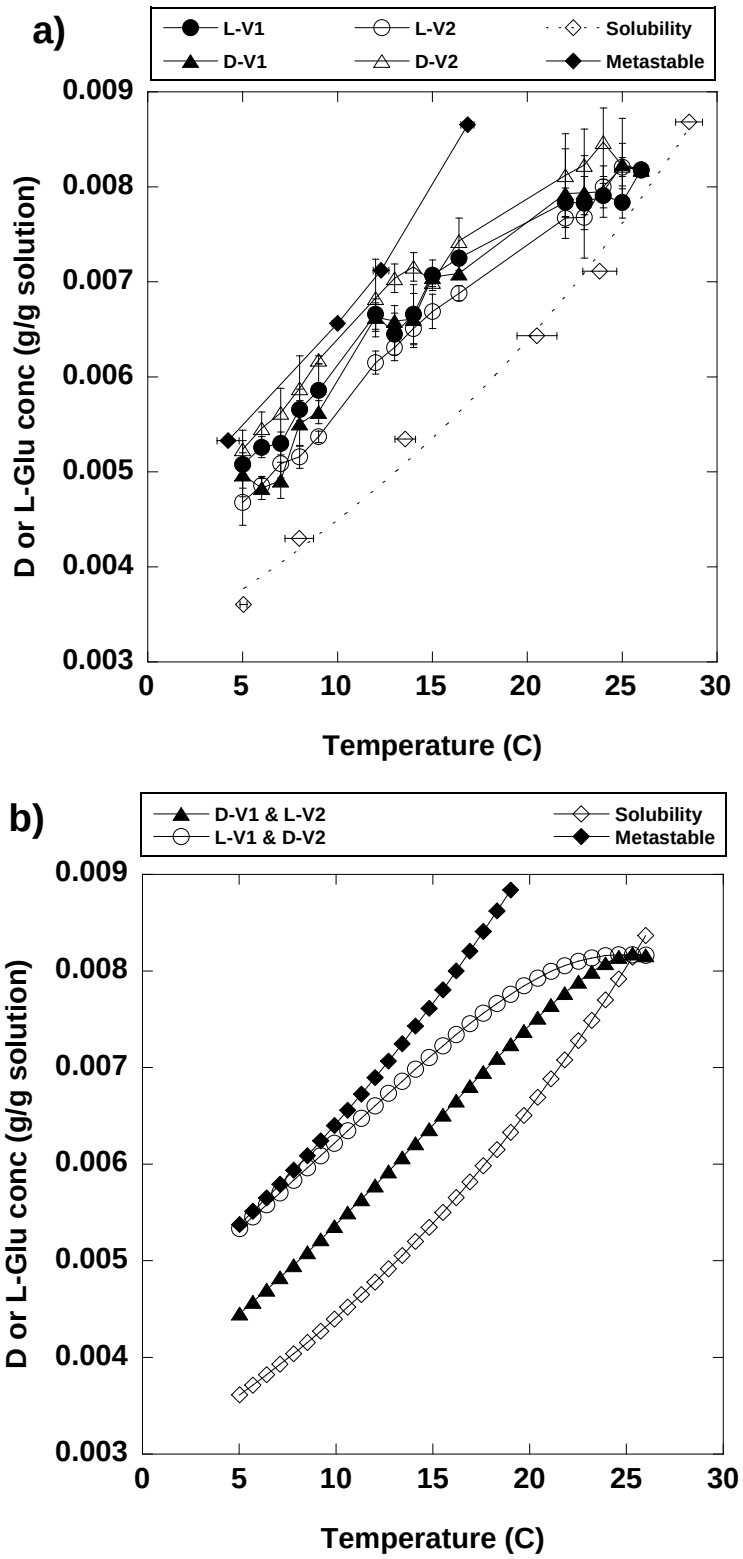

Figure 6.3: Solution concentrations of D and L-Glu versus temperature with seed mass = 25.22 g/dm^3 crystallizer at cooling rate of 1.0^{o}C/h. a) experimental results and b) simulated results. D-Glu seeds were added to V1 and L-Glu seeds were added to V2.

The interesting observation is that the gap between D and L-Glu concentrations in V1 was noticeably smaller than the gap in V2. The concentrations from lowest to highest are L-Glu in V2, D-Glu in V1, L-Glu in V1, and D-Glu in V2. The source of this unexpected behavior could come from the design of the operation. As shown in section 3.1.2, the solutions were pumped through the membrane module at different flow rates so that there was no convective mass transfer across the membrane. The solution from V1 was pumped to the shell side at the rate of 98 cm^3/min while the solution from V2 was pumped to the tube side at 17 cm^3/min. Therefore, there was a thicker cake layer of crystals coated on top of the inlet filter in V1. The thicker cake layer in V1 allowed less crystals to suspend in the vessel. It means that the surface area for crystallization in V1 was less than V2 and therefore, D-Glu in V1 did not crystallize as fast as L-Glu in V2 did. Because D-Glu concentration in V1 did not decrease as fast, the driving force from the concentration difference of D-Glu in both vessels was lower than the driving force of L-Glu. This makes the concentrations of D-Glu in V2 the highest and L-Glu in V1 the lowest.

The assumption for the unexpected behavior above is that the thicker cake on the inlet filter allowed less seed crystals available for crystallization in V1 and this behavior did not come from the difference in crystallization kinetics of D and L-Glu. To prove that this assumption is valid, seed crystals were switched to be introduced into the different vessels; D-Glu were instead introduced to V2 and L-Glu were introduced to V1. Figure 6.4 a) shows the plot of average concentrations ± standard deviation versus temperature. Figure 6.4 a) shows similarity of Figure 6.3 a) in a reverse manner. By that, the magnitude of concentrations from highest to lowest is L-Glu in V2, D-Glu in V1, L-

Glu in V1, and D-Glu in V2 respectively. The concentration plots shows that the concentrations of crystallizing species in V1 (L-Glu) were higher than the concentrations of crystallizing species in V2 (D-Glu). This behavior depends upon which vessel the crystallizing species is in not what enantiomer the crystallizing species is. In conclusion, the unexpected behavior comes from the operational set up not that D and L-Glu crystallize differently.

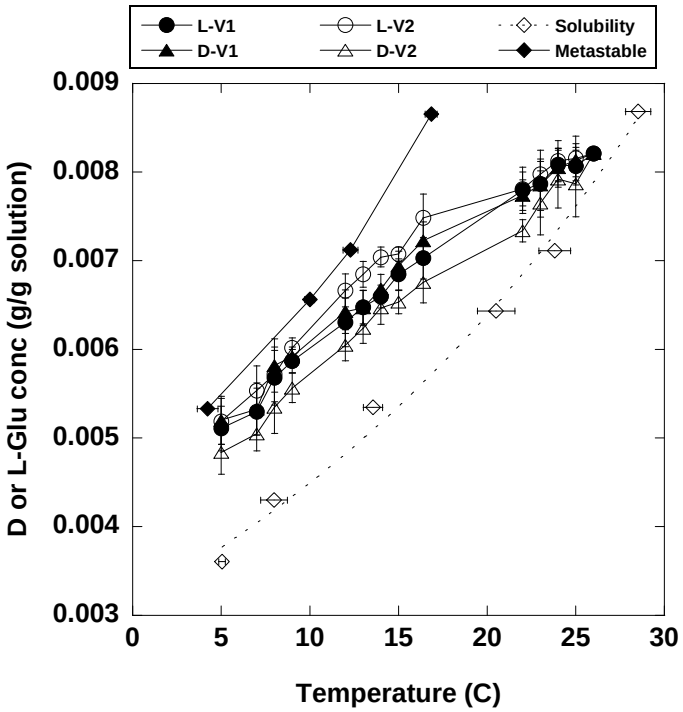

Figure 6.4: Solution concentrations of D and L-Glu versus temperature with seed mass = 25.22 g/dm^3 crystallizer at cooling rate of 1.0^{o}C/h. L-Glu seeds were added to V1 and D-Glu seeds were added to V2.

At this point, the separations were successful with a condition using 25.22 g seed crystals /dm^3 crystallizer seed crystals with a cooling rate 1^{o}C/h. Next, the seed mass was increased to 74.87 g/dm^3 crystallizer. In these experiments, D-Glu seeds were introduced

in V1 and L-Glutamic seeds were introduced in V2. Figure 6.5 a) shows a plot of average concentrations ± standard deviation versus temperature. As shown in Figure 6.5 a), the solute concentrations decreased as the run progress as desirable crystals grew. The concentrations did not reach the metastable limit which is desirable. The concentrations of D-Glu were lower than L-Glu in V1 and L-Glu concentrations were lower than D-Glu in V2. The explanation of the behavior in Figure 6.3 a) could be applied here. However, the concentrations in Figure 6.5 a) were much closer to the solubility limit. This could come from the crystallization rate that was faster as the crystal surface area increased from increasing seed mass. Therefore, the concentrations of the crystallizing materials dropped close to the solubility. Interestingly, the concentrations of non-crystallizing species were slightly higher than ones from crystallizing species. It could come from the sufficient membrane surface area facilitating the mass transport across the membrane. The non-crystallizing species could transport across the membrane quicker resulting in their concentrations getting closer to the crystallizing species. Figure 6.5 b) shows the concentration profile from mathematical simulations by using K_G equal to 0.0025 cm/min. As can be seen from Figure 6.5 b), the mathematical simulations generated reasonable concentration profiles. It means that K_G equal to 0.0025 cm/min was reasonable. However, the simulated concentrations were slightly higher than experimental results. These higher predictions could come from the fact that the model assumes that the seed mass is spherical with one size at 600 μm which is the upper bound of the crystal size. This assumption makes the crystal surface available for the model much less than the surface available in the experiments. Therefore, the concentrations in the experiments were lower than the ones in the simulations.

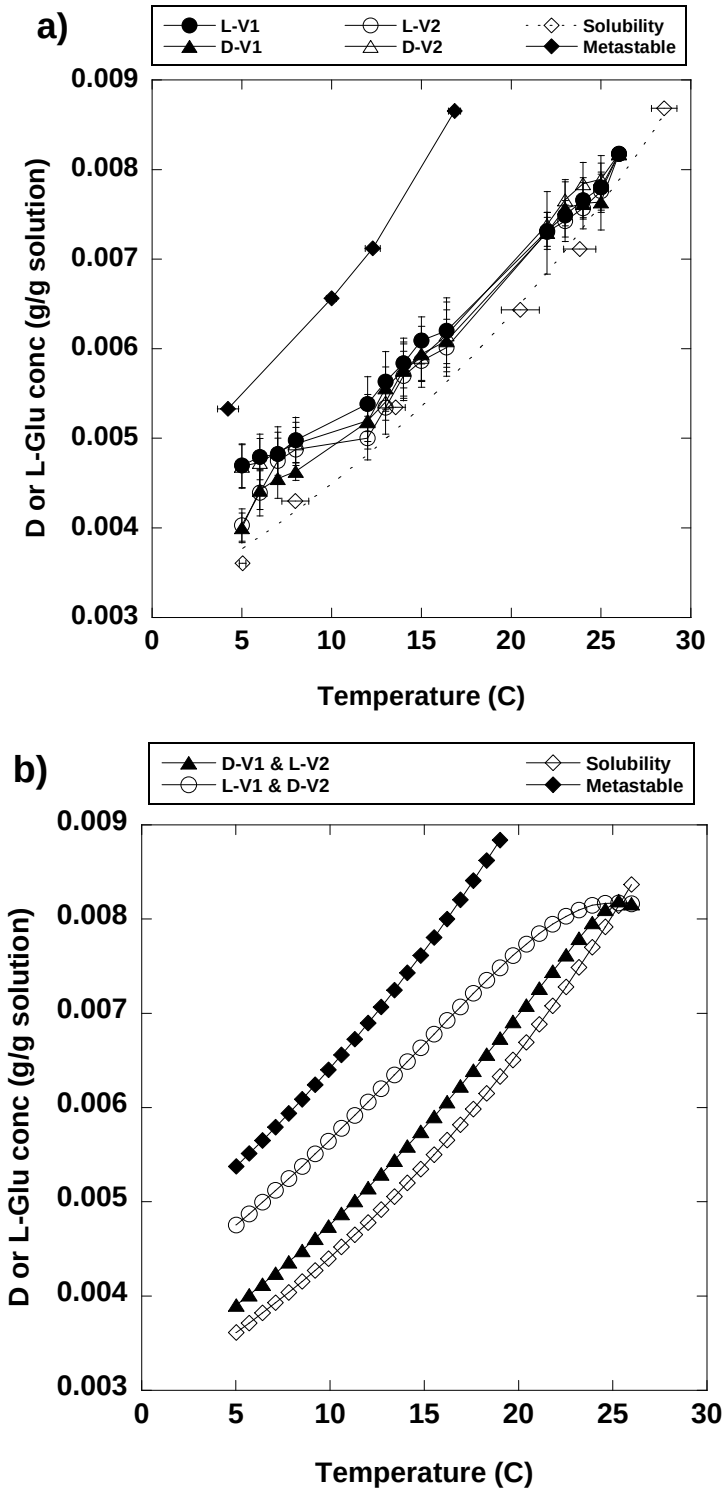

Figure 6.5: Solution concentrations of D and L-Glu versus temperature with seed mass = 74.87 g/dm^3 crystallizer at cooling rate of 1.0^{o}C/h. a) experimental results and b) simulated results. D-Glu seeds were added to V1 and L-Glutamic seeds were added to V2.

After investigating the concentration profile, the product yield and purity are considered next. Table 6.2 summarizes the product yield and purity, the expected yield from HPLC calculations and simulations, product mass per maximum possible product, product mass per seed mass, the calculated product yield from preferential crystallization, and the yield enhancement for the experiments with a constant cooling rate of 1.0^{o}C/h with various seed mass, 3.98, 25.22, and 74.87 g/dm^3 crystallizer. The first line is the total product mass recovered excluding the seed mass. It was measured by the weighing the dried crystal mass recovered deducted by the mass of the seed crystals. The second line shows the product purity analyzed by the HPLC. The third line shows the calculated product mass recovered according to the equation below.

$$M_i = m_{sol,V1}(w_{i,initial,V1} - w_{i,final,V1}) + m_{sol,V2}(w_{i,initial,V2} - w_{i,final,V2}) \qquad \text{Equation 6.1}$$

Where M_i = product mass of species i (g), $m_{sol,V1}$= mass of solution 1 (g), $m_{sol,V2}$= mass of solution 2 (g), $w_{i,initial}$ = weight fraction of species i at the beginning, $w_{i,final}$ = weight fraction of species i at the end. Equation 6.1 works for the system in which primary nucleation does not occur. Basically, the product mass i equals to the summation of product i came from both V1 and V2. This mass calculation from HPLC is a good estimation for how much the product should be from the value measured from the experiments. The fourth line shows the simulated mass expected from each vessel and the equations were shown in section 2.5. Again, this is applicable for only the system without primary nucleation. The nucleation rate was not estimated here. The fifth line is the calculated mass of the product from the preferential crystallization. Assuming that the membrane is non-permeable, the change of desired enantiomer concentration in the vessel comes from solely preferential crystallization and the undesired enantiomer

concentrations would remain the same. The process ends when the undesired enantiomer concentration exceeds the metastable limit. At 16.4°C, the original solute concentration was equal to the metastable limit concentration. The mass of desired product from preferential crystallization is equal to the solution mass times the difference of weight fraction from the beginning and the end, 16.4°C. The equation is shown below.

$$M_i = m_{solution,Vj}(w_{i,initial} - w_{i,T'}) \quad \text{if } i\text{=D-Glu, } Vj = V1 \text{ and if } i\text{=L-Glu, } Vj = V2$$

Equation 6.2

Where $w_{i,T'}$ = weight fraction of species i at the temperature that undesired enantiomer reaches metastable limit.

The recovered product mass was also compared to the maximum possible product mass to consider how much the available product was recovered. The maximum possible product mass could be calculated through Equation 5.3.

$$M_{i,\max} = (m_{sol,V1} + m_{sol,V2})(w_{i,initial} - w^*_{i,final}) \qquad \text{Equation 5.3}$$

For all of these experiments, $M_{i,\max}$ was equal to 9.24 g/dm^3 crystallizer. The ratio of the recovered product mass to the maximum possible product mass was shown in Table 6.2. The ratio of the product mass to the seed mass was also presented here. The key feature of this process was the yield enhancement of the hybrid process from the preferential crystallization alone. The yield enhancement is calculated as below.

$$\textbf{\textit{Yield enhancement}} = \frac{(M_{i,final} - M_{i,crystallization})}{M_{i,crystallization}} x100 \qquad \text{Equation 6.3}$$

Table 6.2: Summary of product yield and purity from the experiments with various seed masses and a constant cooling rate of 1.0°C/h

	Seed mass (g/dm^3 crystallizer)					
	3.98		25.22		74.87	
	V1	V2	V1	V2	V1	V2
Total product mass recovered* (g/dm^3 crystallizer)	8.19 ± 0.60	8.11 ± 0.62	5.52 ± 0.32	6.14 ± 0.41	7.12 ± 0.28	7.36 ± 0.50
Percent product purity analyzed by HPLC	53.44%	54.31%	>99.7%	>99.7%	>99.7%	>99.7%
Product mass expected from HPLC calculation (g/dm^3 crystallizer)	N/A	N/A	6.16	6.62	7.68	7.65
Product mass expected from simulation (g/dm^3 crystallizer)	N/A	N/A	6.62	6.62	7.77	7.77
Product mass / maximum possible product mass	N/A	N/A	0.60	0.66	0.77	0.79
Product mass / seed mass	N/A	N/A	0.22	0.24	0.10	0.10
Product mass from solely preferential crystallization (g/dm^3 crystallizer)	N/A	N/A	1.10	1.31	2.14	2.21
Yield enhancement from preferential crystallization	N/A	N/A	404%	371%	234%	233%

* Average ± a standard deviation

Table 6.2 shows that experiments with 3.98 g seed mass /dm^3 crystallizer showed almost no selectivity in both V1 and V2 since the desired product was a little over 50% of the final product. As can be seen from Figure 6.2 a), both desired and undesired enantiomer concentrations exceeded the metastable limit and primary nucleation occurred. Primary nucleation created a significant number of infinitesimal crystals generating enormous surface area for crystal growth. The growth on infinitesimal crystals was much more significant than the growth on seed crystals because of the much larger surface area. Therefore, the product of this experiment contained almost equal amounts of each enantiomer.

As can be seen in Table 6.2, the separation by experiments with 3.98 g seed mass /dm^3 crystallizer failed due to the insufficient surface area of seed crystals. As the seed mass increased to 25.22 to 74.87 g/dm^3 crystallizer, the separation turned out to be successful. HPLC analysis shows that the product purity was over 99.7%. Please note that with the column used, HPLC cannot detect the impurity less than 0.3%. The HPLC shows only one peak for the purity analysis for the experiments with seed mass equal to 25.22 to 74.87 g/dm^3 crystallizer. This product purity could be 99.7 – 100%. Figure 6.2 a) and Figure 6.5 a) show that the metastable limit was not exceeded and the undesired enantiomer did not crystallize. However, the impurity could come from the racemic solution that remained on the crystal surface during filtration. It is impossible to get rid of all excess racemic solution. According to Mullin (2001 page 297), often the bulk-produced organic chemical is considered "pure" as the purity >95%. Some specialty chemical considers >99% as "pure." If the purity is over 99.9%, it is called ultra pure. It is nearly impossible to produce 100% product for several operating conditions. For

example, the mother liquid could remain on the crystal after filtration. Therefore, the product purity in this work could be considered pure.

The product purity is not the concern for the experiments with seed mass equal to 25.22 and 74.87 g/dm^3 crystallizer as the product purity is over 99.7%. The product yield is considered next. As the seed mass increased from 25.22 to 74.87 g/dm^3 crystallizer, the product mass increased from averagely 5.82 to 7.24 g/dm^3 crystallizer. It is logical because of the increase of surface area available for crystallization. However, the increase of seed mass did not increase the product mass proportionally. The increase of the seed mass is 1.97 times from 25.22 to 74.87 g/dm^3 crystallizer but the increase of product mass is only 0.24 times from 5.82 to 7.24 g/dm^3 crystallizer. This is due to crystallization kinetics. As shown from Equation 3.30 to 3.35, the amount of mass crystallizes depends on the seed crystal surface for crystallization and the driving force which is the concentration difference between the solution and the solubility. As the seed mass increases, the solute molecules crystallize more at the beginning since the seed crystal surface area increases. Then, the solute concentrations drop lower than the experiments with 25.22 g seed crystals/dm^3 crystallizer. Hence, the driving force decreases because it is the difference between concentrations in the solution and the solubility. This behavior could be observed from Figure 6.3 a) and Figure 6.5 a). These figures show the experimental results that the concentrations of crystallizing species from 74.87 g seed crystals /dm^3 crystallizer were lower than the ones from 25.22 g seed crystals /dm^3 crystallizer. In conclusion, the increase of seed mass is both productive and counter productive on crystallization. However, the overall process is still productive to increase the seed crystal as it increased the product mass.

As shown that the increase of seed mass did not increase the product mass proportionally, it seems that it is not a good investment to increase the seed mass from 25.22 to 74.87 g/dm^3 crystallizer. On average, the product mass to seed mass ratio dropped from 0.23 to 0.10 when the seed mass increased from 25.22 to 74.87 g/dm^3 crystallizer. This problem will be considered later on in this chapter. Product mass collected from V2 was higher than V1 because there was less crystal surface available in V1 as discussed earlier in this section.

The ratio of the recovered product to the maximum possible product mass approximately increased from 63% to 78% from when the seed mass increased from 25.22 to 74.87 g/dm^3 crystallizer. The possible product in one vessel would be a half of the maximum possible product. In general, the maximum possible product was quite hard to achieve because the equilibrium must be reached on both sides of the membrane. Therefore, the recovered product was more than a half of the possible product available in one vessel showing big improvement from preferential crystallization alone.

As was seen in Table 6.2, the values of total mass from experiments were little less than mass calculated from HPLC analysis and from the model. It means that the HPLC analysis and the model were reasonable. The less mass weight in the experiments could come from some mass loss during the crystal collection at the end of the process.

The calculated product mass from preferential crystallization from the experiments with 25.22 g seed crystals/dm^3 crystallizer seed mass was lower than the one with 74.87 g seed crystals/dm^3 crystallizer. Increasing seed mass from 25.22 to 74.87 g/dm^3 crystallizer increases surface available for crystallization. Therefore, the crystallizing species concentrations reduced lower with 74.87 g seed crystals /dm^3

crystallizer resulting in a larger generation of product mass from preferential crystallization according to Equation 6.1. As shown in Table 6.2, there is an improvement in product yield from process from the integrated process with hollow fiber membranes compared with solely preferential crystallization for the experiments. The yield enhancement was between 371 – 404% and 233 – 234% for the experiments with seed mass equal to 25.22 and 74.87 g/dm^3 crystallizer respectively. The yield enhancement from experiments with 25.22 g seed crystals /dm^3 crystallizer seed mass was higher than from 74.87 g seed crystals /dm^3 crystallizer because the denominator in Equation 6.3 was smaller. The improvement is significant and it proves that this process is revolutionary. The effect of the cooling rate on product yield and purity will be studied next to determine the best operating conditions for the separation.

For the model, K_G = 0.0025 cm/min was appropriate as it fitted the simulated data to experimental data well. Therefore, K_G = 0.0025 cm/min was used for the prediction for the rest of the chapter.

6.2.2 Effects of cooling rate on chiral separation

As can be seen from the previous section, the experiments showed that the novel process is successful in separating DL-Glu by holding a constant cooling rate but various seed mass. The major improvement was received from the experiments with 25.22 g seed crystals/dm^3 crystallizer as it produced pure product and yield enhancement was up to 404% from preferential crystallization. The study of cooling rates was studied in this section. Constant seed mass of 25.22 g/dm^3 crystallizer was used to study the effect of cooling rates on product purity and yield. The higher seed mass of 74.87 g/dm^3

crystallizer was not used because it increased the product yield very little while the seed mass was increased much more. In the pharmaceutical industries, the amount of seed mass introduced was roughly at least equal to the amount of product expected. The seed mass at 74.87 g/dm^3 crystallizer produced only 7.24 g product crystals/dm^3 crystallizer and that product mass was less than 10% of the seed mass. The search for the appropriate seed mass will be studied in the next section. The simulations were carried out to predict the experiments and to explain system behavior. The estimated value of K_G was 0.0025 cm/min from section 6.2.1.

The experiments were carried out with 25.22 g/dm^3 crystallizer seed mass with cooling rates of 0.5 and 5.0^{o}C/h. Figure 6.6 a) shows a plot of average concentrations ± standard deviation versus temperature from experiments with a cooling rate of 0.5^{o}C/h. As shown in Figure 6.6 a), the solution concentrations decreased as the process went on and remained within the metastable limit zone. It shows that the primary nucleation of undesired species did not occur. The solute concentrations were lower than experiments with cooling rate of 1^{o}C/h as the solute molecules were allowed to have a longer time to grow on the crystal surface at a cooling rate of 0.5^{o}C/h. Therefore, the solutes were drawn out of the solution more and the concentrations were lower with a cooling rate of 0.5^{o}C/h. Figure 6.6 b) shows the plot of concentrations versus temperature from the model. It can be seen that Figure 6.6 b) from the model agrees well with Figure 6.6 a) from the experiments.

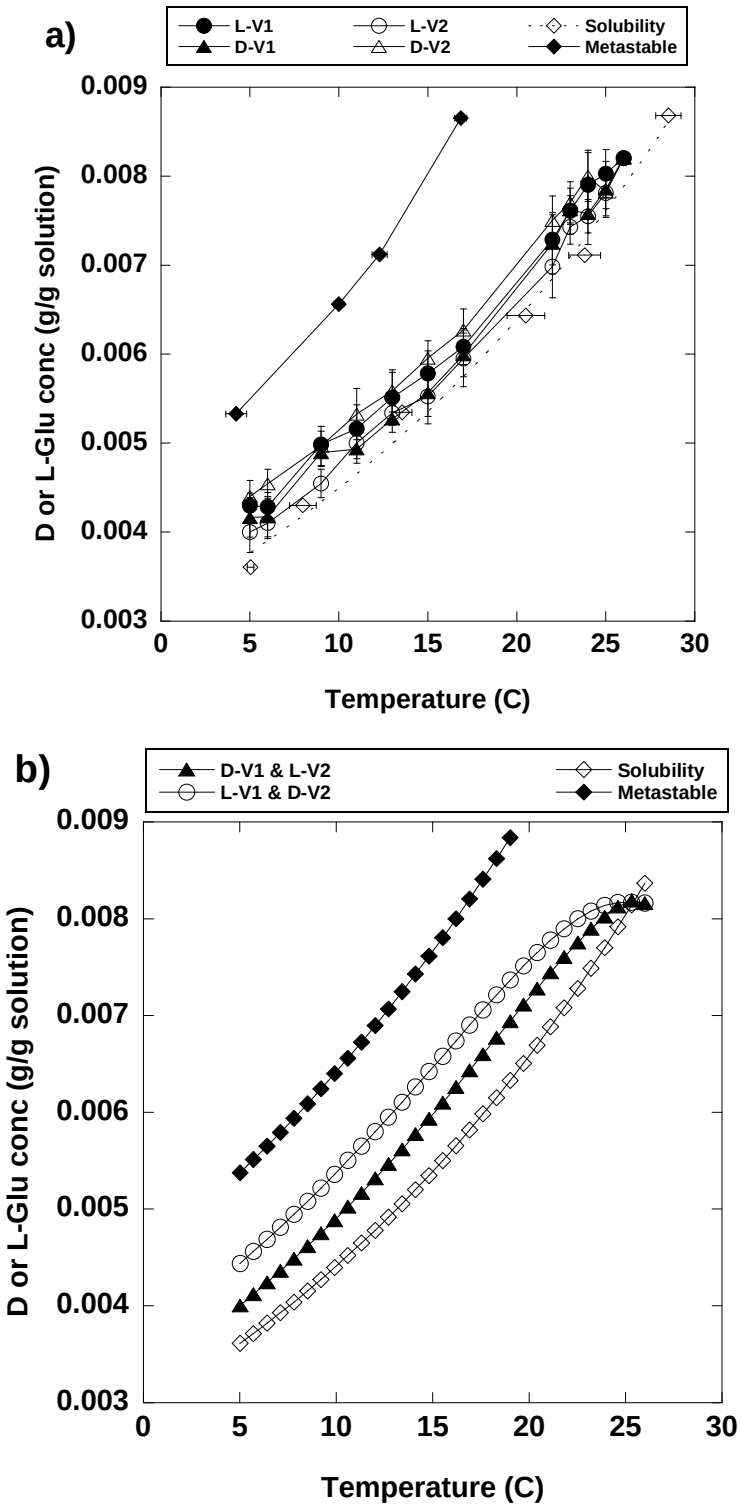

Figure 6.6: Solution concentrations of D and L-Glu versus temperature with seed mass = 25.22 g/dm^3 crystallizer at cooling rate of 0.5^{o}C/h. a) experimental results and b) simulated results. D-Glu seeds were added to V1 and L-Glutamic seeds were added to V2.

As the cooling rate of 0.5^{o}C/h was successful, the cooling rate for the experiments increased to 5^{o}C/h to determine if the process could be faster and as productive. Figure 6.7 a) shows a plot of average concentrations ± standard deviation versus temperature from the experiments with 5.0^{o}C/h cooling rate. Figure 6.7 a) shows that the concentrations changed slightly as the process went on. It could come from the fact that the time for crystal growth was too little to draw the concentrations down as the cooling rate was as fast as 5^{o}C/h. The undesired enantiomer concentrations (L-Glu in V1 and D-Glu in V2) reached metastable limit around 12.5^{o}C while the desired enantiomer concentrations (D-Glu in V1 and L-Glu in V2) reached the metastable limit around 10^{o}C. Once the undesired enantiomer concentrations hit the metastable limit, some of desired enantiomers still grew on the seed mass and the concentrations kept decreasing. Therefore, desired enantiomers reached the metastable limit later. As can be seen from Figure 6.7 a), the concentrations did not drop instantaneously after hitting the metastable limit. The concentrations decreased along the metastable limit line for a while. Then, the concentrations of undesired enantiomer dropped sharply. The concentrations of desired species could not drop sharply because the process ended before the surface area of desired species newly formed crystals became significant enough to draw the concentrations down dramatically. This behavior is similar to the concentration change in the experiments with 3.98 g seed crystals/dm^3 crystallizer with 1^{o}C/h cooling rate as shown in Figure 6.2 a). The detail explanation about this behavior could be found in previous section in the part of experiments with 3.98 g seed crystals/dm^3 crystallizer with 1.0^{o}C/h cooling rate. Figure 6-7 b) shows the simulation results of concentrations versus temperature. The simulations results agreed well with the experimental results.

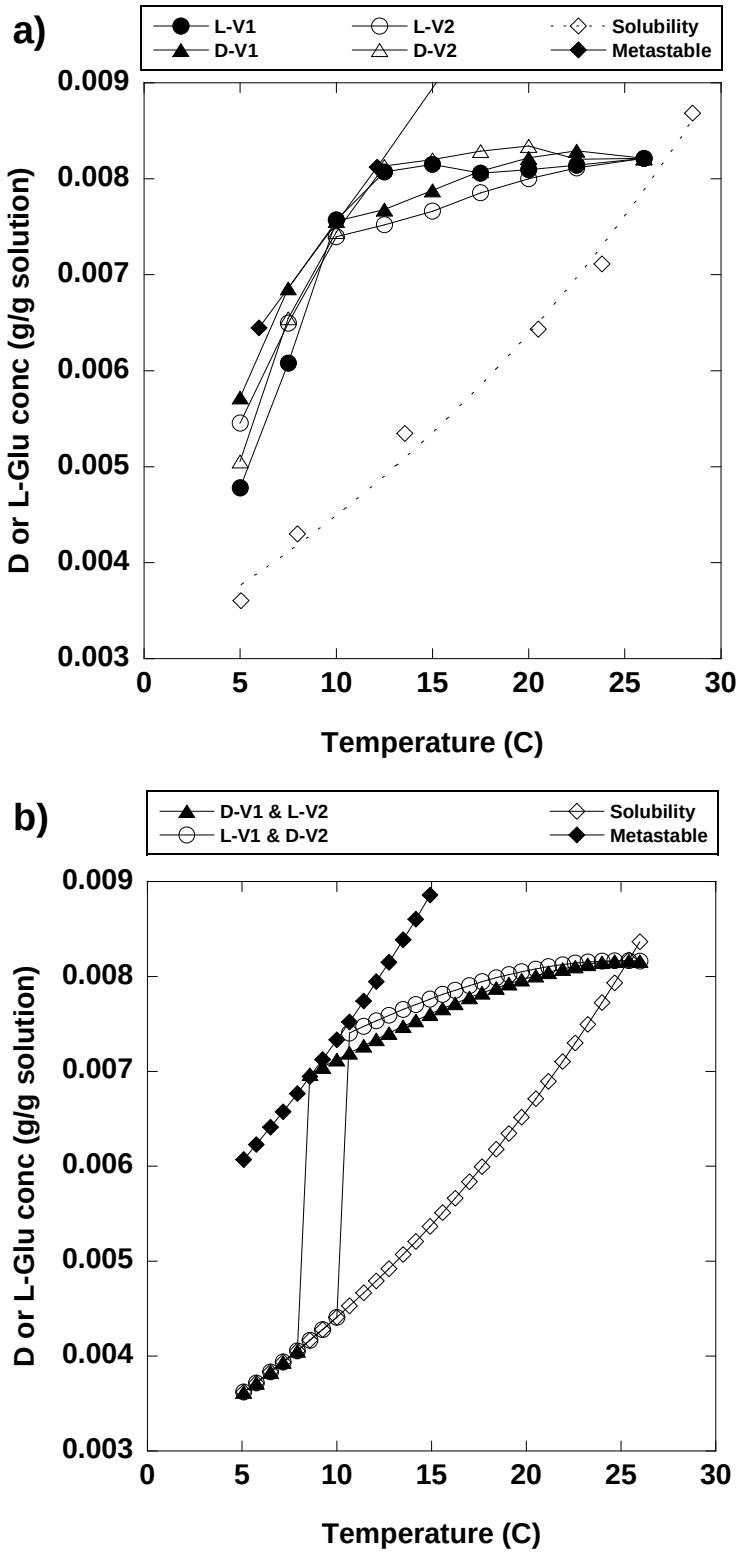

Figure 6.7: Solution concentrations of D and L-Glu versus temperature with seed mass = 25.22 g/dm^3 crystallizer at cooling rate of 5.0^{o}C/h. a) experimental results and b) simulated results. D-Glu seeds were added to V1 and L-Glutamic seeds were added to V2

Table 6.3: Summary of product yield and purity from the experiments with various cooling rates and a constant seed mass of 25.22 g/dm^3 crystallizer

	Cooling rate 0.5^{o}C/h		Cooling rate 1.0^{o}C/h		Cooling rate 5.0^{o}C/h	
	V1	V2	V1	V2	V1	V2
Total product mass recovered* (g/dm^3 crystallizer)	7.68 ± 0.24	7.91 ± 0.50	5.52 ± 0.32	6.14 ± 0.40	5.49 ± 0.34	6.21 ± 0.44
Percent product purity analyzed by HPLC	>99.7%	>99.7%	>99.7%	>99.7%	41.66%	44.67%
Product mass expected from HPLC calculation (g/dm^3 crystallizer)	8.12	7.84	6.16	6.62	N/A	N/A
Product mass expected from simulation (g/dm^3 crystallizer)	7.96	7.96	6.62	6.62	N/A	N/A
Product mass / maximum possible product mass	0.83	0.86	0.60	0.66	N/A	N/A
Product mass from solely preferential crystallization (g/dm^3 crystallizer)	2.64	2.69	1.10	1.31	N/A	N/A
Yield enhancement from preferential crystallization	191%	195%	404%	371%	N/A	N/A

* Average ± a standard deviation

After understanding the concentration profile of the process, the product yield and purity are studied next. Table 6.3 shows the summary of the product yield and purity, the expected yield from HPLC calculations and simulations, product mass per maximum possible product, the calculated product yield from preferential crystallization, and the yield enhancement for the experiments with cooling rates of 0.5, 1.0, 5.0^{o}C/h and a constant seed mass of 25.22 g/dm^{3} crystallizer. Only the experiments with 5.0^{o}C/h cooling rate failed to generate pure product. As shown in Figure 6.7 a) the solute concentrations reached metastable limit for the experiments with 5.0^{o}C/h cooling rate. Figure 6.7 a) shows that the undesired enantiomer reached the metastable limit before the desired enantiomer did. Hence, the concentrations of the undesired enantiomer dropped lower than the desired enantiomer. Therefore, the product purity was even lower than 50%.

Table 6.3 also shows some of successful experimental results. The experiments with cooling rates of 0.5 and 1.0^{o}C/h generated the product with the purity over 99.7%. The product masses measured from the experiments were reasonably close to the product masses calculated from HPLC and the model. Therefore, the model agreed well with the experiments. The product masses from 0.5^{o}C/h were higher than the ones from 1^{o}C/h. This could come from the experiments with 0.5^{o}C/h which allowed a longer time for crystal growth than the ones from 1.0^{o}C/h. Again, the product masses from V2 were observed to be higher than V1. As explained earlier, there were more crystals available in V2 due to the less cake on top of the filter situation. Therefore, the product masses from V2 were higher than V1.

Table 6.3 shows that on average, the ratio of the product mass to the maximum possible product mass increased from 63% to 85% when the cooling rate decreased from 1.0 to 0.5^{o}C/h. The increase of the ratio was considered large.

Table 6.3 shows that the calculated masses from solely preferential crystallization from the experiments with cooling rate of 0.5^{o}C/h were higher than the experiments with cooling rate of 1.0^{o}C/h. It is logical because the experiments with 0.5^{o}C/h allowed a longer time for crystal growth and therefore, the concentrations dropped sharper. This makes the denominator larger in Equation 6.3, $\frac{(m_{i,final} - m_{i,crystallization})}{m_{i,crystallization}} x100$, and results in lower yield enhancement for 0.5^{o}C/h cooling rate than to 1^{o}C/h cooling rate. Table 6.3 shows that the yield enhancement of 0.5^{o}C/h was averagely 193% which was still a leap improvement.

Table 6.3 concludes that the experiments were successful separating DL-Glu with a cooling rate of 0.5 and 1.0^{o}C/h but failed for the runs with 5.0^{o}C/h cooling rate. The simulations were carried out further at cooling rates of 0.2 and 10.0^{o}C/h to investigate the separation performance with seed mass equal to 25.22 g/dm^{3} crystallizer. Figure 6.8 a) and b) show the simulated solute concentration versus temperature with cooling rates of 0.2 and 10^{o}C/h respectively. Figure 6.8 a) shows that the concentration reached the metastable limit very early at 21^{o}C for the simulations with cooling rates of 0.2^{o}C/h because the metastable zone width was very small. On the other hand, Figure 6.8 b) shows that the concentrations reached the metastable limit much later at 8^{o}C for the simulations with cooling rate of 10.0^{o}C/h because the metastable zone width was larger. The metastable limit was still reached even though the metastable gap was larger for the simulations with 10.0^{o}C/h cooling rate. This is because the overall growth rate

coefficient was very small, 0.0025 cm/min. The fast cooling simulations did not allow enough time for the desired enantiomer to grow on seed crystals and it created a lower driving force for the undesired enantiomer to transport across the membrane. Then, the metastable limit was reached. For example, the time was not sufficient for D-Glu to grow on top of D-Glu seed crystals in V1. Then, the concentrations of D-Glu in V1 did not decrease as low as it should be and resulting in the smaller concentration difference between D-Glu in V1 and V2. D-Glu concentrations in V2 could not transport across the membrane to V1 quickly enough to avoid reaching metastable limit. As a result, D-Glu concentrations in V2, which is undesirable, exceeded the metastable limit and the process ends. In conclusion, the experiments should not be investigated further for the cooling rates lower than 0.5^{o}C/h and higher than 5.0^{o}C/h because the experiments will fail to separate DL-Glu as the simulations suggested.

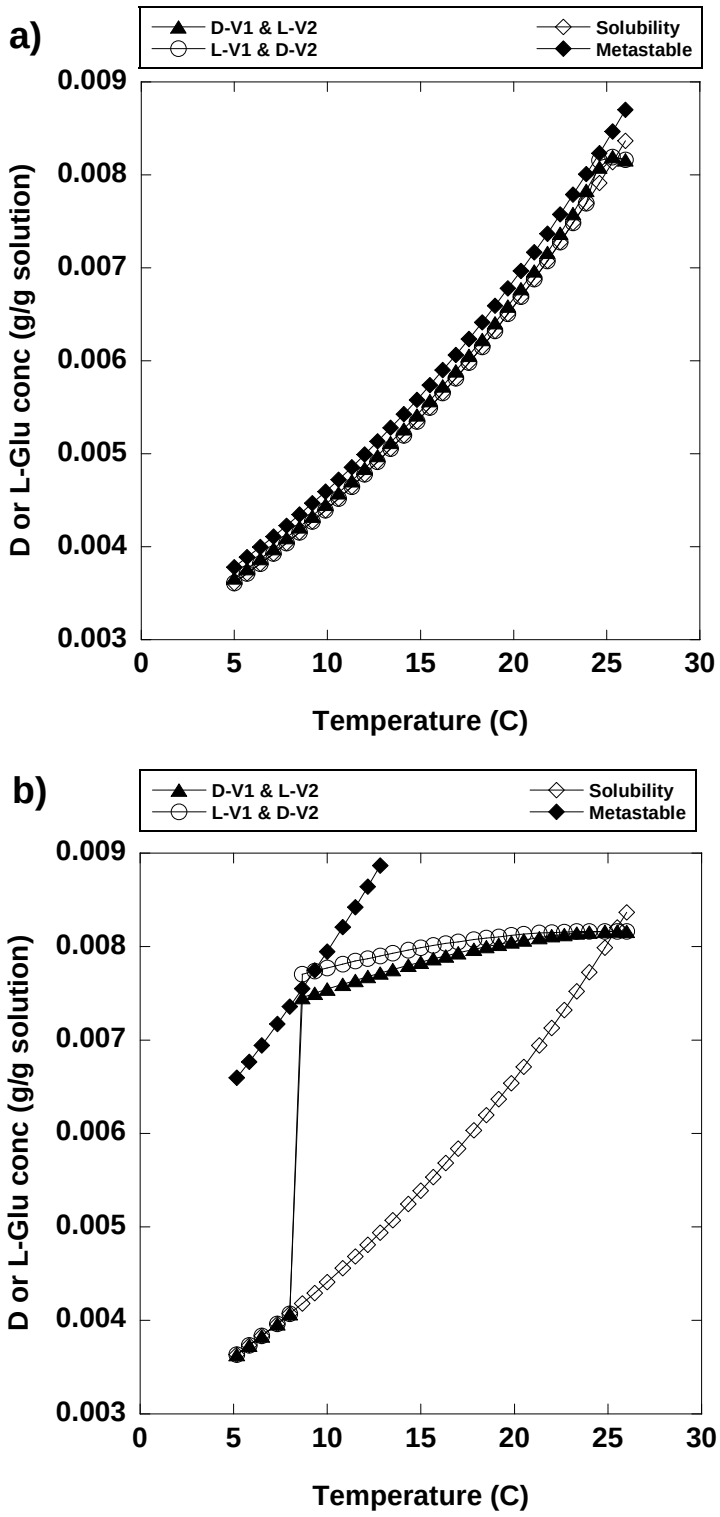

Figure 6.8: Simulated concentrations of D and L-Glu versus temperature with seed mass = 25.22 g/dm^3 crystallizer at cooling rate of a) 0.2^{o}C/h and b) 10.0^{o}C/h. D-Glu seeds were added to V1 and L-Glutamic seeds were added to V2

6.2.3 Desirable operating conditions

In this section, the desirable operating condition would be searched. The desirable operating condition gives high purity product and high product yield. The product yield should be close to the maximum possible product yield and close to the amount of seed mass. As stated earlier, it is not wise to invest a large amount of seed mass to obtain a small amount of product in return. It is quite difficult to prepare seed crystals. Seed crystals must be pure, in the right size range, and the right polymorphic form. It takes several long processes to prepare seed crystals as shown in section 3.2.3. Therefore, it is wise to use the least amount of seed crystals and obtain nearly maximum yield. In this section, the process simulations were carried out to find such conditions by varying the amount of seed crystals and cooling rates. Then the experiments were conducted to prove if the simulations were correct.

The simulations were carried out with seed mass in the range of 3.98 – 177 g/dm^3 crystallizer and with the cooling rates of 0.2, 0.5, 1.0, 5.0, and 10.0^oC/h. The amount of seed mass used was limited to 177 g/dm^3 crystallizer because the solution will turn out to be thick slurry and the crystallizer cannot hold the increased volume if the seed mass is larger than 177 g/dm^3 crystallizer. The metastable limit concentrations used in the model were constructed from experimental results in section 4.2 through mathematical regression. The simulated results shown are only the simulations that metastable limits were not reached.

According to the simulation results, the metastable limits were reached for the process with the cooling rates of 0.2, 5.0, and 10.0^oC/h. Therefore, the simulation results with these cooling rates are not shown here. The simulations with the seed mass lower

than 7.43 g/dm^3 crystallizer are also not presented as the metastable limits were also reached.

Figure 6.9 a) shows the simulated results of product crystal mass versus seed crystal mass with a cooling rate of 0.5 and 1.0^{o}C/h. Figure 6.9 a), shows that as seed mass increased, the product mass increased. This could come from the product mass increase as crystallizing surface area increased in larger amount of seed mass. The product masses were higher from the simulations with 0.5^{o}C/h than 1.0^{o}C/h. This is because the simulations with 0.5^{o}C/h cooling rate provided more time for crystallization and eventually result in producing a higher product mass. Figure 6.9 a) shows that the product mass nearly reached plateau around seed mass equal to 89 g/dm^3 crystallizer for 0.5^{o}C/h cooling rate. It implied that the seed mass had insignificant effect after the seed mass reached 89 g/dm^3 crystallizer for 0.5^{o}C/h cooling rate. However, for the simulations with 1.0^{o}C/h cooling rate, the product mass did not reach plateau at all. It could be the process time of 1.0^{o}C/h cooling rate was not long enough for crystallization and therefore, the amount of seed mass still strongly influenced the product yield. Product masses from both cooling rates increased sharply at the beginning and increased slowly as the seed mass increased. As explained in section 6.2.1, the increase of seed mass created both productive and counter-productive effects on product yield. High amounts of seed mass could draw the concentration down drastically at the beginning since the surface area is high. Afterwards, the solute concentrations were not much different from solubility concentrations and therefore, the driving force reduced. The driving force for crystallization is the difference in the solute concentrations and the

solubility concentrations. These phenomena could be explained from Equation 2.28 – 2.31.

Figure 6.9 b) shows the product crystal mass per seed crystal mass versus seed crystal mass for experiments with cooling rate of 0.5 and 1.0^{o}C/h. As can be seen here, as the amount of seed mass increased, the ratio of product mass to seed crystal decreased sharply at the beginning and slower after seed mass equal to 30 g/dm^3 crystallizer. The maximum product to seed crystal mass was 84% and 26% for 0.5 and 1.0^{o}C/h respectively.

As can be seen from Figure 6.9 a) and b), the best condition to run experiments is with the seed mass equal to 10.09 g/dm^3 crystallizer and 0.5^{o}C/h cooling rate. Figure 6.9 a) shows that at this condition, the product mass was approximately 74% of the maximum possible product which was 9.24 g/dm^3 crystallizer as calculated in section 6.2.1. Even though Figure 6.9 b) shows that the ratio of the product to the seed mass was only 68%, this value was still high because the maximum was 84%. In other words, the ratio was 81% of the maximum. Therefore, it is satisfactory to find the condition that both product mass and seed mass ratio were around 80% of the maximum.

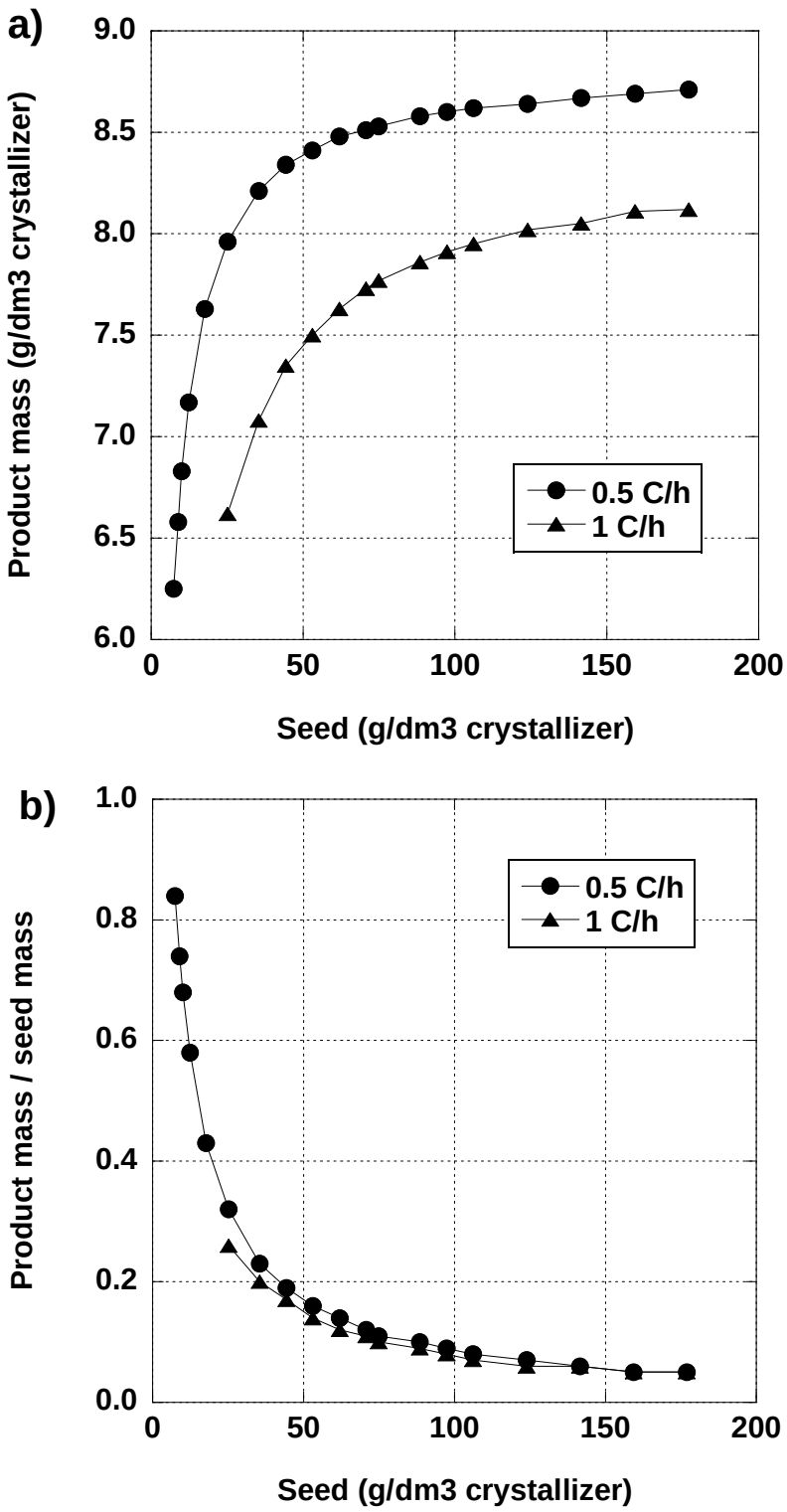

Figure 6.9: Simulated results of a) product crystal mass versus seed crystal mass and b) product crystal mass per seed crystal mass versus seed crystal mass for experiments with cooling rate of 0.5 and 1.0^{o}C/h.

The experiments were carried out at the conditions of 10.09 g seed crystals/dm^3 crystallizer and 0.5^oC/h cooling rate. Figure 6.10 a) shows a plot of average concentrations ± standard deviation versus temperature. The concentrations reduced as the process were carried on and stayed in the metastable limit zone. Therefore, no primary nucleation of undesired species occurred. As shown in Figure 6.10 a), the metastable limit was almost reached at the end of the process. According to Figure 6.9 a), this could come from that the seed mass of 10.09 g/dm^3crystallizer was close to the seed mass of 7.43 g/dm^3 crystallizer which was the lowest seed mass that the simulations did not reach metastable limit. Concentrations of crystallizing species (D-Glu in V1 and L-Glu in V2) were lower than non-crystallizing species (L-Glu in V1 and D-Glu in V2). Hypothetically, the concentrations of crystallizing species in both vessels should be roughly equal to each other. The same hypothetic could be applied to non-crystallizing species as well that they should be equal to each other in both vessels. However, it is not true here. This anomaly behavior came from the crystal cake in V1 was thicker than in V2. The explanation was given in section 6.2.1. Figure 6.10 b) shows the simulations of these experiments. The simulated results agreed well with the experimental results. The concentration profiles from both simulations and the experiments were very close with each other.

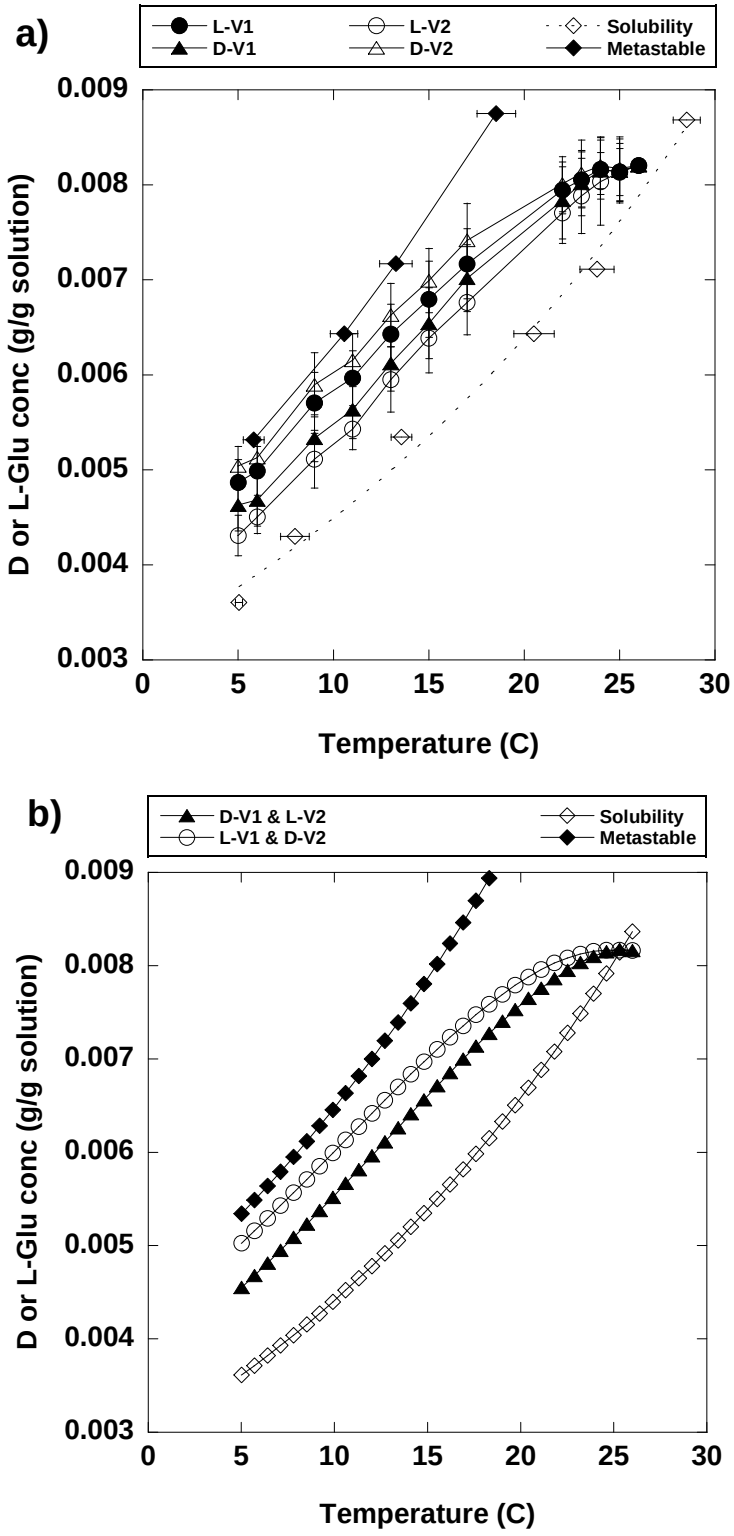

Figure 6.10: Solution concentrations of D and L-Glu versus temperature with seed mass = 10.09 g/dm^3 crystallizer at cooling rate of 0.5^{o}C/h. a) experimental results and b) simulated results. D-Glu seeds were added to V1 and L-Glutamic seeds were added to V2

Table 6.4 shows the summary of the product yield and purity, the expected yield from HPLC calculations and simulations, product mass per maximum possible product, product mass per seed mass, the calculated product yield from preferential crystallization, and the yield enhancement. Table 6.4 shows that the total product masses were close to one another from experiments, HPLC calculations, and simulations. The product mass was over 99.7%. As discussed earlier, this product could be considered pure according to Mullins (2004). The experimental results were slightly lower than the simulated results for the product mass per the seed mass (0.68, model) and the product mass per the maximum possible product mass (0.74, model). Therefore, the experiments agreed well with the model. The yield enhancement of the experiments was 266 – 283% which was considered very high. As can be seen from Table 6.4, the product mass from experiments, HPLC calculations, simulations, and preferential crystallization from V1 were slightly lower than V2. Again, this could come from the fact that the crystal cake on the filter in V1 was thicker than in V2 and it resulted in lower crystallization in V1.

In conclusion, the simulations were carried out to search for the most desirable seed mass use at different cooling rates. The simulations found that the condition with 10.09 g seed crystals/dm^3 crystallizer and 0.5^oC/h cooling rate produced a very attractive amount of product compared to the amount of seed mass invested. Simulations showed that it produced 74% of the maximum possible product mass and 81% of the maximum ratio of product to seed crystal mass. The experiments were carried out at this condition and agreed well with the simulations. The experimental results showed that the product was pure and the product was roughly 6.53 g/dm^3 crystallizer. The product yield enhancement was 266 – 283% which is very high.

Table 6.4: Summary of product yield and purity from experiments with 10.09 g/dm^3 crystallizer seed mass and 0.5^{o}C/h.

	V1	V2
Total product mass recovered* (g/dm^3 crystallizer)	6.37 ± 0.35	6.67 ± 0.34
Percent product purity analyzed by HPLC	>99.7%	>99.7%
Product mass expected from HPLC calculation (g/dm^3 crystallizer)	7.24	6.74
Product mass expected from simulation (g/dm^3 crystallizer)	6.83	6.83
Product mass / seed mass	0.63	0.66
Product mass / maximum possible product mass	0.69	0.72
Product mass from solely preferential crystallization	1.66	1.82
Yield enhancement from preferential crystallization (g/dm^3 crystallizer)	283%	266%

* Average ± a standard deviation

6.2.4 Effects of membrane properties on chiral separation

Through section 6.2.1 to 6.2.3, the variables investigated were involved with the crystallization aspects. These variables are surface area of the seed crystals (various seed mass), the amount of time (various cooling rates), and the metastable limit concentrations (various cooling rates). In this section, the effects of membrane properties on chiral separation were investigated.

As shown in section 2.5, the variables involving membrane properties are the membrane surface area, the membrane thickness, the pore tortuosity and the pore porosity.

Practically, it is quite simple to increase the surface area by increasing the number of the module. However, it is not quite easy to vary the rest of the variables because the manufacturer might not produce one. First, the thickness of the membrane wall is preferred to be as thin as possible so that the transport barrier is reduced. In the experiments, the thickness of the hollow fiber membranes was measured to be 135 μm. If the membrane thickness is too thin, the fiber is easily collapsed during operations. Second, the pore tortuosity is desired to be one so that the effective diffusivity in Equation 2.24, $D_e = \frac{\varepsilon}{\tau} D_v$, is maximized. In the experiments, the pore tortuosity was assumed to be unity already. Third, the porosity of the membrane layer was preferred to be as high as possible to increase the effective diffusivity in Equation 2.24, $D_e = \frac{\varepsilon}{\tau} D_v$. In the experiments, the hollow fiber porosity was 40%. To increase the porosity of the membrane, the process is at risk because the membrane might not be stable and could collapse easily. Therefore, in these simulations, the only membrane variable studied was the membrane surface area due to the practical production and assembly of the hollow fiber membranes.

Simulations were carried out to study the effects of the membrane area with different seed mass and cooling rates. The membrane area range was from 9,180 – 100,000 cm^2/dm^3 crystallizer. The current hollow fiber membrane module had the area of 5,187 cm^2 or 9,180 cm^2/dm^3 crystallizer. It was calculated by the inner diameter = 0.5 cm, length = 63.5 cm, and the number of fiber = 520. Theoretically, the membrane could be constructed to have the surface area larger than the solution volume one hundred times.

Therefore, the upper limit is one hundred times larger than a crystallizer volume or 100,000 cm^2 membrane area/ dm^3 crystallizer.

The seed masses used were equal to 25.22 and 74.87 g/dm^3 crystallizer. The cooling rates used were 0.2, 0.5, 1.0, 5.0, and 10.0^oC/h. The simulated results were shown only if the experiments were successful or in other words, the metastable limit was not exceeded. The simulations showed that the metastable limit was reached with cooling rates of 0.2, 5.0, and 10.0^oC/h for the whole range of membrane surface area studied. The metastable limit was reached for 0.2^oC/h because the metastable gap was very small. For 5.0 and 10.0^oC/h, the metastable limit was reached because the process was too quick to allow the solute to grow on seed crystals. Then, the concentrations did not reduce enough and eventually reached metastable limit.

Figure 6.11 shows the plot of product mass versus membrane surface area. The product mass increased sharply with the membrane surface area until the membrane area reached 30,000 cm^2/dm^3 crystallizer. The product mass reached constant around the membrane area equal to 53,100 cm^2/dm^3 crystallizer. It could be explained that at a lower range area of the membrane, the transmembrane mass transport depended on membrane area which was a primary resistance. As the membrane area increased sufficiently to transport the solute molecules at an infinite rate, the transmembrane transport no longer depended on the membrane area. In this system, the mass transfer resistance due to membrane is negligible at the membrane area equal to 53,100 cm^2/dm^3 crystallizer. The experiments were not carried out at this membrane area because of extremely expensive experimental set up to investigate the obvious effects on the membrane area on this hybrid chiral separation process.

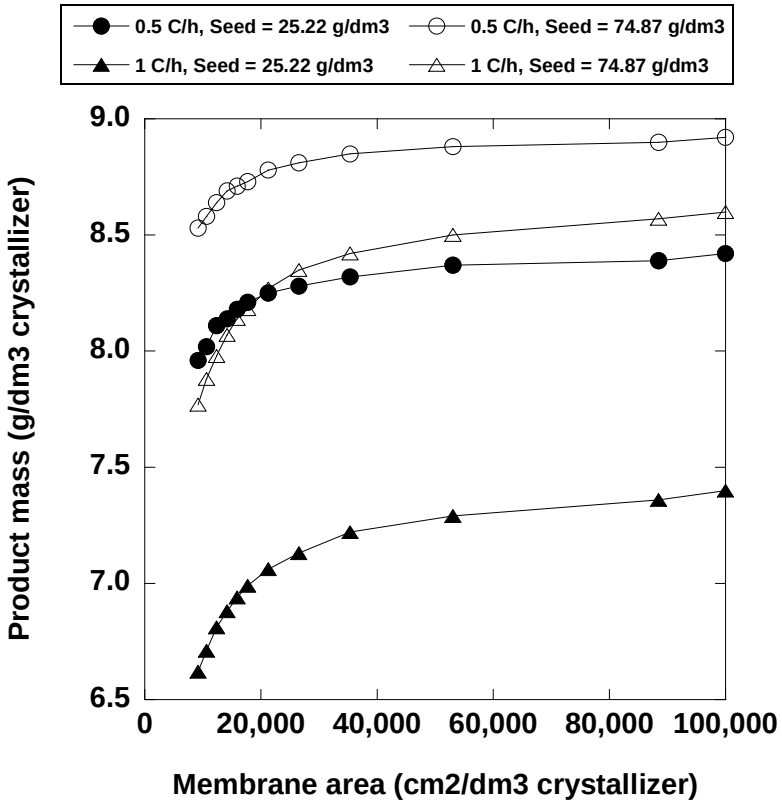

Figure 6.11: Product mass versus membrane surface area with seed mass of 25.22 and 74.87 g/dm^3 crystallizer and cooling rates of 0.5 and 1.0^{o}C/h

The amount of seed mass also had effects on the crystallization transport as the seed mass provided the surface for crystallization. The larger surface of seed mass, the faster the solutes grow and the faster decrease of the solute concentrations to create higher chemical potential across the membrane. As expected, the product mass from seed mass equal to 74.87 g/dm^3 crystallizer was higher than the seed mass equal to 25.22 g/dm^3 crystallizer due to a higher seed crystal surface area. The product mass from 0.5^{o}C/h cooling rate was higher than 1^{o}C/h cooling rate because of the longer time for crystallization. The gap between product mass from 25.22 g seed crystals/dm^3 crystallizer at two cooling rates was larger than one from 74.87 g seed crystals/dm^3 crystallizer. This could come from the high seed surface area withdrew the solute

concentrations quite low and close to the solubility at the beginning as shown in Equation 2.32, $dM/dt = J_c A_c$. Hence, the driving force for crystallization was not very high as shown in Equation 2.29, $J_c = K_G \rho_s (w-w^*)$. Therefore, giving more time by decreasing the cooling rate did not increase the product mass as much as it should be. This behavior was explained in detail in section 6.2.1.

6.3 Conclusions

In this chapter, the chiral separation via a hybrid of preferential crystallization and hollow fiber membrane barrier was studied. The objectives of the study in this chapter were to improve our established hybrid chiral separation process from the previous chapter and to study process variables to determine appropriate conditions for chiral separation. In this chapter, the membrane module was changed from a flat plate membrane to hollow fiber membrane to increase mass transfer across the membrane and therefore, to avoid concentrations exceeding the metastable limit. The product yield and purity were expected to be increased from the previous chapter (37 to 404%).

The process variables relating to the crystallization process were the amount of seed mass and cooling rates. The seed mass amount represented the surface area for crystallization. The experiments and the simulations were carried out with various seed masses of 3.98, 25.22, and 74.87 g/dm^3 crystallizer at a constant cooling rate of 1.0^{o}C/h. The results showed that the experiments with 3.98 g seed crystals/dm^3 crystallizer failed to separate DL-Glu mixture while experiments with 25.22 and 74.87 g seed crystals/dm^3 crystallizer produced pure product. Experiments produced 5.84 and 7.24 g product/dm^3

crystallizer from seed mass equal to 25.22 and 74.87 g/dm^3 crystallizer respectively. The higher seed mass provided a larger crystallizing surface area and therefore, the product increased when seed mass increased. The product yield enhancement was 233 – 404% from solely preferential crystallization process. This enhancement proved that this process is revolutionary compared to the traditional preferential crystallization process. The value of K_G was estimated as 0.0025 cm/min by fitting the model to the experimental results. As discussed earlier, K_G was controlled by k_r which is the surface integration growth rate. As K_G did not change with the temperature, it shows that activation energy in the surface integration process was very low as shown in Equation 2.10. The estimated K_G was used further in the model to predict and to explain the system behavior later on.

As the experiments were successful with different seed mass at a constant cooling rate, the experiments and simulations were carried out at a constant seed mass with different cooling rates. The seed mass used was 25.22 g/dm^3 crystallizer because the increase of seed mass to 74.87 g/dm^3 crystallizer increased little product mass. It is quite difficult to produce seed mass. The cooling rates were 0.5, 1.0, and 5.0^{o}C/h. The experiments failed with the 5^{o}C/h cooling rate because the time was not enough for crystallization and the metastable limit was exceeded. The product increased from 5.84 to 7.81 g/dm^3 crystallizer when the cooling rate decreased from 1.0 to 0.5^{o}C/h. This is because the slower process allowed more time for the product to crystallize. The yield enhancement of different cooling rates was 191 – 404% compared to preferential crystallization. This is considered a huge improvement from traditional crystallization process. The simulations agreed well with the experiments. The simulations also

suggested that the experiments should not be done at cooling rates of 0.2 and 1.0^{o}C/h as the metastable limit would be reached.

The problem arose that the product obtained was much lower than the seed mass invested. Therefore, the process simulations were carried out to find the desirable seed mass that gave a high ratio of product to seed mass and high product mass. The simulations were carried out with varied seed mass from 3.98 – 177 g/dm^3 crystallizer and cooling rates of 0.2, 0.5, 1.0, 5.0, and 10.0^{o}C/h. The desirable seed mass was 10.09 g/dm^3 crystallizer at 0.5^{o}C/h because it gave product mass equal to 74% of the maximum possible product mass and gave the ratio of product to seed mass equal to 81% of the maximum ratio. The experiments were run at this condition and the experimental results agreed well with the model. The product mass was approximately 6.53 g/dm^3 crystallizer. The yield enhancement from preferential crystallization was 266 – 286% which is considered high.

The process variables studied so far were involved with crystallization kinetics, crystal surface area and cooling rates. Next, the process variables involving the membrane were studied. The variable here was the membrane surface area because it was the only practical variable that could be changed in this setting. The simulations studied the effect of the membrane area on chiral separation. As expected, the product yield increased as the membrane surface area increased and stayed constant. The product yield remained constant when the membrane area reached 53,100 cm^2/dm^3 crystallizer. It shows that the mass transfer resistance due to the membrane was negligible with this membrane area.

Overall, the objectives of this chapter were reached. The experiments show a significant improvement in product yield and purity with the set up with hollow fiber membranes compared to the set up with a flat plate membrane in previous chapter. The yield enhancement was up to 404% from the hollow fiber membrane set up improving from up to 65% from the flat plate membrane set up. The process variables involving mass transfer resistances due to crystallization and membrane were studied. The appropriate seed mass was found from the simulation and confirmed by the experiments. The experimental and simulated results show that this hybrid process is revolutionary. It increased the product purity to >99.7% and also increased the product yield up to 404% from preferential crystallization itself.

CHAPTER 7

EXTENSION TO OTHER SYSTEMS

The novel chiral separation process through the hybrid of crystallization and a membrane barrier has shown the promise through extensive studies in both experiments and simulations. The hybrid process has shown revolutionary results that the product purity was over 99.7% and the product yield increased up to 404% compared to traditional preferential crystallization. Up to this point, the novel process was studied for the separation of DL-glutamic acid which is categorized as a racemic conglomerate. The experiments were carried out thoroughly for the separations of one of the racemic conglomerate mixtures and had shown the process promise. Therefore, the hybrid process could be applied to other racemic conglomerate systems because of their similarity in solubility behaviors to DL-glutamic conglomerates.

Around 10% of racemic mixtures are racemic conglomerates while approximately 90% are racemic compounds. In this chapter, the hybrid process was attempted to separate racemic compounds because of their large proportion in the market. As stated earlier, the racemic compounds must fit into three criteria in section 2.3.2 to be successfully separated by this hybrid process. The easiest way to check if the process is feasible is to measure the metastable limits of the racemic compounds according to criterion 2. The test model in this chapter is DL-leucine (Leu). The hypothesis is that if the metastable limit concentrations of DL-Leu are higher than the solubility concentrations of D or L-Leu, it means that the metastable form of D or L-Leu could be formed on its own species seed crystals while the metastable limit of DL-Leu is not

reached. Therefore, this hybrid process could possibly apply for separation of DL-Leu. In this chapter, the significantly large cooling rate of 20.0°C/h was used. If the metastable limit of DL-Leu is lower than the solubility of L-Leu, then this hybrid process does not work for DL-Leu. It is even more impossible at the lower cooling rate. The lower the cooling rate is, the smaller the gap between the metastable limit and solubility is. The use of cooling rate higher than 20.0°C/h is not practical. In general, the overall growth rate coefficient is very small, for example, the overall growth rate coefficient of D or L-glutamic acid was 0.0025 cm/min. At a much higher cooling rate, the time for crystallization and mass transport across the membrane is much less. Therefore, the product yield would be very small and the impurity would be very large. It is because the undesired species could not be transport across the membrane fast enough and eventually primarily nucleated.

7.1 Experiments

The metastable limits were measured according to the procedures in section 4.1. Three concentrations of DL-Leu were used for the metastable limit measurements. These three concentrations correspond to the solubility concentrations at 25, 50, and 75°C (Yalkowsky and He, 2003). The cooling rate was 20.0°C/h. The experiments were repeated 6 times and the standard deviation of the measured temperatures was within 7%.

7.2 Results and discussions

Figure 7.1 shows the solubility data of DL-Leu and L-Leu (Yalkowsky and He, 2003) and the metastable limit of DL-Leu (this study). The concentrations of DL-Leu

were divided by two in order to compare the concentrations based on one enantiomer. As can be seen from Figure 7.1, the metastable limits of DL-Leu were much lower than L-Leu solubilities. The temperature gap was approximately 17°C between the solubility and metastable limit of DL-Leu at the same concentrations.

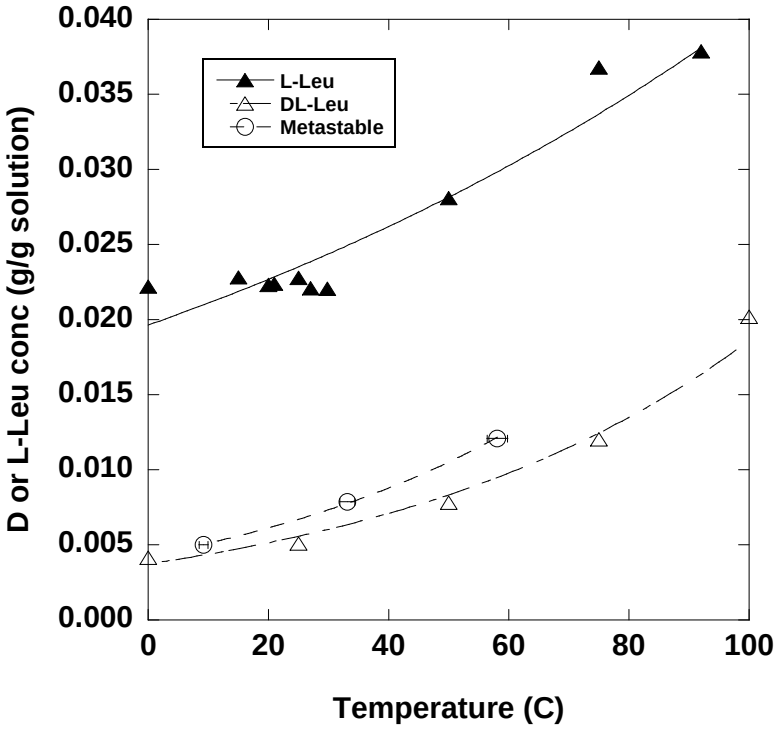

Figure 7.1: Solubility of L and DL-leucine (Yalkowsky and He, 2003) and metastable limit of DL-leucine with a cooling rate of 20.0°C/h. The concentrations are based on one enantiomer.

As can be seen from the results in Figure 7.1, the metastable limit concentrations of DL-Leu were less than the solubility concentrations of L-Leu. Therefore, it was impossible to form metastable L-Leu crystals and this process is not feasible for separating DL-Leu.

7.3 Process design variables

The separation of chiral isomers through preferential crystallization coupled with a membrane barrier was studied using the racemic conglomerate mixture of L and D glutamic acid as a model system. It is expected that the design of separations involving other racemic conglomerates can follow the example of glutamic acid separation. On the other hand, if a mixture forms racemic compounds or pseudoracemates, then the three criteria in section 2.3.2 must be met in order to use the hybrid process examined in present work. The three criteria in section 2.3.2 are also suitable for consideration of separations involving close solubilities and that co-crystallize in the same lattice. After first determining that the hybrid process is feasible for the mixture of interest, it is important then to consider the following process design variables in order to employ it for the separation of other systems.

1. Dependence of the solubility on temperature. The greater the reduction in solubility with decreasing temperature, the greater the recovery of product for a given decrease in temperature.
2. Operating temperature. The larger the cooling temperature range, the larger the product recovered at a given initial temperature. Not only solubility increases with temperature but also mass transfer coefficient from bulk transport (k_c), mass transfer coefficient from surface integration (k_r), and overall crystal growth rate coefficient (K_G). As crystal growth rate increases at higher temperature, the concentrations of desired species in both vessels greater decrease, giving a greater driving force for transport across the membrane. As a result, the product purity increases as well as the product yield.

3. Mass of seed crystals. Larger amount of seed crystals provides larger surface for greater crystal growth rate. As a result, both product yield and purity increase as described in number 2. As the mass of seed crystals increases, the product mass may increases as long as equilibrium is not reached. It is not wise to invest large amount of seed mass to obtain little amount of the product in return because the production of seed mass is difficult and expensive as discussed in section 3.2.3.
4. Seed crystal size. The smaller crystal size provides more crystal surface area per crystal mass, giving greater crystal growth rate. Therefore, the product yield and purity increase.
5. Seed crystal polymorph. Polymorphism has significant effects on crystal growth rate. Each polymorph provides different surface area per volume for crystal growth. In addition, the solubility of the stable polymorph is lower than the metastable polymorph, giving greater chemical potential for crystal growth. Moreover, each polymorph has a different mass transfer coefficient due to surface integration. Also, the chosen polymorph must not transform into another polymorph during the course of operation.
6. Metastable limit. The metastable limit must not be reached to avoid spontaneous nucleation of undesired species.
7. Cooling rate. An operation with slower cooling rate provides longer time for crystal growth, allowing greater reductions in the concentrations of desired species. This results in larger chemical potential differences across the membrane. Therefore, the mass transport rates across the membrane for both desired and undesired species increase, resulting in an increase of product yield and purity.

However, at very slow cooling rate, the metastable zone is very small and the metastable limit can be reached more readily, risking a compromise of product purity

8. Solvent selection. Solvent has significant effect on the solubility, the metastable limit, k_c, k_r, and K_G.
9. Mixing intensity. The solution must be well-mixed. And the crystals must be uniformly suspended in the solution. Increasing mixing intensity beyond that required to accomplish these objectives risks significant crystal fracture and concomitant loss of crystal purity.
10. Membrane area. Larger membrane area increases the transport rate across the membrane, resulting in the increase of the product yield and purity. However, the increase of product yield stops at a certain membrane surface area as equilibrium is reached. The membrane area can be very expensive. Therefore, it is important to consider the cost of the membrane.
11. Membrane pore size. The membrane pore size must be small enough to block crystals from moving across the membrane. Experience with the present system was successful at achieving this objective when using a pore size smaller than 0.1 times the smallest seed crystal.
12. Membrane porosity. The increase of membrane porosity results in the increase of effective diffusivity across the membrane, resulting in the increase of the mass flux across the membrane. In general, the commercial membrane porosity is 40%. If the membrane porosity is too high, the membrane structure collapses easily.

13. Membrane pore tortuosity. Greater pore tortuosity reduces the effective diffusivity across the membrane as the diffusion pathway is longer.
14. The membrane thickness. Thinner membrane gives shorter distance for transport across the membrane resulting in the increase of mass flux. However, too thin membrane can break easily.
15. Membrane material selection. The membrane material must not react with chemicals in the process and the membrane pore structure must not be deformed during operation. The hollow-fiber membrane must be capable of maintaining integrity at the highest operating temperature in the process. The flat plate membrane can be made of either polymer or ceramic material. Ceramic membranes are very brittle and easy to break but can withstand very high temperature without the deformation of pore structure.
16. The membrane module. A hollow-fiber membrane module is more robust than a flat-plate module because it is easier to construct and it can be subject to greater variations in operating conditions. In addition, hollow-fibermembranes provide larger surface area for transport in a much smaller module volume than is possible with a flat-plate membrane.

7.4 Conclusions

DL-Leu was used as a test model for racemic compound separation. The metastable limit properties of DL-Leu were tested to investigate the feasibility of using this hybrid process. The experimental results showed that the metastable concentrations of DL-Leu were less than the solubility concentrations of L-Leu. It means that it was not possible to form metastable crystal of L-Leu without reaching the metastable limit of DL-Leu. Therefore, it was not possible to separate DL-Leu by the hybrid process. The important process design variables were listed here if the hybrid process is considered for the separation of other systems.

CHAPTER 8

CONCLUSIONS AND RECOMMENDATIONS

8.1 Conclusions

Over fifty percent of approved drugs world-wide are chiral. Common chiral drug synthesis produces racemic mixtures without the presence of asymmetric catalysts. In general, only one enantiomer is active but the other one did not perform activities, often inhibits the activities, generates side effects or creates toxicity. Therefore, the separation of racemic mixtures is crucial.

The novel chiral separation process was proposed as the hybrid process of preferential crystallization and a membrane barrier. The primary objective of this thesis was to establish an efficient alternative chiral separation process in term of the product yield and purity. The secondary objective of this thesis was to determine the importance of the process variables to achieve the highest purity product with an excellent yield. The research was carried out primarily through experiments. Mathematical simulations were created as a guide to which directions the experiments should be on.

The fundamental of this proposed process is to control the crystal growth of pure enantiomer on the opposite sides of a permeate membrane. The membrane was non-enantioselective but could block the crystals.

The research started with the measurement of solubility and metastable limits as they were the process boundaries. The measured solubility concentrations were in the same range with the data found in literatures (Apelblat and Manzurola, 1997; Dalton and Schmidt, 1993). The metastable limits were measured for 5 different cooling rates, 0.2,

0.5, 1.0, 5.0, and 10.0^{o}C/h. From the plot of the concentration versus temperature, the results showed that the faster the cooling rate, the further away the metastable limit. This is because the solute molecules need a certain period of time to move around in the solution to attract other molecules to form a nucleus. With the same period of time, the solution temperature for a fast cooling rate reduces lower than the one from a slow cooling rate. Now the process boundaries were found.

The basic set up with the flat plate membrane was designed and built first to determine the feasibility of the process. Then, the advance set up with hollow fiber membranes was designed and constructed to improve the process and investigate the effects of the operating conditions on the separation performance. The temperature was cooled at 1.0^{o}C/h from 40^{o}C to the middle of the metastable zone gap at 37^{o}C and remained constant for 7 hours to determine the crystal growth rate of the process. The experiments were carried out with two levels of seed mass, 3.50 and 22.20 g/dm^{3} crystallizer to investigate the effect of amount of seed crystal surface area on the product yield and purity. The experiments showed that with 3.50 g seed crystals/dm^{3} crystallizer, the solute concentrations decreased slightly along the process because less seed mass provided less crystal surface for the solute to grow on. On the other hand, the experiments with 22.20 g seed crystals/dm^{3} crystallizer showed that the solute concentrations dropped significantly as expected because of larger seed crystal surface area. As expected, the higher seed mass produced more product. The product purity of all experiments was in a range of 94 – 98%.

For both seed masses, the solute concentrations decreased slightly after the temperature was kept constant for 7 hours. This result showed that the crystal growth

rate was very slow. Therefore, the overall growth rate constant (K_G) was estimated through the experimental results with the aid of the mathematical model. It showed that the overall growth rate was controlled by the surface integration process. The value of K_G was used further for experimental planning and prediction for hollow fiber membrane set up.

In conclusion, the experimental results showed the feasibility of this process through the set up with a flat plate membrane. The yield enhancement of this hybrid process was up to 65% from preferential crystallization and the product purity was over 94%. However, the calculations showed that the surface area of the membrane was the process limitation. The undesired species could not transport across the membrane fast enough; therefore, the metastable limit would be reached and the process had to stop. By increasing the surface area of the membrane, not only the product purity but also the product yield was expected to increase. As the cooling range increases, the difference in solubility concentrations at the beginning and at the end increases and therefore, it allows a larger amount of solutes to crystallize. The results were hoped to be improved by using the set up with hollow fiber membranes that has a significant larger membrane surface area.

The set up with hollow fiber membranes were constructed and tested with several designs before the final. The use of the hollow fiber membrane set up was planned to improve the product yield and purity from the previous set up and to show a significant improvement from the preferential crystallization. The experiments and the simulations were carried out to investigate all process possible variables of the process. The process variables could be determined from the concentration evolution in the vessel through

Equations 2.38 through 2.41. Equations 2.38 and 2.39 are shown below for the concentration evolution in vessel 1.

$$\frac{dw_{D,V1}}{dt} = \frac{J_{v,D}A_M}{V_1\rho_s} - \frac{N_D J_{c,D,1} A_{c,D}}{V_1\rho_s} = \frac{1}{V_1}\left(\frac{D_e A_M}{l}(w_{D,2} - w_{D,1}) - N_D A_{c,D} K_{G,D}(w_{D,1} - w_D^*)\right)$$

Equation 2.39

$$\frac{dw_{L,V1}}{dt} = -J_{v,L,2}\frac{A_M}{V_1\rho_s} = -\frac{D_e A_M}{V_1 l}(w_{L,1} - w_{L,2})$$

Equation 2.40

As can be seen from the above equations, the variables can be listed as follows.

1. The membrane area per a crystallizer volume ($\frac{A_M}{V}$). This variable was studied from the flat plate membrane set up to the hollow fiber membrane set up. However, no experiments were studied by varying the membrane surface area of the hollow fiber membranes. Only simulation studies were carried out. The membrane area could not be changed experimentally due to its very expensive cost. The vessel volume was fixed due to the construction.
2. The membrane thickness (l). This variable was constant in the process. The membrane module was purchased and this value is fixed.
3. The effective diffusivity (D_e). This value could not be manipulated in this process. Effective diffusivity depends on bulk diffusivity and the membrane porosity and tortuosity. Again, the membrane module was purchased and the porosity and the tortuosity are fixed.
4. The total surface area of seed crystals per a crystallizer volume ($\frac{N A_c}{V}$). This variable was studied by varying 4 levels of the seed crystal mass, 3.98, 10.09,

25.22, and 74.87 g/dm^3 crystallizer through the experiments and the simulations.

5. The overall growth coefficient (K_G). This variable was assumed to be constant.
6. The metastable limit concentration (w*). The metastable limit concentrations were varied with 5 levels of cooling rates, 0.2, 0.5, 1.0, 5.0, and 10.0^{o}C/h. The effects of this variable were investigated through the experiments and the simulations.
7. The process time (t). The process time was varied with the cooling rate. The slower the cooling rate is, the longer the process time is.

After all of the process variables were determined, the experiments were planned and carried out with the help of the simulations. First of all, the investigation started with the experiments at a constant cooling rate of 1.0^{o}C/h with various seed mass, 3.98, 25.22, and 74.87 g/dm^3 crystallizer. Only the experiment with the seed mass of 3.98 g/dm^3 crystallizer failed to separate DL-Glu by having metastable limit reached. The other experiments succeeded the separation by producing over 99.7% purity product. The experiments with 25.22 g seed crystals/dm^3 crystallizer generated less product than the ones with 74.87 g seed crystals/dm^3 crystallizer. However, the increase of the product compared to the increase of seed mass used was satisfactory. Therefore, 25.22 g seed crystals/dm^3 crystallizer was chosen for the separation with different cooling rate in the next step. The experiments with 25.22 g seed crystals/dm^3 crystallizer had the yield enhancement from preferential crystallization up to 403% which was significant and

showed the process had promise. The simulation results agreed well with the experiments.

Next, the effects of cooling rate on separation process were investigated. The experiments and the simulations were carried out at a constant seed mass of 25.22 g/dm^3 crystallizer with different cooling rates of 0.5 and 5.0^{o}C/h. The 0.5^{o}C/h experiment generated a larger amount of product from the 1.0^{o}C/h experiment because 0.5^{o}C/h experiment allowed more time for solutes to crystallize. However, the 5.0^{o}C/h experiment failed the separation process. The metastable limit was reached because the 5.0^{o}C/h experiment allowed insufficient time for crystallization and for exporting undesired species across the membrane.

The simulations were carried out further with cooling rates of 0.2 and 10.0^{o}C/h. The simulation results showed that both runs failed the separation because the metastable limit was reached. The metastable limit was reached for the 0.2^{o}C/h run because of a very narrow metastable limit zone gap. On the other hand, the metastable limit gap of 10.0^{o}C/h was quite large but the metastable limit was reached because of insufficient time for crystallization and for the export of undesired species across the membrane. According to the simulation results, the experiments were not carried out at 0.2 and 10^{o}C/h cooling rates.

As the experimental results showed promise of the process, the simulations were carried out further to determine the appropriate operating conditions so that the ratio of crystal product per seed crystal mass was maximized but the product yield remained high. The simulations were run at the cooling rates of 0.2, 0.5, 1.0, 5.0, and 10.0^{o}C/h with the seed mass varied from 3.98 – 177 g/dm^3 crystallizer . Only runs with 0.5 and 1.0^{o}C/h

cooling rate provided the conditions so that the metastable limit was not exceeded. With the 0.5^{o}C/h cooling rate, the product yield increased with the increase of seed crystal mass and reached constant when the seed mass approached 88.50 g/dm^3 crystallizer. The desirable condition was determined to be with 10.09 g seed crystals/dm^3 crystallizer and 0.5^{o}C/h cooling rate. At this condition, the ratio of product crystal mass per seed crystal mass was 0.65. The product yield was 71% of maximum possible yield. The experiments were carried out at this condition to confirm the simulated results. The product yield from the experiments was very close to the one from the simulations and the experimental product purity was over 99.7%. The yield enhancement from the experiments was up to 283% from preferential crystallization. So far, the experimental results showed that this hybrid process was revolutionary for chiral separation as it increased the yield from preferential crystallization enormously while maintaining very high purity product over 99.7%.

As the experiments proved the promise of this process with existing experimental apparatus, the simulations were carried out for the set up with various membrane surface areas. The simulations were run at various seed mass and various cooling rates. As expected, the product yield increased with the increase in membrane surface area and reached constant at the surface area of 53,100 cm^2/dm^3 crystallizer which is approximately 6 times larger than the current set up. The experiments were not conducted to confirm the results because the cost of the set up would be extremely expensive to confirm the obvious separation behaviors.

So far, the hybrid process was applied to a racemic conglomerate system, DL-glutamic acid. The experimental and simulation results showed the strong promise of this

hybrid process. The process was also tested if it would be feasible for racemic compounds. The preliminary experiments were carried out for DL-leucine as a test model. The solubility and metastable limit behaviors showed that this hybrid process was not feasible for separation of DL-leucine. The experiments were not carried out further for other racemic compound systems as the solubility behaviors founded from literatures of several amino acids did not show any promise for success in separation. However, it is hypothetically possible for appropriate systems as discussed in section 2.4.2.

In conclusion, the chiral separation through the novel hybrid of cooling crystallization and a membrane barrier was studied thoroughly via the experiments and simulations with DL-glutamic acid as a test model. The set up with hollow fiber membrane produced the highest product yield and purity and the highest improvement from cooling crystallization. The experimental results showed the yield enhancement of the process was up to 283% from preferential crystallization with the purity over 99.7% with the appropriate seeding conditions. With the presence of a membrane, the cooling crystallization process can continue at a large cooling range at once while the cooling crystallization alone must stop several times to cover the same range because it could not export the undesired species across the membrane resulting in crossing metastable limit. Therefore, this process can save energy, time, and resources especially the seed crystals as the seed crystals are introduced only once and the process continues until the end without a stop. This novel process not only increases the product yield and purity but also saves energy, time, and resources. It proved that this process is revolutionary and a great alternative for a chiral separation.

With the insight understanding of the test model from this thesis, the process can be extended to separate the systems similar to DL-glutamic acid such as other racemic conglomerates or the system that the mixtures do not co-crystallize in the same lattice in a stable form.

8.2 Recommendations

Even though the experimental and simulation studies were carried out thoroughly and the results showed a great promise of the novel hybrid process, there are a few issues that could be addressed here for consideration for more effective use in the future.

1. For a large scale production, the membrane surface area should be increased to the point that the mass transfer resistance due to the membrane is no longer significant. For example, in this process, the simulations showed that the product yield reached the constant at the membrane surface area around 53,100 cm^2/dm^3 crystallizer. The experiments were not carried out with this set up because of the extremely expensive set up. However, for a large scale continuous production, it would be beneficial to invest in the membrane units to receive the highest production.
2. The membrane module could be designed differently so that the solution flow rates to the membrane module of both tube and shell sides are equal. As discussed in Chapter 6, the seed crystals formed thinner cake in the vessel that the solution was pumped at a faster rate; in this case, it was vessel 1 in which the solution was pumped to the shell side. This is because the flow rate to the shell side was larger to ensure that the pressure across the membrane was negligible as discussed in section 3.1.2.3. As the cake on the filter surface was thicker in one

vessel than the other, the crystallization rates were different in both vessels due to different amounts of seed crystals available for crystallization. Therefore, the concentrations between both vessels behaved differently. The concentrations of non-crystallizing species also behaved the same. This could be a problem in a larger scale production because the product does not crystallize at the highest rate. To ensure that the flow rate of the shell side (F_s) is relatively close to the tube side (F_t), the hollow fiber membrane module design should follow Equation 3-19, $\frac{F_s}{F_t} = \frac{1}{18.75}\frac{S_M D_p^2}{\pi n R^4}\frac{\varepsilon^3}{(1-\varepsilon)^2}$. As can be seen here, the variables are the cross-sectional area of the module (S), the effective particle diameter (D_p), the number of the fibers (n), the fiber inner radius (R) and the shell side porosity (ε). If these variables could be adjusted so that $F_s/F_t \rightarrow 1$, then the problem would be minimized. The membrane module in this thesis was purchased; therefore, it could not be justified.

3. The solution inlet filtration unit could be improved. The vibrator was used to shake the cake off the top of the inline filter and it was not an ideal set up in a large scale continuous production. A better alternative of using a vibrator is proposed here. Instead of having one direction flow, the intermittent reverse flow is applied so that the cake on top of the filter is pushed off. For example, the normal flow is applied for 1 minute and the reverse flow is applied for 5 seconds. This could get rid of the cake easily and the process is more stable as it does not have to control the continuous vibration for a long period of time. The reverse flow was not used in this work because a programmable reversible peristaltic pump is not available in a reasonable price range.

4. The control of the pressure across the membrane to be negligible could be a big issue for a large scale production. The pressure across the membrane must be negligible. The variable setting of the process is very tight. Therefore, a very well controlled system must be used for a larger scale production. There is also an alternative for the pressure problem. If the hydrogel could be coated as a very thin layer inside the hollow fiber bores, the trans-membrane pressure would no longer be an issue. Hydrogel acts as a non-porous dense layer and therefore, the flow across the hydrogel would automatically be diffusion not convection. The production of the hollow fiber membrane with hydrogel coated inside is a big challenge. I had done some experiments trying to synthesis hydrogel inside the hollow fibers but there were so many problems. The issues regarding this hydrogel synthesis will be addressed in the Appendix B.
5. The estimation of k_c and k_r can be improved. To estimate k_c and k_r, it is essential to know precise crystal surface area which is derived from the crystal size, aspect ratio, and number. In the current process, the current crystals are needles and it was not possible to control the crystal size, aspect ratio, and number. First of all, the size distribution was not well-defined. The crystals were sized through the sieving process. The crystal size could not be well-defined as how the crystals would be oriented to pass through the mesh. Also, the needles tend to pack quite well in the sieving plates resulting in that the smaller needles may not be able to fall through the stack of needles. Second, as shown in Figure 3.9, the crystal aspect ratio was not uniform. Therefore, it was not possible to determine the crystal surface area. Third, the needles tend to break in the vessel as the solution

was stirred by a stir bar. Therefore, the number, the size, and the aspect ratio of the crystals changed during the run. The following ideas are suggested to improve the control of the crystal size, aspect ratio, and number. First of all, the used crystals should have well-defined aspect ratio and not break easily in the process. The appropriate crystal shapes are spherical and granular. Second, the crystal size range must be very narrow. The crystals must not break during the run. Instead of using a stir tank, it is more appropriate to use the fluidized bed to avoid the impeller or the stir bar to break the crystals. With these considerations, the estimation of k_c and k_r should be more effective as the crystal surface area can be well estimated.

APPENDIX A

DESIGNS OF EXPERIMENTAL APPAPRATUS FOR THE SET UP WITH HOLLOW FIBER MEMBRANES

The set up with hollow fiber membranes were designed and constructed several times before the final set up was used. In this section, the previous failed set ups were discussed and discovered what could be learned. The major problem of previous set ups was the crystal blocking issues. To pump the solution from the vessel to the membrane through a peristaltic pump, the seed crystals must be blocked from transporting to the membrane module by the inline filter placed at the end of the inlet transporting tube. As recalled from section 3.1.2, the seed crystals formed a cake layer on top of the inline filter. As the crystal cake gets thicker, the solution flow rate pumped to the membrane module was reduced and more importantly, there were less seed crystals available for solute molecules to crystallize on. As a result, the crystallization rate was reduced unnecessarily. Therefore, the discussion focus will on the design of the crystal blocking unit.

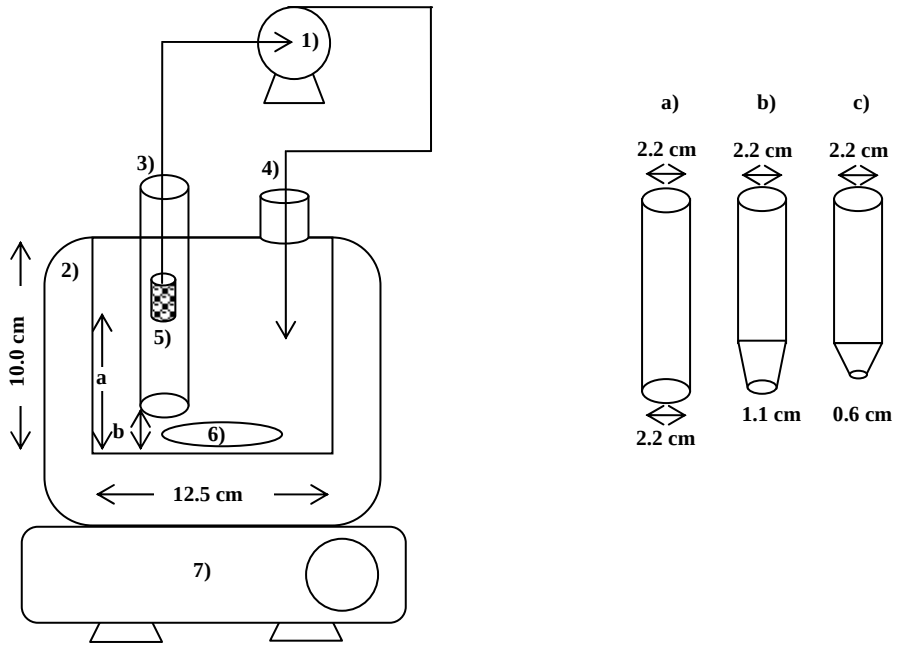

Figure A.1: Experimental apparatus of crystal blocking unit: 1) peristaltic pump, 2) heating/cooling jacket, 3) glass tube (different shapes: a), b) and c)), 4) the vessel neck, 5) 10 μm inline filter, 6) stir bar, 7) stir plate

Figure A.1 shows the schematic diagram of the vessel equipped with the crystal blocking unit. As can be seen from Figure A.1, the tip of the transporting tube was attached to the 10 μm inline filter to block the inline filter. The tip of the transporting tube was placed in the middle of the glass tube inside the vessel. The variables of the design were the height of the tip of the transporting tube, the tip shape of the glass tube, and the height of the tip of the glass tube. The glass tube was placed in the middle of the vessel to block the seed crystals to travel to the inline filter to form a cake layer. Then, the flow rate of the solution pumped out of the vessel was calculated. The basic idea was that the terminal velocity of the smallest crystals had to be less than the superficial velocity of the solution across the glass tube surface so that the crystals would not get

sucked to the filter. The average velocity of the solution in the glass tube can be calculated from Equation A.1.

$$\langle v \rangle = \frac{F}{S} = \frac{F}{\pi r^2} \qquad \text{Equation A.1}$$

$\langle v \rangle$ is average velocity (cm^2/min), F is volumetric flow rate (cm^3/min), S is the cross sectional area of the glass tube (cm^2), and r is the inner radius of glass tube (cm) or equal to 1.1 cm in this case.

The terminal velocity of the seed crystals can be calculated from Equation A.2. Seed crystals are assumed to be a long cylinder. The direction that the particle would be sucked to the filter would be perpendicular with the largest projected area of the particle or along the length of the cylinder.

$$v_t = \sqrt{\frac{2mg}{\rho A C_d}} = \sqrt{\frac{2\left(\rho_s \pi \frac{D_p^2}{4} l\right) g}{\rho D_p l C_d}} = \sqrt{\frac{g \rho_s \pi D_p}{2 \rho C_d}} \qquad \text{Equation A.2}$$

v_t is terminal velocity (cm/min), m is mass (g), g is gravitational acceleration (cm/min^2), ρ is fluid density (g/cm^3), ρ_s is particle density (g/cm^3), A is projected area (cm^2), l is the cylinder length, D_p is the cylinder diameter (cm), and C_d is the drag coefficient. C_d depends on the shape of the particle and the direction of the flow. In this case, the variables are equal to the followings. ρ_s = 1.46 g/cm^3, ρ = 1.02 g/cm^3, g = 3528000 cm/min^2, μ = 0.06 g/cm·min. C_d is a function of Reynolds number (Re) in a laminar flow region (Welty et al, 2000). C_d is a function of Re as interpolated from Figure 12.2 of Welty et al (2000) as shown below.

$$C_d = -44.44Re + 54.44 \qquad \text{Equation A.3}$$

$$\mathrm{Re} = \frac{\rho \langle v \rangle D_p}{\mu}$$ Equation A.4

In the experiments, the minimum flow rate was 15 cm^3/min. The void volume in the shell side is 210 cm^3 and it takes 14 minutes for the solution to travel from and back to the vessel at this flow rate. With the flow rate of 15 cm^3/min, $\langle v \rangle$ was calculated to be 3.94 cm/min and the maximum velocity (V_{max}) was twice as much as the average velocity or 7.90 cm/min. C_d could be calculated from Equation A.3 and A.4,. The v_t was 3.94 cm/min if the D_p = 1.05 μm and 1.90 cm/min if the D_p = 4.15 μm. Only particles with D_p smaller or equal to 4.15 μm would be sucked to the filter.

A.1 Experiments

The glass tube a), b), and c) were constructed and placed at a different height in the vessel. The objective was to find the best design so that the cake formation was minimal. The experimental procedures were as followings.

1. 500 cm^3 of HPLC water was poured into the vessel at room temperature (22^{o}C).
2. 14.25 g of L-Glu seed crystals was introduced into the vessel. The seed crystal size was in the range of 106 – 805 μm. The seed crystals were in the form of needle.
3. The solution was then pumped through a peristaltic pump and returned to the vessel at a flow rate of 15 cm^3/min.
4. The experiment time was 3 hours. The experiments stopped once the majority of the seed crystals formed a cake layer on the inline filter surface.

5. The experiments were carried out using different glass tubes, a), b), and c), showing in Figure A.1. The distance of a and b were varied.
6. The experiments were repeated twice.

A.2 Results and discussions

First of all, the experiments were run without the glass tube. The solution was transported to the pump with the flow rate of 15 cm^3/min. Even though the flow rate was this low, the majority of the seed crystals formed the cake on top of the inline filter after 20 minutes. This showed that most particles had the diameter less than 4.15 μm as estimated.

Next, the glass tube was placed in the vessel. The distance *a* and *b* were varied. The most effective distance *a* was very close to the liquid surface so that the crystals must travel very far to reach the inline filter. The most effective distance *b* was very close to the bottom so that the crystals could not sneak into the tube easily. Tube a) was used first. It was observed that the majority of the crystals formed a cake layer on top of the filter surface and filled a part of the glass tube around the filter. The flow pattern in the glass tube might not be fully developed and there could be some eddies and turbulences from the stirring push the crystals to the top. Therefore, tube b) was used next because the opening was smaller than tube a) hoping that less crystals would travel through the smaller opening to block the inline filter.

As tube b) was used, less amount of crystals coated on top of the filter compared to the results from using tube a) but still significant enough. However, the crystals that could travel through the small opening stuck on the glass tube around the opening

because it has the slope for the crystals to sit on. The crystals could not fall out of the tube because there was a flow coming into the tube and the velocity was faster than 3.94 cm/min since the opening was smaller. After 3 hours, most of the crystals were stacked on the slope and formed a thick layer inside the tube. This was undesirable. Therefore, tube c) was used next as its opening was much smaller than tube b opening.

The experiments were carried out using tube c). The results showed that the cake formed on top of the inline filter was not much different from tube b). This could come from fine particles still travel through the opening and got sucked to the filter. The crystals still stacked up around the opening due to the slope.

The new problem arose as the crystals stacked up around the opening. The new solution was to glue a piece of non-woven fabric to cover the tube opening so that no particles could travel through and no crystals would stack up on the tube ending slope. The experiments were carried out. However, another problem arose. The non-woven fabric mesh was too dense. Once the glass tube was inserted into the vessel, it took roughly 5 minutes for the water to sift through the fabric and to fill in the glass tube. The water could not be transported out of the vessel in time because all the water in the tube was sucked out before the water in the vessel could sip in to fill in the tube again.

As the above problem arose, the new solution was proposed by using a piece of fabric from the female stalking to close the opening of the tube a) instead of the non-woven fabric. However, in this case, a good number of fine crystals were stuck in the stocking fabric and it was undesirable.

Earlier with the experiments before using any fabric to seal the opening, I attempted to check how thick the cake layer on top of the inline filter was by pulling the

inlet transporting tube out of the glass tube. The crystals fell off the filter surface very easily. Therefore, the vibrator was placed on top of the vessel to shake the crystals off the filter and the use of the glass tube became unnecessary. This design by using a vibrator was final and was used throughout the experiments in Chapter 6.

A.3 Conclusions

The design with the glass tube was unsuccessful to minimize the crystal formation on top of the inline filter. However, the idea of using a vibrator to shake the crystal cake on top of the filter came up. The use of the vibrator reduced the formation of the crystal cake layer on the filter. Therefore, the vibrator was utilized for all the experiments.

APPENDIX B

FABRICATION OF HYDROGEL INSIDE HOLLOW FIBER MEMBRANES

The use of hollow fiber membranes filled with hydrogel was proposed so that the existence of pressure drop across the membrane would not be a problem for a system. In this hybrid process, the mass transport across the membrane must be from diffusion so that undesirable enantiomers from both sides of the membrane can be exported. If convective mass transfer occurs, the solution concentration from one side does not change and eventually, the undesired enantiomer concentration will reach the metastable limit and generate impurity. Therefore, the controlling pressure difference across the membrane to be equal is essential. However, it is not easy to control such a system in a large production scale unless the process control system is very sensitive. By having the hydrogel thinly coated inside the hollow fibers, the pressure difference across the membrane is no longer an issue. The hydrogel is dense and can act like a barrier so that convective mass transfer cannot occur. The hydrogel could have 99% water in the hydrogel matrix; therefore, the diffusivity through the matrix is barely reduced. In conclusion, it seems like a good solution because it can block the convective mass transfer and can allow high diffusivity. Acrylic acid was chosen to be the material for this study. Because of its easy polymerization and biocompatible properties, acrylic acid (AA) is widely used to prepare hydrogels designed for drug release (Adnadjevic et al, 2007; Chauhan and Kumar, 2008; Jabbari et al, 2007; Pulat and Asil, 2009). The hydrogel synthesis procedure followed the procedure from Jabbari et al (2007) with adaption.

In general, the hydrogel synthesis is continuous to produce one final hydrogel product. For example (Jabbari et al, 2007) the solution was purged with nitrogen to avoid oxidation and reacted at 50^{o}C in the oven for 1 hour. Then, the solution was post treated in the oven for 12 hours at 30^{o}C to continue the crosslinking process. However, the synthesis procedure here is different because the synthesis was planned to be non-continuous. First, the reaction was planned to stop at a certain point that the solution was viscous enough so that it could stick on the hollow fiber surface. The unreacted solution is not viscous enough and it could not coat the hollow fiber surface. The reaction would be continued after the hollow fibers were coated. The objective of the experiments was to determine the discontinuous procedure so that the hydrogel could be synthesis on hollow fiber surface.

B.1 Experiments

1. The hydrogel solution was prepared by mixing 70 g of HPLC water, 74 g of acrylic acid, 0.5 g of ethylene glycol dimethacrylate (crosslinker), and 0.16 g of azobisisobutyronitrile (initiator) in the glass jar with stirring by a magnetic bar.
2. The solution was poured into 6 of 50 ml flasks. The flasks were closed with a rubber top and argon gas was purged into the solution to get rid of oxygen.
3. All the flasks were heated in the oven at 50^{o}C. Flask 1 (F1) and flask 2 (F2) were taken out of the oven after 30 minutes and placed in the ice box to stop the reaction immediately for 60 minutes. Flask 3 (F3), flask 4 (F4), flask 5 (F5), and flask 6 (F6) were taken out of the oven after 60 minutes. F3 and F4 were placed in the ice box immediately for 60 minutes. F5 and F6 were put in the oven at 30^{o}C right away for 6 hours and placed in the ice box for 60 minutes.

4. After all of the flasks were taken out of the ice box, they were left at room temperature (23^{o}C) for 48 hours to observe the change in their viscosity.
5. The viscosity was determined here whether the solution was viscous enough to coat the hollow fiber surface.
6. The solutions in the even-numbered flasks (F2, F4, and F6) were then continued in the rest of the reaction. F2 was placed in the oven at 50^{o}C for 30 minutes following by 30^{o}C for 12 hours. F4 was placed in the oven at 30^{o}C for 12 hours. F6 was placed in the oven for 6 hours.
7. Then, the flasks were left at room temperature (23^{o}C) for 48 hours to observe the change in their viscosity and compared with the viscosity from the solution in the odd-numbered flasks (F1, F3, F5)

B.2 Results and discussions

The observations of the solution physical property change will be discussed here. The F1 solution viscosity was slightly increased from the pretreated solution showing that the solution was slightly reacted. However, a good amount of unreacted azobisisobutyronitrile (initiator) remained as particle aggregates in the solution. The F2 solution turned to be hydrogel as expected because it went through all the synthesis process. A very little amount of initiator particle aggregates remained in the solution. It seems like this could be a good solution for the process because the solution could go through the synthesis as F1 solution first. The solution would be viscous enough to coat the hollow fiber membrane and the whole coated membrane module could be treated later on to form the hydrogel. The problem is the initiator particle aggregates. The aggregates

would not be able to transport through the hollow fiber bores and the initiator concentration in the solution would not be homogeneous. Therefore, the experiments were carried on further with longer reaction time hoping that the initiator would be all reacted so as to form a homogeneous solution so that the hollow fiber membrane bores would not be blocked.

The F3 and F4 solutions were reacted at 50^{o}C for a longer time which was 60 minutes. The F3 solution did not go through the post-treatment. The F3 solution physical property change was interesting. The viscosity of the solution increased right after the solution was taken out from the oven and put in the ice box. At this point, some amount of initiator aggregates remained in the solution. However, after the solution was left at room temperature for 48 hours, it turned to be hydrogel. That means that the reaction continued at lower temperature. The amounts of aggregates were not noticeably different from when the F3 solution was taken out right after the reaction in the oven. For the F4 solution, the solution was formed as hydrogel before it was post-treated. The F4 solution remained hydrogel after post-treatment. The amount of initiator aggregates were the same as the one in the F3 solution. Therefore, the experiments were carried on further by having the solution partially post-treated so that the initiator aggregates were all used.

The F5 and F6 solutions were treated at 50^{o}C for 60 minutes and at 30^{o}C for 6 hours. The F5 solution physical property change was also interesting. The solution viscosity increased tremendously but did not turn to be hydrogel yet. After it was left at room temperature for 48 hours, it turned to be hydrogel. The F6 solution was hydrogel even before the post-treatment. Very little amount of initiator aggregates were found in

these two solutions. However, they already converted to the hydrogel so it was not possible to coat the solution on the hollow fiber bores.

As can be seen from the experimental results, it was not possible to form the homogeneous solution that was viscous enough to coat the hollow fiber membrane bores. It is important to use homogeneous solution because the initiator aggregates would not block the hollow fiber bores and the fabricated hydrogel layer surface would not have any defects to allow the convective flow through.

The other major problem was that the solution had to be in the oxygen-free environment at all times during synthesis so that no oxidation could occur. This could be a very difficult task to accommodate the set up. Further thorough research needs to be carried out to solve these problems.

B.3 Conclusions

Various hydrogel synthesis steps were proposed so that the hydrogel could be synthesized and coated on top of the hollow fiber membrane bores. The hydrogel synthesis steps were changed from the reference (Jabbari et al, 2007). Instead of producing hydrogel right away, the hydrogel synthesis was carried out at a certain point so to turn low viscous solution to high viscous solution in order that the solution could coat on the hollow fiber membrane surface. The coated membrane would then be treated afterward to finish the hydrogel synthesis process. However, the experimental results showed that the high viscous solution could not be formed without a good amount of initiator particle aggregates remaining in the solution. This is a serious problem because the membrane bores could be blocked and the hydrogel layer was not homogeneous

because the solution was not homogeneous. The other major problem was that the synthesis must be under oxygen-free environment during the synthesis process. It would be a big challenge to design the equipment to accommodate this need. In conclusion, further research needs to be carried out to successfully synthesis hydrogel on top of the hollow fiber membrane surface.

APPENDIX C

MATHEMATICAL MODELING CODES

Appendix C shows R code for general use. To run a model, the user must specify the following variables.

1. Membrane area in cm^2 (A_membr). 17.34 and 51867.69 cm^2 for a flat plate membrane and hollow fiber membranes respectively.
2. Seed mass in g (Seed).
3. Cooling rate in $^oC/h$ (rate).
4. Starting and final temperature in ^oC (Start and Final).
5. Membrane thickness in cm (thickness). 0.006 and 0.035 cm for a flat plate membrane and hollow fiber membranes respectively.
6. Metastable limit concentrations corresponding to the cooling rate (metastable).

In this simulation, the model calculates the following values.

1. The concentrations of D and L-Glu in each vessel versus temperature.
2. The solubility and metastable limit concentrations versus temperature.
3. The increase of product mass along the course of the run.
4. The final product mass.

```
A_membr=51867.69 #cm2
KG = 0.0025 #cm/min
Seed = 14.25 #g
rate = 10 # C/hr
space = 1 #min
Start = 26 #C
Tfinal = 5 #C

thickness=35E-3 #cm
n = (Tstart-Tfinal)*60/rate
Diao = 600E-4 #cm
```

```
CriDia = 1E-7 #cm the critical diameter
rhos = 1.46 #g/cm3
num = Seed/rhos/(pi*Diao^3/6)
#constant
rho=1.012 #g/cm3
V1=565 #cm3
V2=565 #cm3
Adj = 1/0.4


#Initial value

#Apelblat, CD[i]=8.18E-8*exp(0.03815501*T[i])
To = 273.15 + Tstart #K
CDo= 0.008165   # g/g solution
CLo=CDo
Deo=5.936878E-7*To/(5.845-0.0163*To)
CSato=0.00295464*exp(0.0400456*(To-273.15))
metastableo=0

# Geometry
Rs2vo = 6/Diao
Rd2vo = 6/(pi*Diao^2)
Aco = pi*Diao^2


#Initial set
CD1 = c(rep(CDo,n))
CL1 = c(rep(CLo,n))
CD2 = c(rep(CDo,n))
CL2 = c(rep(CDo,n))
CSat = c(rep(CSato,n))
time = c(rep(0,n)) #hr
T = c(rep(To,n))
De=c(rep(Deo,n))
Def=c(rep(Deo,n))
Rs2vD=c(rep(Rs2vo,n))
Rs2vL=c(rep(Rs2vo,n))
Rd2vD=c(rep(Rd2vo,n))
Rd2vL=c(rep(Rd2vo,n))
AcD=c(rep(Aco,n))
AcL=c(rep(Aco,n))
DiaD = c(rep(Diao,n))
DiaL = c(rep(Diao,n))
JL = c(rep(0,n))
JD = c(rep(0,n))
JcD = c(rep(0,n))
JcL = c(rep(0,n))
MassD=c(rep(0,n))
MassL=c(rep(0,n))
TMassD=c(rep(Seed,n))
TMassL=c(rep(Seed,n))
metastable=c(rep(metastableo,n))
```

```
for(i in 2:n){
T[i]= T[i-1] -  rate/60
De[i]=5.936878E-7*T[i]/(5.845-0.0163*T[i])
Def[i]=0.5*(De[i]+De[i-1])

# metastable[i]=0.0031*exp(0.03970478*(T[i]-273.15))# 0.2C/hr
# metastable[i]=0.0044*exp(0.0387*(T[i]-273.15))# 0.5C/hr
# metastable[i]=0.0045*exp(0.0355*(T[i]-273.15))# 1 C/hr
# metastable[i]=0.004994*exp(0.038419*(T[i]-273.15)) # 5 C/hr
# metastable[i]=0.005403*exp(0.038602*(T[i]-273.15)) # 10 C/hr

# Solubility
CSat[i]=0.00295464*exp(0.0400456*(T[i]-273.15))


# Mass deposition & evolution
# Constant
# For D ############
X1 = space*Def[i]*rho/thickness*A_membr/V1/rho
Y1 = num*KG*rho*AcD[i-1]/V1/rho*space
X2 = Def[i]*rho/thickness*A_membr/V2/rho*space
A1 = 1/(1+X1+Y1)
A2 = 1/(1+X2)
B1 = (CD1[i-1]+Y1*CSat[i]+X1*A2*CD2[i-1])

# CD1[i]= CD1[i-1]+space*JD[i]*A_membr/V1/rho - num*JcD[i]*AcD[i-1]/V1/rho*space
CD1[i] = A1*B1/(1-X1*X2*A1*A2)

# CD2[i]= CD2[i-1]-JD[i]*A_membr/V2/rho*space
CD2[i] = A2*(CD2[i-1]+X2*CD1[i])

# For L ############
P1 = space*Def[i]*rho/thickness*A_membr/V2/rho
Q1 = num*KG*rho*AcL[i-1]/V2/rho*space
P2 = Def[i]*rho/thickness*A_membr/V1/rho*space
M1 = 1/(1+P1+Q1)
M2 = 1/(1+P2)
N1 = (CL2[i-1]+Q1*CSat[i]+P1*M2*CL1[i-1])

# CL2[i]= CL2[i-1]+space*Def[i]*rho*(CL1[i]-CL2[i])/thickness*A_membr/V2/rho -
num*KG*rho*(CL2[i]-CSat[i])*AcL[i-1]/V2/rho*space
CL2[i] = M1*N1/(1-P1*P2*M1*M2)

# CL1[i]= CL1[i-1]-Def[i]*rho*(CL1[i]-CL2[i])/thickness*A_membr/V1/rho*space
CL1[i] = M2*(CL1[i-1]+P2*CL2[i])

#Crystal surface
JcD[i] = KG*rho*(CD1[i]-CSat[i])
JcL[i] = KG*rho*(CL2[i]-CSat[i])

#Membrane
```

```
JD[i]=Def[i]*rho*(CD2[i]-CD1[i])/thickness
JL[i]=Def[i]*rho*(CL1[i]-CL2[i])/thickness

MassD[i] = JcD[i]*space*AcD[i-1]*num
MassL[i] = JcL[i]*space*AcL[i-1]*num

######
#Geometry change
TMassD[i] = TMassD[i-1]+MassD[i]
TMassL[i] = TMassL[i-1]+MassL[i]
DiaD[i] = (TMassD[i]*6/pi/rho/num)^(1/3)
DiaL[i] = (TMassL[i]*6/pi/rho/num)^(1/3)
AcD[i] = pi*DiaD[i]^2
AcL[i] = pi*DiaL[i]^2
#####
}

TMassD[n]-TMassD[1]


plot(T-273.15,CL2,'l',xlab='temperature (C)',ylab='composition (g/g solution)',main='Vessel 1',
ylim=c(0,0.012),xlim=c(5,26))
lines(T-273.15,CD2,lty='dashed')
lines(T-273.15,metastable, 'o')
lines(T-273.15,CSat,col='red')


ind=c(rep(1,31))
for(i in 2:31){
middle=n/30
ind[i]= round((i-1)*middle)
}

RsCD1=c(rep(CDo,31))
RsCL1=c(rep(CLo,31))
RsMet=c(rep(metastable[2],31))
RsCSat=c(rep(CSato,31))
Temp=c(rep(26,31))

for(i in 2:31){
RsCD1[i]=CD1[ind[i]]
RsCL1[i]=CL1[ind[i]]
RsMet[i]=metastable[ind[i]]
RsCSat[i]=CSat[ind[i]]
Temp[i]=T[ind[i]]-273.15
}

b <- data.frame(Temp, RsCD1, RsCL1, RsMet, RsCSat)
b
```

APPENDIX D

MATHEMATICAL CODE FOR ESTIMATING K_G*

In this appendix, the R code for estimating K_G* according to section 5.3 is presented. The estimation procedure could be found from section 5.3. In short, the value of K_G* was guessed and data were simulated. The calculated concentrations were compared with the experimental results here to search for the minimum of the roote mean square error (MSE) of these two results. This code generates the following values.

1. Roote mean square error (MSE) for each species in each vessel.
2. The percentage of MSE compared to the average experimental value.
3. The concentrations of each species in each vessel.
4. The plot of concentration versus temperature of the concentrations from the simulations and experiments.

```
# Having different volumes.

KG = 0.0025 #cm/min

Seed = 2.25 #g

rate = 1 # C/hr

space = 1 #min

Tstart = 40 #C

Tfinal = 37 #C

n = (Tstart-Tfinal)*60

Diao = 600E-4 #cm

rhos = 1.46 #g/cm3
```

```
num = Seed/rhos/(pi*Diao^3/6)

#Experiment values

# High seed mass

KAL1 = 0.0139

KAD1 = 0.0013

KAL2 = 0.0014

KAD2 = 0.0069

KBL1 = 0.0048

KBD1 = 0.0641

KBL2 = 0.0629

KBD2 = 0.0226

# Low seed mass

KAL1 = 0.0132

KAD1 = 0.0082

KAL2 = 0.0111

KAD2 = 0.0134

KBL1 = 0.006

KBD1 = 0.0178

KBL2 = 0.0106

KBD2 = 0.0061

#constant

A_membr=17.34945 #cm2

thickness=6E-3 #cm

rho=1.012 #g/cm3

V1=662.44 #cm3
```

```
V2=603.95 #cm3

Adj = 1/0.4


#Initial value

#Apelblat, CD[i]=8.18E-8*exp(0.03815501*T[i])

To = 273.15 + Tstart #K

CDo= 0.01679 # g/g solution

CLo=CDo

Deo=5.936878E-7*To/(5.845-0.0163*To)

CSato=8.18E-8*exp(0.03815501*To)

metastableo=0.0045*exp(0.0355*(To-273.15))

# Geometry

Rs2vo = 6/Diao

Rd2vo = 6/(pi*Diao^2)

Aco = pi*Diao^2


#Initial set

CD1 = c(rep(CDo,n))

CL1 = c(rep(CLo,n))

CD2 = c(rep(CDo,n))

CL2 = c(rep(CDo,n))

CSat = c(rep(CSato,n))

time = c(rep(0,n)) #hr

T = c(rep(To,n))

De=c(rep(Deo,n))
```

```
Def=c(rep(Deo,n))

Rs2vD=c(rep(Rs2vo,n))

Rs2vL=c(rep(Rs2vo,n))

Rd2vD=c(rep(Rd2vo,n))

Rd2vL=c(rep(Rd2vo,n))

AcD=c(rep(Aco,n))

AcL=c(rep(Aco,n))

DiaD = c(rep(Diao,n))

DiaL = c(rep(Diao,n))

JL = c(rep(0,n))

JD = c(rep(0,n))

JcD = c(rep(0,n))

JcL = c(rep(0,n))

MassD=c(rep(0,n))

MassL=c(rep(0,n))

TMassD=c(rep(Seed,n))

TMassL=c(rep(Seed,n))

metastable=c(rep(metastableo,n))




##########

# Estimate the error

ECD1 = c(rep(CDo,n))

ECL1 = c(rep(CDo,n))
```

```
ECD2 = c(rep(CDo,n))

ECL2 = c(rep(CDo,n))

difsquareD1=c(rep(1,n))

difsquareL1=c(rep(1,n))

difsquareD2=c(rep(1,n))

difsquareL2=c(rep(1,n))

for(i in 2:n){

T[i]= T[i-1] - rate/60

De[i]=5.936878E-7*T[i]/(5.845-0.0163*T[i])

Def[i]=0.5*(De[i]+De[i-1])

metastable[i]=0.0045*exp(0.0355*(T[i]-273.15))

CSat[i]=8.18E-8*exp(0.03815501*T[i])

# Mass deposition & evolution

# Constant

# For D ############

X1 = space*Def[i]*rho/thickness*A_membr/V1/rho

Y1 = num*KG*rho*AcD[i-1]/V1/rho*space

X2 = Def[i]*rho/thickness*A_membr/V2/rho*space

A1 = 1/(1+X1+Y1)

A2 = 1/(1+X2)

B1 = (CD1[i-1]+Y1*CSat[i]+X1*A2*CD2[i-1])

# CD1[i]= CD1[i-1]+space*JD[i]*A_membr/V1/rho - num*JcD[i]*AcD[i-1]/V1/rho*space

CD1[i] = A1*B1/(1-X1*X2*A1*A2)

# CD2[i]= CD2[i-1]-JD[i]*A_membr/V2/rho*space

CD2[i] = A2*(CD2[i-1]+X2*CD1[i])
```

```
# For L ############

P1 = space*Def[i]*rho/thickness*A_membr/V2/rho

Q1 = num*KG*rho*AcL[i-1]/V2/rho*space

P2 = Def[i]*rho/thickness*A_membr/V1/rho*space

M1 = 1/(1+P1+Q1)

M2 = 1/(1+P2)

N1 = (CL2[i-1]+Q1*CSat[i]+P1*M2*CL1[i-1])

# CL2[i]= CL2[i-1]+space*Def[i]*rho*(CL1[i]-CL2[i])/thickness*A_membr/V2/rho -
num*KG*rho*(CL2[i]-CSat[i])*AcL[i-1]/V2/rho*space

CL2[i] = M1*N1/(1-P1*P2*M1*M2)

# CL1[i]= CL1[i-1]-Def[i]*rho*(CL1[i]-CL2[i])/thickness*A_membr/V1/rho*space

CL1[i] = M2*(CL1[i-1]+P2*CL2[i])

#Crystal surface

JcD[i] = KG*rho*(CD1[i]-CSat[i])

JcL[i] = KG*rho*(CL2[i]-CSat[i])

#Membrane

JD[i]=Def[i]*rho*(CD2[i]-CD1[i])/thickness

JL[i]=Def[i]*rho*(CL1[i]-CL2[i])/thickness

MassD[i] = JcD[i]*space*AcD[i-1]*num

MassL[i] = JcL[i]*space*AcL[i-1]*num

######

#Geometry change

TMassD[i] = TMassD[i-1]+MassD[i]

TMassL[i] = TMassL[i-1]+MassL[i]

DiaD[i] = (TMassD[i]*6/pi/rho/num)^(1/3)
```

```
DiaL[i] = (TMassL[i]*6/pi/rho/num)^(1/3)

AcD[i] = pi*DiaD[i]^2

AcL[i] = pi*DiaL[i]^2

#####

ECD1[i] = KAD1*exp(KBD1*(T[i]-273.15))

ECL1[i] = KAL1*exp(KBL1*(T[i]-273.15))

ECD2[i] = KAD2*exp(KBD2*(T[i]-273.15))

ECL2[i] = KAL2*exp(KBL2*(T[i]-273.15))

}


for (i in 1:n){

difsquareD1 = (ECD1[i]-CD1[i])^2

difsquareL1 = (ECL1[i]-CL1[i])^2

difsquareD2 = (ECD2[i]-CD2[i])^2

difsquareL2 = (ECL2[i]-CL2[i])^2

}

MSPED1 = sqrt(sum(difsquareD1)/n)

MSPED2 = sqrt(sum(difsquareD2)/n)

MSPEL1 = sqrt(sum(difsquareL1)/n)

MSPEL2 = sqrt(sum(difsquareL2)/n)

PErrorL1 = MSPEL1/CDo*100

PErrorD1 = MSPED1/CDo*100

PErrorL2 = MSPEL2/CDo*100

PErrorD2 = MSPED2/CDo*100

MSPEL1
```

```
MSPED1

MSPEL2

MSPED2

MSPEL1+MSPED1+MSPEL2+MSPED2

PErrorL1

PErrorD1

PErrorL2

PErrorD2

PErrorL1+PErrorD1+PErrorL2+PErrorD2

ind=c(rep(1,31))

for(i in 2:31){

middle=n/30

ind[i]= round((i-1)*middle)

}

RsCD1=c(rep(CDo,31))

RsCL1=c(rep(CLo,31))

RsCD2=c(rep(CDo,31))

RsCL2=c(rep(CLo,31))

RECD1 = c(rep(CDo,31))

RECL1 = c(rep(CDo,31))

RECD2 = c(rep(CDo,31))

RECL2 = c(rep(CDo,31))

RsMet=c(rep(metastable[2],31))

RsCSat=c(rep(CSato,31))

Temp=c(rep(40,31))
```

```
for(i in 2:31){

RsCD1[i]=CD1[ind[i]]

RsCL1[i]=CL1[ind[i]]

RsCD2[i]=CD2[ind[i]]

RsCL2[i]=CL2[ind[i]]

RECD1[i]=ECD1[ind[i]]

RECL1[i]=ECL1[ind[i]]

RECD2[i]=ECD2[ind[i]]

RECL2[i]=ECL2[ind[i]]

RsMet[i]=metastable[ind[i]]

RsCSat[i]=CSat[ind[i]]

Temp[i]=T[ind[i]]-273.15

}

b <- data.frame(Temp, RECD1, RECL1, RECD2, RECL2,RsMet, RsCSat)

b
```

REFERENCES

B. Adnadjevic, J. Jovanovic, B. Drakulic, Isothermal kinetics of (E)-4-(4-metoxyphenyl)-4-oxo-2-butenoic acid release from poly(acrylic acid), Thermochimica Acta, hydrogel, 466 (2007) 38-48.

A. Apelblat, E. Manzurola, Solubility of L-aspartic, DL-aspartic, DL-Glutamic, p-hydroxybenzoic, o-anistic, p-anisic, and itaconic acids in water from T = 278 K to T = 345 K, Journal of Chemical Thermodynamics 29 (1997) 1527.

D.H. Beiny, J.W. Mullin, Solubilities of higher normal alkanes in m-xylene, Journal of Chemical Engineering and Data 32 (1987) 9.

E. Barbier, M. Coste, A. Genin, D. Jung, C. Lemoine, S. Logette, H. Muhr, Simultaneous determination of nucleation and crystal growth kinetics of gypsum, Chemical Engineering Science 64 (2009) 363.

P. Bennema, Surface diffusion and the growth of sucrose crystals, Journal of Crystal Growth 3-4 (1968) 331.

M. Bryajak, J. Kozlowski, P. Wiezorek, P. Kafarski, Enantioselective transport of amino-acid though supported chiral liquid membrane, Journal of Membrane Science 85 (1993) 221.

T. Bushse, D.K. Kondepudi, and B. Hoskins, Kinetics of chial resolution in stirred crystallization of D/L-Glu, Chirality 11 (1999) 343.

A.A. Ceyhan, O. Sahin, A.N. Bulutcu, Crystallization kinetics of the borax dehydrate, Journal of Crystal Growth 300 (207) 440.

G.S. Chauhan, A. Kumar, A study in the uranyl ions uptake on acrylic acid and acrylamide copolymeric hydrogels, Journal of Applied Polymer Science 110 (2008) 3795.

A.N. Collins, G.N. Sheldrake, and J. Crosby (editors), Chirality in industry: the commercial manufacture and applications of optically active compounds, John Wiley & Sons, Chichester, 1992, page 20

J.B. Dalton, C.L.A. Schmidt, The solubilities of certain amino acids in water, the densities of their solutions at twenty-five degrees, and the calculated heats of solution and partial molal volume, Journal of Biological Chemistry 103 (1933) 549.

M.A. Deji, J.H. ter Horst, H. Meekes, P. Jansens, and E. Vlieg, Polymorph formation studied by 3D nucleation simulations. Application to a yellow isoxazolone dye, paracetamol, and L-Glutamic acid, Journal of Physical Chemistry B. 111 (207) 1523.

P. Dzygiel, P. Wieczorek, J.A. Jonsson, M. Milewska, P. Kasfarski, Separation of amino acid enantiomers using supported liquid membrane extraction with chiral phosphates and phosphonates, Tetrahedron 55 (1999) 9923.

M.P. Elsner, G. Ziomek, A. Seidel-Morgenstern, Simultaneous preferential crystallization in a coupled, batch operation mode – Part I: Theoretical analysis and optimization, Chemical of Engineering Science 62 (2007) 4760.

G.D. Fasman, Handbook of Biochemistry & Molecular Biology, Physical & Chemical Data, 3rd ed., CRC Press, Cleaveland, OH, volume 1 1976 page 115

J. Garside, The concept of effectiveness factors in crystal growth, Chemical Engineering Science 26 (1971) 1425.

G.H. Gilmer, R. Ghez, N. Carera, An analysis of combined and volume diffusion process in crystal growth, Journal of Crystal Growth 8 (1971) 79.

T. Gumi, C. Minguillon, C. Palet, Separation of propranolol enantiomers though membranes based on chiral derivatized polysulfone, Polymer 46 (2005a) 12306.

T. Gumi, M. Valiente, C. Palet ,Elucidation of SR-propranolol transport rate and enantioselectivity though chial activated membranes, Journal of Membrane Science 256 (2005b) 150.

P. Hadik, L. Kotsis, M. Eniszne-Bodogh, L.-P. Szabo, and E. Nagy, Lactic acid enantioseparation by means of porous ceramic disc and hollow fiber organic membrane, Separation and Purification Technology 41 (2005) 299.

P. Hadik, L.P. Szabo, E. Nagy, D,L-Lactic acid and D,L-alanine enantioseparation by memebrane process, Desalination 148 (2002) 193.

P. Harriott, Mass transfer to particles: Part I. Suspended in agitated tanks, AIChE Journal 8 (1962) 93.

A. Higuchi, Y. Higuchi, K. Furuta, B.O. Yoon, M. Hara, S. Maniwa, M. Saitoh, K. Sanui, Chiral separation of phenylalanine by ultrafiltration though immobilized DNA membrane, Journal of Membrane Science 221 (2003) 207.

A. Higuchi, Y. Yomogita, B.O. Yoon, T. Kojima, M. Hara, S. Maniwa, M. Saitoh, Optical resolution of amino acid by ultrafiltration using recognition sites of DNA, Journal of Membrane Science 205 (2002) 203.

T.A. Howell Jr., E.B. Yoseph, C. Rao, R.W. Hartel, Sucrose crystallization kinetics in thin fils at elevated temperature and supersaturations, Crystal Growth Design 2 (2002) 67.

E. Jabbari, J. Tavokoli, A.S. Sarvestani, TaSwelling characteristics of acrylic acid polyelectrolyte hydrogel in a dc electric field, *Smart Materials and Structures* 16 (2007) 1614.

J. Jacques, A. Collet, SH. Wilen, Enantiomers, Racemates and Resolutions, 1994 John Wiley & Sons, New York.

Z.J. Jin, K-C Chao, Solubility of four amino acids in water and of four pairs of amino acids in their water solution, Journal of Chemical Engineering Data 37 (1992) 199.

P. Jit, W. Feng, Solubility of amino acids in water and aqueous solutions by the statistical associating fluid theory, Industrial and Engineering Chemistry Research 47 (2008) 6275.

P.H. Karpinski, Importance of the two-step crystal growth model, Chemical Engineering Science 40 (1985) 641.

J.T.F. Keruentjes, L.J.W.M. Nabuurs, E.A. Vegter, Liquid membrane technology for separation of racemic mixture, Jouranl of Membrane Science 113 (1996) 351.

K.V. Kumar, Regression analysis for the two-step growth kinetics of crystals in pure solutions, Industrial & Engineering Chemistry Research 48 (2009a) 7852.

K.V. Kumar, Simple kinetic expressions to study the transport process during the growth of crystals in solution, Industrial & Engineering Chemistry Research 48 (2009b) 11236.

K.V. Kumar, A semienpirical kinetics for modeling and simulation of the crystal growth process in pure solutions, Industrial & Engineering Chemistry Research 48 (2009c) 5105.

K.V. Kumar, P. Martins, F. Rocha, Modelling of the batch sucrose crystallization kinetics using artificial neural networks: Comparison with conventional regression analysis, Industrial & Engineering Chemistry Research 47 (2008) 4917.

A.V. Kustov, V.P. Korolev, The thermodynamic characteristics of solution of L-α-histidine and L-α-phenylalanine in water at 273-373 K, Russian Journal of Physical Chemistry 82 (2008) 1828.

P.A. Levkin, Y.A. Strelenko, K.A. Lyssenko, V. Schurig, R.G. Kostyanovsky, Temperature-dependent racemic compound-conglomerate crystallization of 2,3:6,7-dibenzobicyclo[3.3.1]nona-2,6-diene-4,8-dione, Tetrahedron: Asymetry 14 (2003) 2059.

W.L. McCabe, J.C. Smith, P. Harriott, Unit Operations of Chemical Engineering, 5th ed., 1993 McGraw-Hill, New York, p 672.

J.W. Mullin, Crystallization, 4th ed. 2001 Elservier, Amsterdam

J.W. Mullin, C. Gaska, The growth and dissolution of potassium sulphate crystals in a fluidized bed crystallizer, Canadian Journal of Chemical Engineering 47 (1969) 483.

J.W. Mullin, C. Gaska, Potassium sulfate crystal growth rates in aqueous solution, Journal of Chemical Engineering Data 18 (1973) 217.

Z.J. Li, W.H. Ojala, D.J.W. Grant, Molecular modeling study of chiral drug crystals: lattice energy calculations, Journal of Pharmaceutical Sciences 90 (2001) 1523.

Z.J. Li, M.T. Zell, E.J. Munson, and D.J.W. Grant, Characterization of racemic speicies of chial drugs using thermal analysis, thermodynamic calculation, and structural studies, Journal of Pharmaceutical Sciences 88 (1999) 337.

H. Lorenz, D. Sapoundjiev, A. Seidel-Morgenstern, Enantiomeric mandelic acid system-melting point phase diagram and solubility in water, Journal of Chemical Engineering Data 47 (2002) 1280.

G.D.C. Machado, M. Gomes Jr., O.A.C. Antures, E.G. Oestreicher, Enzymic resolution of DL-phenylglycine, Process Biochemistry 40 (2005) 3186.

E. Manzurola, A. Apelblat, Solubilities of L-Glu, 3-nitrobenzoic acid, p-toluic acid, calcium-L-lactate, calcium gluconate, magnesium-DL-aspartate, and magnesium-L-lactate in water, Journal of Chemical Thermodynamics 34 (2002) 1127.

M. Matsuoka, Secondary growth phenomena in industrial crystallization and their effects on crystal quality, Journal of Chemical Engineering of Japan 35 (2002) 1025.

W.L. McCabe, J.C. Smith, P. Harriott, Unit Operations of Chemical Engineers, McGraw-Hill, 5th ed., New York, 1993 page 672-673.

J.W. Mullin, Crystallization, Crystallization, Elsevier, 4th ed., Amsterdam, 2001

J.W. Mullin, C. Gaska, The growth and dissolution of potassium sulphate crystals in a fluidized bed crystallizer, Canadian Journal of Chemical Engineers 47 (1996) 483.

J.W. Mullin, C. Gaska, Potassium sulfate crystal growth rates in aqeous solution, Journal of Chemical Engineering Data 18 (1973) 217.

P.E.M. Overdevest, M.H.J. Hoenders, K. van't Riet, A. ven der Padt, Enantiomer separation in a cascaded micellar-enhanced ultrafiltration system, AIChE Journal 48 (2002) 1917.

G.R. Pazuki, M. Nikookar, A new local composition model for predicting of activity coefficient and solubility of amino acids and peptides in water, Biochemical Engineering Journal 28 (2006) 44.

V.M. Profir and A.C. Rasmuson, Influence of solvent and the operating conditions on the crystallization of racemic mandelic acid, Crystal Growth & Design 4 (2004) 315.

M. Pulat and H. Eksi, Determination of swelling behavior and morphological properties of poly(acrylamide-co-itaconic acid) and poly(acrylic acid-co-itaconic acid) copolymeric hydrogels, Journal of Applied Polymer Science 102 (2006) 5994.

M. Pulat and D. Esil, Fluconazole Release Through Semi-Interpenetrating, Journal of Applied Polymer Science 113 (2009) 2613.

G. Sgualdino, D. Aquilano, A. Cincottia, L. Pastero, G. Vaccari, Faceb-by-face growth of sucrose crystals from aqeous solutions in the presence of raffinose. I. Experiments and kinetic-adsorption model, Journal of Crystal Growth 292 (2006) 92.

O. Sahin, Effect of electrical field and temperature on the crystal growth rates of boric acid, Crystal Research and Technology 37 (2002) 183.

O. Sahin, M. Ozdemir, H. Kendirci, A.N. Bulutcu, Determination of growth and dissolution of boric acid crystals by a simple computer program, Journal of Crystal Growth 219 (2000) 75.

O. Sahin, N. Genli, M. Ozdemir, The role of transport processes in crystallization kinetics of ammonium pentaborate, Journal of Crystal Growth 253 (2003) 488.

L.-D. Shiau, The distribution of dislocation activities among crystals in sucrose crystallization, Chemical Engineering Science 58 (2003) 5299.

E.A. Sobczak, A simple method of determination of mass transfer coefficients and surface reaction constants for crystal growth, Chemical Engineering Science 45 (1990) 561.

R.F. Strickland-Constable, *Kinetics and Mechanism of Crystallization*, Academic Press, London (1968).

X.J. Wang, H. Wiehler, and C.B. Ching, Study of the characterization and crystallization of 4-hydroxy-2-pyrrolidone, Chirality 16 (2004) 220.

X.J. Wang, H. Wiehler, and C.B. Ching, Physicochemical properties and the crystallization thermodynamics of the pure enantiomer and the racemate for n-methylephedrine, Journal of Chemical Engineering Data 48 (2003) 1092.

X. Wang, X.J. Wang, and C.B. Ching, Solubility, metastable zone width, and racemic characterization of propanolol hydrochloride, Chirality 14 (2002) 318.

Y. Wang, R. LoBrutto, R.W. Wenslow, and I. Santos, Eutectic composition of a chiral mixture containing a racemic compound, Organic Process Research & Development 9 (2005) 670.

J.R. Welty, C.E. Wicks, R.E. Wilson, G.L. Rorrer, Fundamentals of Momentum, Heat, and Mass Transfer, 4th ed., 2000 John Wiley & Sons, New York, p. 151.

C.R. Wilke, P. Chang, Correlation of diffusion coefficients in dilute solutions, Chemical Engineering Progress 1 (1955) 264.

S.H. Yalkowsky, Y. He, Handbook of aqueous solubility data, 2003, CRC Press, Boca Raton.

M. Yokota, N. Doki, and K. Shimizu, Chiral separation of a racemic compound induced by transformation of racemic crystal structures: DL-Glu, Crystal Growth & Design 6 (2006) 1588.